



National Library
of Canada

Bibliothèque nationale
du Canada

Acquisitions and
Bibliographic Services Branch

Direction des acquisitions et
des services bibliographiques

395 Wellington Street
Ottawa, Ontario
K1A 0N4

395, rue Wellington
Ottawa (Ontario)
K1A 0N4

Your file - Votre référence

Our file - Notre référence

NOTICE

AVIS

The quality of this microform is heavily dependent upon the quality of the original thesis submitted for microfilming. Every effort has been made to ensure the highest quality of reproduction possible.

La qualité de cette microforme dépend grandement de la qualité de la thèse soumise au microfilmage. Nous avons tout fait pour assurer une qualité supérieure de reproduction.

If pages are missing, contact the university which granted the degree.

S'il manque des pages, veuillez communiquer avec l'université qui a conféré le grade.

Some pages may have indistinct print especially if the original pages were typed with a poor typewriter ribbon or if the university sent us an inferior photocopy.

La qualité d'impression de certaines pages peut laisser à désirer, surtout si les pages originales ont été dactylographiées à l'aide d'un ruban usé ou si l'université nous a fait parvenir une photocopie de qualité inférieure.

Reproduction in full or in part of this microform is governed by the Canadian Copyright Act, R.S.C. 1970, c. C-30, and subsequent amendments.

La reproduction, même partielle, de cette microforme est soumise à la Loi canadienne sur le droit d'auteur, SRC 1970, c. C-30, et ses amendements subséquents.

Canada

Active Alignment for a Free-Space Optical Backplane

Guillaume C. Boisset

**Department of Electrical Engineering
McGill University
Montreal, Canada
September, 1994**

**A thesis submitted to the Faculty of Graduate Studies and Research in
partial fulfillment of the requirements of the degree of Master of
Engineering**

(c) Guillaume Boisset, 1994.



National Library
of Canada

Acquisitions and
Bibliographic Services Branch

395 Wellington Street
Ottawa, Ontario
K1A 0N4

Bibliothèque nationale
du Canada

Direction des acquisitions et
des services bibliographiques

395, rue Wellington
Ottawa (Ontario)
K1A 0N4

Your file / Votre référence

Our file / Notre référence

THE AUTHOR HAS GRANTED AN IRREVOCABLE NON-EXCLUSIVE LICENCE ALLOWING THE NATIONAL LIBRARY OF CANADA TO REPRODUCE, LOAN, DISTRIBUTE OR SELL COPIES OF HIS/HER THESIS BY ANY MEANS AND IN ANY FORM OR FORMAT, MAKING THIS THESIS AVAILABLE TO INTERESTED PERSONS.

L'AUTEUR A ACCORDE UNE LICENCE IRREVOCABLE ET NON EXCLUSIVE PERMETTANT A LA BIBLIOTHEQUE NATIONALE DU CANADA DE REPRODUIRE, PRETER, DISTRIBUER OU VENDRE DES COPIES DE SA THESE DE QUELQUE MANIERE ET SOUS QUELQUE FORME QUE CE SOIT POUR METTRE DES EXEMPLAIRES DE CETTE THESE A LA DISPOSITION DES PERSONNE INTERESSEES.

THE AUTHOR RETAINS OWNERSHIP OF THE COPYRIGHT IN HIS/HER THESIS. NEITHER THE THESIS NOR SUBSTANTIAL EXTRACTS FROM IT MAY BE PRINTED OR OTHERWISE REPRODUCED WITHOUT HIS/HER PERMISSION.

L'AUTEUR CONSERVE LA PROPRIETE DU DROIT D'AUTEUR QUI PROTEGE SA THESE. NI LA THESE NI DES EXTRAITS SUBSTANTIELS DE CELLE-CI NE DOIVENT ETRE IMPRIMES OU AUTREMENT REPRODUITS SANS SON AUTORISATION.

ISBN 0-315-99955-1

Canada

ABSTRACT

Future high-performance digital computing systems will demand extremely high throughput backplanes to meet massive connectivity requirements between computing subsystems. This thesis begins by analyzing the characteristics of high-performance electronic backplanes and argues that electronic backplanes face fundamental cost/performance limitations which free-space optical backplanes can overcome provided key problems such as maintaining mechanical alignment in an industrial setting are resolved. An analysis of misalignment mechanisms indicates that active alignment is a powerful solution to the problem of optical alignment. A review of active alignment in other optical systems such as compact disk players and telescopes is then conducted.

The central part of this thesis presents the theoretical design, simulation, fabrication and testing of a novel active alignment demonstrator system based on Risley Beam Steerers. The demonstrator features a quadrant detector which detects the misalignment error between the centre of a spot of light and the centre of the quadrant detector. This misalignment error is then used by a new algorithm to calculate the rotational displacement required for the two Risley Beam Steerers to steer the spot of light to the centre of the quadrant detector. This experimental system contains all the necessary optics, optomechanics, electronics, and computer hardware and software required to demonstrate the task of centering the spot. The experimental results indicate that any spot misaligned by up to 160 μm on the quadrant detector will be systematically centered by the demonstrator system. Future directions for active alignment are then presented and discussed.

RÉSUMÉ

Les ordinateurs numériques à haute performance du futur nécessiteront des fonds de panier ("backplanes") à débit extrêmement élevé afin de répondre aux immenses besoins des connexions entre sous-systèmes informatiques. Cette thèse commence par analyser les traits principaux des backplanes électroniques à haute performance et indique qu'ils font face à des limitations de coût/performance fondamentales que les backplanes à optique libre pourront surmonter à condition que certains problèmes clés, tels que le maintien de l'alignement en milieu industriel, soient résolus. Les causes principales des défauts d'alignement mécanique sont étudiées et quantifiées et l'utilisation de l'alignement actif est présentée comme un outil puissant pour résoudre le problème du maintien de l'alignement optique. Cette étude est suivie d'une revue de l'alignement actif dans d'autres systèmes comme les disques compacts et les télescopes.

La partie principale de cette thèse présente la conception théorique, la simulation, la fabrication et les essais d'un nouveau démonstrateur d'alignement actif utilisant des prismes Risley. Dans ce démonstrateur, un détecteur à quadrants détecte les défauts d'alignement entre le centre d'un point lumineux et le centre du détecteur à quadrants. Le démonstrateur met en application un nouvel algorithme de centrage qui calcule le déplacement rotationnel nécessaire à deux prismes Risley pour centrer un point lumineux sur un détecteur à quadrants. De surcroît, le démonstrateur inclut toutes les composantes optiques, optomécaniques, électroniques, et informatiques (équipements et logiciels) afin de mener à bien la tâche de centrer le point lumineux. Les résultats expérimentaux indiquent que tout point lumineux jusqu'à 160 microns du centre peut être effectivement centré par le démonstrateur. Enfin, de nouvelles avenues de recherche dans le domaine de l'alignement actif sont proposées et discutées.

Acknowledgements

I wish to thank my supervisor, Professor Scott Hinton, for his superb guidance, support, and constant encouragement to always reach higher. I am deeply indebted to him for teaching me so much about research, from the theoretical to the practical and beyond.

Many thanks to Professor Dave Plant for his enthusiastic help and key advice in so many theoretical, experimental, and administrative matters. Un super merci à Brian Robertson for teaching me basic principles of optics, for always patiently answering all my barrages of questions, for his constant assistance, and for reviewing my thesis.

Thanks to all the great guys in the group, Marcos, Nam, Yongsheng, Alain, Lizhong, Dave, Dave, Will and Bill Robertson at NRC for their vital help, suggestions, and encouragement day and night. A special thanks to Bielo, André and especially Don Pavlasek for helping me in my mechanical designs and for spending countless hours explaining to me what can and what cannot be done in a machine shop. Thanks also to Messrs Marx and Hughes from BNR who kindly took the time to show me how a real backplane is fabricated.

Merci Séverine.

And most importantly, thank you to my parents and family for their love and support during all my studies.

The work on active alignment was supported by the McGill BNR/NT-NSERC Industrial Chair in Photonic Systems.

Table of Contents

Chapter 1: Introduction and motivation.....	1
1.1 Introduction	1
1.2 Definition of a backplane	2
1.3 Survey of modern electronic backplanes.....	2
1.4 Cost/performance limitations of electronic backplanes.....	5
1.4.1 Transmission line effects.....	5
1.4.2 Energy and power requirements.....	9
1.4.3 Limitations of separable electronic interconnects.....	10
1.5 Optical backplane demonstrators.....	12
1.6 Organization of the thesis.....	15
1.7 References.....	15
Chapter 2: Alignment constraints within a free-space optical backplane.....	19
2.1 Introduction	19
2.2 Basic misalignment mechanisms.....	19
2.2.1 Misalignment in the x-y plane	22
2.2.2 Misalignment in the z-direction.....	23
2.2.3 Tilt about the x and y axes	24
2.2.4 Rotation about the z-axis	26
2.2.5 Further comments on misalignment mechanisms	28
2.3 Effect of the harsh conditions in a backplane environment on optomechanics.....	29
2.3.1 Thermal effects: mechanical stress on optics.....	30
2.3.2 Thermal Effects: movement of optics.....	32
2.3.3 Vibration and shock.....	34
2.4 Consequences of board insertion on mechanical specifications in backplane chassis	35
2.5 Possible solutions to mechanical misalignment.....	35
2.6 Conclusion	36
2.7 References.....	37
Chapter 3: Review of active alignment.....	39
3.1 Introduction	39
3.2 Definition of active alignment.....	39
3.3 X-Y-Z active alignment: compact disk and optical disk players.....	40
3.4 Angular correction: Hubble Space Telescope	41

3.5 Image jitter compensation: ground-based astronomical telescopes	44
3.6 Issues in active alignment.....	47
3.6.1 Reliability	47
3.6.2 Accuracy	48
3.6.3 Cost.....	49
3.7 Conclusion	49
3.8 References.....	50
Chapter 4: Theory of x-y active alignment using Risley Beam Steerers	52
4.1 Introduction	52
4.2 Determination of misalignment error	53
4.2.1 Geometric and opto-electronic features of a quadrant detector.....	53
4.2.2 Definitions and assumptions.....	55
4.2.3 Total light power for centered spot.....	55
4.2.4 Total light power for misaligned spot.....	56
4.2.5 Application of equations describing total light power.....	57
4.3 Model of Movement of Risley Beam Steerers.....	59
4.3.1 Justification for using Risley Beam Steerers in active alignment	59
4.3.2 Definitions and assumptions.....	59
4.3.3 Effect of two RBSs in series on the trajectory of a beam.....	60
4.3.4 Transformation expressing lateral Cartesian displacement as an angular RBS displacement (CtoR transform).....	61
4.3.5 Cartesian displacement of spot imparted by two RBSs with known angular rotation (RtoC Transform)	64
4.3.6 Formal algorithm for calculating the angular displacement necessary for two RBSs to correct a lateral misalignment error detected by a quadrant detector.....	64
4.3.7 Formal algorithm for determining initial (q_A , q_B) given arbitrary initial angular displacement of RBSs	65
4.3.8 Resolution of RBS angular movement required for 1 mm alignment accuracy	66
4.3.9 Simulation of movement due to rotating RBSs.....	67
4.4 Conclusion	70
4.5 References.....	70
Chapter 5: Design and construction of active alignment demonstrator	71
5.1 Introduction	71

5.2 Optoelectronics and electronics for detection and transmission of error signal	72
5.2.1 Choice of resistor value	72
5.2.2 Choice of reverse bias voltage for photodetectors on quadrant detector.....	74
5.2.3 Uniformity of optoelectronic sensitivity on quadrant detector	75
5.2.4 Experimental analysis of the analog signal transmission setup	78
5.3 Determination of optical parameters	80
5.3.1 Choice of lens focal length.....	80
5.3.2 Theoretical and experimental determination of optimal spot size and measurement sensitivity constant.....	81
5.4 Optomechanical design and actuator issues.....	83
5.4.1 Power train from actuator to RBS holder	83
5.4.2 Fabrication of RBS holder assembly	84
5.5 Design, fabrication, and analysis of the optomechanical support structure for the Quadrant Detector package	88
5.6 Computer hardware and software setup	91
5.7 Effect of packaging and optomechanics on spot profile.....	92
5.8 Conclusion	93
5.9 References.....	93
Chapter 6: Experimental results.....	94
6.1 Introduction	94
6.2 Centering the spot	94
6.2.1 Implementation of algorithm.....	94
6.3 Limitations of demonstrator	98
6.3.1 Wedge mismatch	98
6.3.2 Limitations on initial conditions for the hunting algorithm.....	99
6.4 Conclusion	100
6.5 Reference	100
Chapter 7: Future directions and conclusion	101
7.1 Future Directions	101
7.1.1 Scalability.....	101
7.1.2 Integration of alignment intelligence	103
7.1.3 Further issues.....	104
7.2 Conclusion	105
Appendix A: Exact calculation of effect on beam of RBSs in series	106

Chapter 1

Introduction and motivation

1.1 Introduction

As society continues to pour ever more data into high performance computers and telecommunication systems, conventional electronic interconnects between digital computing subsystems soon will be overwhelmed. A key interconnect is at the backplane level, where data throughput demands are rapidly increasing to a point where electronic backplanes no longer will be able to meet these demands in a cost-effective manner.

Free-space optical interconnects hold the promise of alleviating these communication bottlenecks which will arise in the connection-intensive backplanes of future high-performance digital systems^(1,2). A separable interconnect offering the massive connectivity of free-space optics will greatly increase the data throughput between printed circuit boards on an optical backplane.

This thesis explores the use of free-space optics to implement extremely high performance backplanes and focuses on the key issue of alignment: for an optical backplane to be of practical use, it must be capable of operating continuously over long periods of time, unaffected by mechanical and optical misalignments, external vibrations and temperature changes. Active alignment is shown to provide a powerful technique for maintaining alignment in free-space optical backplanes.

The results of an experiment into the design and fabrication of an active alignment system for a free-space optical backplane are presented. The demonstrated system contains algorithms that determine the misalignment of an optical interconnect and calculate the rotational displacement required for two Risley Beam Steerers (RBSs) to properly re-align the interconnect. An active alignment solution implementing RBSs is shown to be advantageous since RBSs are less susceptible to drift and have already proven their worth in free-space optical systems implementing manual alignment.

In section 1.2 of this chapter the definition of a backplane is given. In section 1.3 an overview of existing electronic backplane standards is presented. Sections 1.4 and 1.5 demonstrate that electronic backplanes are approaching fundamental limitations which will restrict any further cost-effective improvements in their performance and that free-space optical backplanes can overcome these basic limitations if physical and engineering problems such as alignment are solved. In section 1.6, an outline of the thesis is presented.

1.2 Definition of a backplane

A backplane can be defined as a high performance structure that provides the physical, mechanical and electrical support for high-speed digital communication between removable printed circuit boards (PCBs) within a frame (chassis). A simplified view of a PCB and a backplane, along with a typical scale, is shown in Figure 1.1.

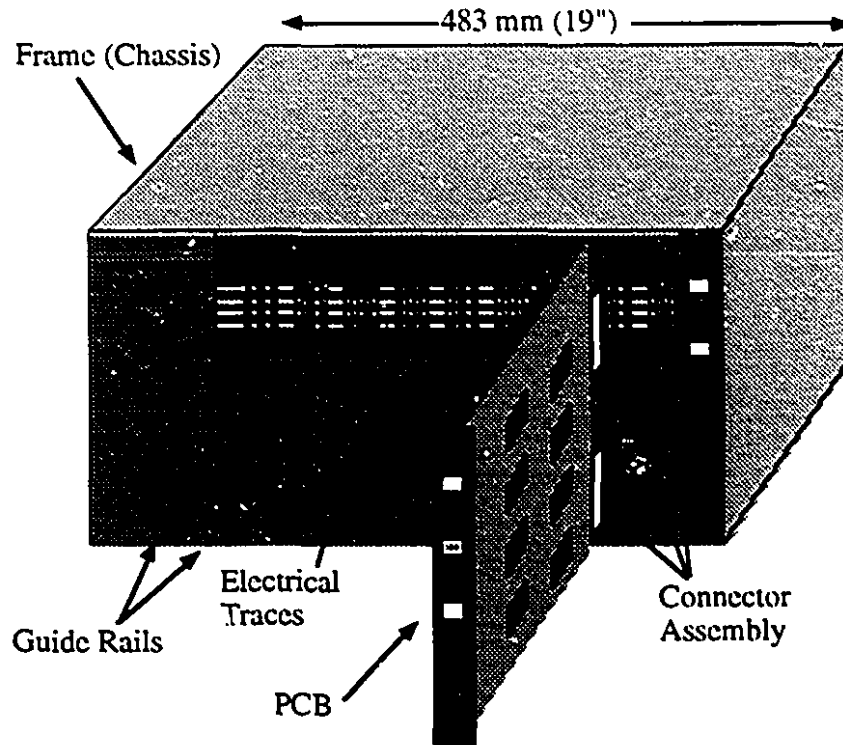


Figure 1.1: PCB being inserted into a backplane in a computing system chassis.

1.3 Survey of modern electronic backplanes

Before launching into an analysis of electronic and photonic backplanes, it is essential to determine what are the characteristics of existing backplanes in computers today; this reality check will ensure the relevance of subsequent analyses and comparisons. The following is a study of open, standardized backplanes. While other unpublished proprietary standards do exist (i.e. the backplanes in the BNR SupernodeTM or in the AT&T SESSTTM switch), the standards described below are nonetheless representative of high performance backplane systems commercially available today.

Tables 1.1 and 1.2 indicate key characteristics of existing backplanes and the meaning of each column is as follows. The IEEE standard # is important for a backplane definition

since it indicates that the backplane standard has been studied and approved by leading members of the technical and scientific community. The data bus width, address space, peak throughput and clock frequency (in a synchronous backplane, the clock frequency is fixed for all transactions on the backplane; in an asynchronous backplane, the clock rate is determined by the master in any transaction) are traditional logical characteristics which are always scrutinized by backplane end-users since they are an important factor in determining the performance of the computing system using the backplane. In Table 1.2, the expression "Pins: SigGnd/Total" indicates the ratio of the total number of ground pins to the total number of pins; this expression and the term "insertion force per pin" will be explained in subsection 1.4.3 (for ergonomic reasons, industry standards usually specify that the force required to insert a PCB into a backplane be under 200N). The pin pitch and PCB pitch respectively represent the centre-to-centre distance between individual pins on the PCB-backplane connector and the centre-to-centre distance between PCBs along the backplane. The driver column applies only to the backplane transceivers.

Name	IEEE standard	Data bus width max	Address space max 2 ^x	Peak rate (MByte/sec)	Synchronous / f clk (MHz)
<i>Early systems</i>					
CAMAC ⁽³⁾	583	24	24	3	Y/1
<i>PC First Generation</i>					
E/ISA ^(4,5)	P996	32	24	33	Y/8
MCA ^(6,7)	IBM	32	32	20	Y/5
NuBus ⁽⁶⁾	1196	32	32	37.5	Y/10
<i>PC Second Generation</i>					
VL ⁽⁸⁾	-	32	32	85-160	Y/40
PCI ⁽⁹⁾	-	64	32	85-132	Y/20
<i>Specialized Systems: Avionics, DSP, Scientific</i>					
PI-BUS ^(10,11)	(SAE) 4710	32	32	100	Y/100
DTConnect II ⁽¹²⁾	Proprietary	32	32	100	Y/25
Fastbus ^(13,14)	960	32	32	160	N
<i>Systems in Widespread Use Today</i>					
STD80 ⁽⁶⁾	961	16	24	4	Y/8
STD32 ⁽¹⁵⁾	961	32	32	32	Y/8
VMEfamily ^(16,17)	1014	32	32	40-80	N
MultibusI ⁽⁶⁾	796	16	14+4	10	N
MultibusII ⁽⁶⁾	1296	32	32	40	Y/10
<i>Newer Designs</i>					
Futurebus+ ⁽¹⁸⁾	896.x	256	64	Meas: 600	N
SCI ⁽¹⁹⁾	P1596	N/A	N/A	65x10 ⁶	N/A

Table 1.1: Selected Backplanes: General Characteristics.

Many performance parameters such as peak rate numbers are often controversial, since different interpretations and scenarios (i.e. infinite length packets) lead to different values. The peak rate numbers given are reasonable estimates based on existing technology and claims, although peak rate values often change over the years as incremental improvements are brought to the technology and protocols ⁽²⁰⁾.

PI-BUS is a (mainly military) avionics standard which has only an electrical and logical specification, and as such is not a pure backplane according to the definition given above. Nonetheless, it is included in this study in order to give an indication of the performance of military avionics systems. Futurebus+ is divided into many sub-specifications called profiles which specialize in different applications: the table describes a typical profile (profile F). Scalable Coherent Interface (SCI) is not a traditional backplane in that it does not offer a definite physical structure: it is more an expanded switching network. Nonetheless, SCI can support communications between PCBs and does contain an electrical definition to that end, so it is often classified as a backplane.

Name	Max PCBs allowed	Pins: SigGnd/ Total	max insert force/pin NEWTONS	pin pitch inch (mm)	PCB pitch inch (mm)	Driver
<i>Early Systems</i>						
CAMAC	25	3/86	80 (total)	0.1 (2.54)	0.67(17.2)	TTL
<i>PC First Generation</i>						
E/ISA	16	AT:14/98	1.2	0.1(2.54)	0.8(2.03)	TTL
MCA ⁽⁷⁾	16	27/89	1.2	0.05(1.27)	0.8(2.03)	TTL
NuBus	16	27/192	0.96	0.1(2.54)	0.8(2.03)	TTL
<i>PC Second Generation</i>						
VL	3	28/196 (est)	1.2	0.05 (1.27)	0.8(2.03)	TTL
PCI	5	38/188	1.2	0.05(1.27)	0.85(2.16)	TTL
<i>Specialized Systems: Avionics, DSP, Scientific</i>						
PI-BUS	32	N/A	N/A	N/A	N/A	TTL
DT Connect II	5	50/100	in:1.11 out:0.13	0.05(1.27)	1" (25.4)	TTL
Fastbus	26	36/130	1.2	0.1(2.54)	0.6(1.52)	ECL10K
<i>Systems in Widespread Use Today</i>						
STD 80	20	10/56	0.28-1.4	0.125(3.2)	0.5(12.7)	TTL
STD 32	20	24/136	0.84	0.05(1.27)	0.5(12.7)	TTL
VME 6U	21	12/192	0.93	0.1(2.54)	0.8"(2.03)	TTL
Multibus	21	20/86	1.2	0.156/0.1 (3.9/2.54)	0.6(1.52)	TTL
Multibus II	21	38/192	0.93	0.1(2.54)	0.8(2.03)	TTL
<i>New Designs</i>						
Futurebus (F)	14	256/384+pwr	0.46	0.078(2.0)	1.18(30.0)	BTL

Table 1.2: Selected Backplanes: key physical/mechanical/electrical characteristics.

There are obviously many other characteristics that define backplanes, but these are in constant flux and change too fast to be put on a table. A typical example is live insertion: the ability to insert a PCB without affecting data traffic on the backplane and without damaging the electronics on the inserted or any other PCB. Live insertion has become increasingly important ⁽²¹⁾ over the past few years. Newer standards like Futurebus+ prescribe it ⁽¹⁶⁾ and many companies are offering retrofits to allow live insertion even in backplanes whose standards previously did not offer live insertion ⁽²²⁾ (such as VME).

Nonetheless, the survey of electronic backplanes in this section indicates that the available electronic backplanes have very different characteristics which can be used in different applications. The next section indicates that all electronic backplanes, by their very nature, face fundamental physical and engineering limits which impose diminishing returns on any further research time and effort invested to overcome these limits.

1.4 Cost/performance limitations of electronic backplanes

In this section, an analysis is performed indicating that limitations of electronic backplanes will be increasingly difficult to overcome in a cost-effective manner. The cost is shown to be increasing in terms of power consumption, fabrication complexity, valuable real estate on a PCB edge, and ergonomic usability.

1.4.1 Transmission line effects

In order to analyze the electrical performance of high performance electronic backplanes, traditional lumped element analysis is not valid: all components must be modeled using transmission line models. Furthermore, a key point that arises from the following discussion on transmission line models of backplanes is the difference between, on one hand, a bare (unloaded) backplane trace which is often just a microstrip or strip line on a dielectric, and, on the other hand, a loaded backplane trace which is electrically in contact with plated through holes (PTHs) for PCB connector pins, the PCB pins themselves, traces leading from the PCB drivers to the backplane trace, and drivers themselves. The difference in electrical properties between unloaded and loaded traces is considerable.

The following section will analyze the electrical performance of unloaded and loaded backplane traces using the transmission line models shown in Figures 1.2 a) and b) respectively.

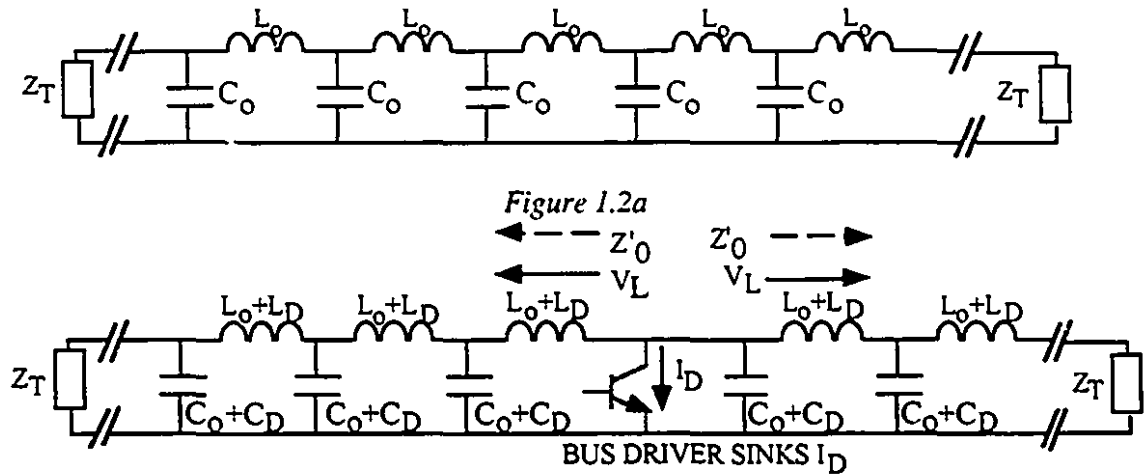


Figure 1.2a) Unloaded backplane trace where L_o and C_o respectively represent the distributed inductance and capacitance along the trace, and Z_T represents the termination impedance b) Loaded backplane trace where L_D and C_D respectively represent additional inductance and capacitance due to PTHs, PCB pins, drivers and so on. One driver is also shown.

Two assumptions will be made during the following analysis 1) The backplane is fully loaded, which means that there is a PCB in every slot. This is justifiable since racks in high performance systems such as telecommunications switches are always as full as possible. Furthermore, dummy boards can always be inserted into empty slots in order to ensure a more uniform characteristic impedance across a trace and to simplify calculations for cooling air flow in a chassis. 2) All traces analyzed are identical traces for high-speed data transmission. Consequently, analyzing one trace is equivalent to analyzing all traces, except for certain calculations such as crosstalk.

A key parameter defining a transmission line is its characteristic impedance Z_o . For an unloaded, ideal, and lossless transmission line,

$$Z_o = \sqrt{\frac{L_o}{C_o}} \quad \Omega \quad (1.1)$$

where L_o and C_o are respectively the distributed inductance and capacitance along the trace and have units of H/m and F/m respectively.

However, the characteristic impedance for a fully loaded transmission line is different: an additional distributed capacitance, C_D , and inductance, L_D , must be added to the model, although in traditional backplane transmission line modeling, the smaller effect of L_D is neglected for characteristic impedance and related calculations ⁽²³⁾. (The effect of L_D is mainly apparent in crosstalk calculations). The characteristic impedance of a loaded backplane trace, Z_o' is thus:

$$Z_o' = \sqrt{\frac{L_o}{C_o + C_D}} \quad \Omega \quad (1.2)$$

When a driver sinks or drives a current I_o onto a trace of length l , the driver 'sees' an impedance of Z_o' in parallel with Z_o' , or an equivalent impedance of $Z_o'/2$. Therefore, the voltage created by the current pulse is:

$$V_o = I_o \times Z_o' / 2 \quad (1.3)$$

The current will propagate along the trace with a velocity v_p ⁽²⁴⁾:

$$v_p' = 1 / \sqrt{L_o(C_o + C_D)} \quad (1.4)$$

and will reflect at the termination impedance Z_T ; this reflected current will be added to the original current. The reflection coefficient ρ indicates how much of the pulse will be reflected and is a function of both Z_T and Z_o' :

$$\rho = \frac{Z_T - Z_o'}{Z_T + Z_o'} \quad (1.5)$$

At this point, it is instrumental to look at a numerical example. While numerical values of the above-mentioned parameters vary widely depending on geometry, material, and fabrication, typical values can nonetheless be used. A typical PCB trace has a distributed capacitance $C_o = 65.8$ pF/m and distributed inductance $L_o = 0.658$ μ H/m; the additional capacitance due to PTHs, drivers, pins, and other sources of capacitance is on the order of 30 pF. Assuming 45 boards/m and using Eq. (1.2), $Z_o' \approx 20 \Omega$ ⁽²³⁾. Consequently, in order to drive a 3V swing on the trace, the driver must drive a current of $I_D = 3V/(20/2) = 300$ mA. However, a standard TTL driver cannot drive more than 50-100 mA and as such the initial current wavefront will create an unacceptably small voltage. Consequently,

several round trips (i.e. reflections off the termination) will have to be made before the signal can be sampled. The successive reflections building up the voltage are illustrated in Figure 1.3.

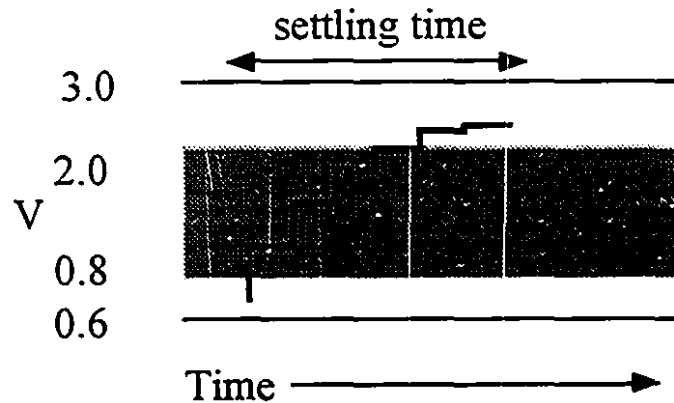


Figure 1.3: Additive effect of successive reflections of a current pulse off Z_T ⁽²³⁾.

For a trace of length $l = 0.5\text{m}$ and a current pulse requiring 2 round trips to settle, the total settling time is: $2 \times 2l / v_p = 61 \text{ ns}$. This settling time, however, is dependent on driver technology, fabrication, material and so on. The VME standard, for example, specifies a settling time of 35 ns during which the lines may not be sampled⁽¹⁶⁾.

As a result of these transmission line effects, many extensive (and expensive) efforts have been made to calculate and impose strict controls on the choice of backplane material, geometry, drivers and fabrication in order to control all the parameters on transmission lines and as such increase data throughput by reducing settling times, unwanted reflections, signal skew, and so on^(25,26,27,28). However, the cost of such controls is high, and backplanes whose specifications embrace such strict controls, such as Futurebus+ which has been discussed and proposed for over ten years now^(22,29), have found only limited acceptance in the marketplace as companies are reluctant to pay considerably more for a product that promises revolutionary gains in throughput but presently offers only incremental cost/performance gains over existing products such as VME⁽³⁰⁾. Transmission line effects are thus one of many engineering problems which act as a limiting factor for electronic backplane cost/performance improvements.

1.4.2 Energy and power requirements

As the characteristic impedance, Z_o' decreases, the amount of current drive required for a voltage swing ΔV on a trace increases, which increases total power consumption. The signal energy E_s for one bit in a properly terminated transmission line is ⁽³¹⁾:

$$E_s > \frac{V^2}{Z_o'} \tau \quad (1.6)$$

Table 1.3 indicates typical power consumption of various drivers. (BTL: Backplane Transceiver Logic, a specification for carefully controlled backplane environments ⁽²⁶⁾). The table further indicates that as the number of lines increases, an option which certain standards are contemplating in order to increase throughput ⁽¹⁸⁾, the heat dissipated by the drivers becomes comparable to or greater than that produced by high performance microprocessors, such as, for example, the Pentium's 16 W or the DEC Alpha's 30 W ⁽³²⁾.

Driver	Max power/driver, mW	Max power for 256 lines, W
TTL (no Z_T)	72	18.4
BTL	89	22.76
ECL	134	34.3

Table 1.3: Power requirements for backplane drivers, per board.

The termination impedances at the end of the traces also contribute to heat along the backplane. VME traces, for example, are terminated with a real equivalent termination impedance of 194Ω to $3V$. This results in an additional source of heat of up to 46 mW at each end of a trace.

For optical interconnects, on the other hand, the minimum signal energy E_{so} for one bit is a function of the wavelength λ , the photodetector's quantum efficiency β , the capacitance of the receiver C_D , the voltage which must be developed across a resistor R , and the efficiency of the interconnect η_i . For $RC_D > \tau$ ⁽³¹⁾:

$$E_{so} = \frac{hcC_D V}{\eta_i \beta \lambda e} \quad (1.7)$$

where $h=6.626 \times 10^{-34}$ J-s, $c = 2.998 \times 10^8$ m/s, and $e = 1.602 \times 10^{-19}$ C.

While a comparison of the heat produced by different types of interconnects depends on many factors, studies nonetheless indicate that beyond a certain throughput-distance product, electronic interconnects consume more power than optical interconnects (33,34). The simplified graph in Figure 1.4, for example, indicates that for a 1 Gb/s transmission rate, the break-even distance at which an electrical interconnect consumes more power is of the order of 1 cm, further indication that optical interconnects over backplane distances are more advantageous than electrical interconnects. While Figure 1.4 neglects negligible optical power losses as a beam propagates through air and minor losses at all optical surfaces, the graph still indicates that optical interconnects are more energy-efficient than electronic interconnects for links over backplane distances.

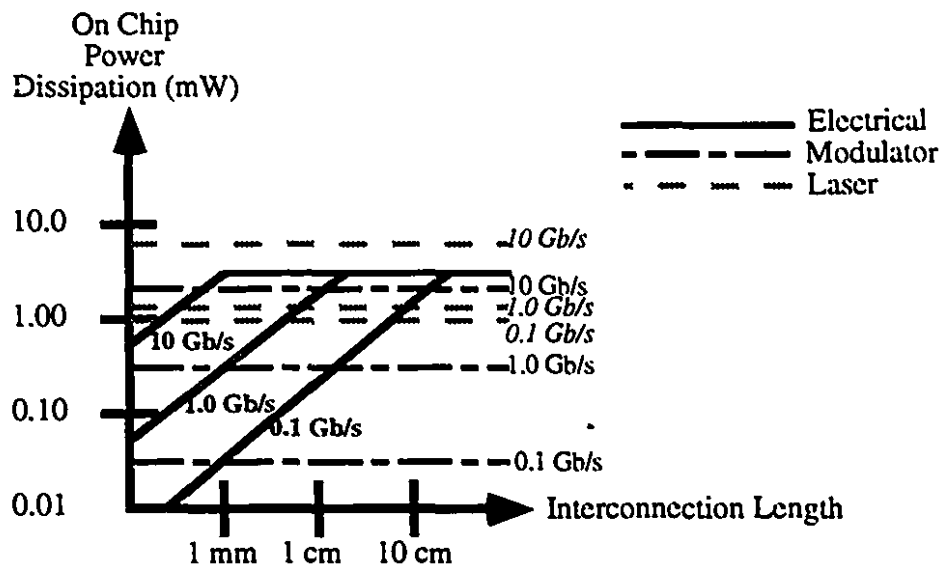


Figure 1.4: Comparison of power dissipation per I/O for various lengths and transmission schemes⁽³³⁾.

1.4.3 Limitations of separable electronic interconnects

A reliable separable interconnect which allows repeated insertion and extraction (I/E) of PCBs into and out of the backplane is, by the very definition of a backplane, a necessity.

Traditional high performance PCB-backplane connectors consist of pins on the PCB (backplane) which mate into appropriate receptacles on the backplane (PCB). As was outlined in section 1.4.1, a negative aspect of pins and their associated plated through holes (PTHs) is that they contribute substantial additional capacitance and inductance which affect Z'_o , thus changing the transmission line environment of the electronic backplane trace.

However, most importantly, the crosstalk between adjacent pins on a ~2 cm long connector is substantial when compared to the crosstalk between adjacent signal lines in the controlled environment of the backplane itself ⁽³⁵⁾. High performance pinned connectors are obliged to insert ground pins between the signal-carrying pins in order to limit crosstalk to acceptable levels, as shown in Figure 1.5. The ratio of signal pins to ground pins, the signal:ground ratio (SGR), is a key parameter for PCB-backplane connectors. For example, 4 row connectors with pins on a 0.100 inch (2.54 mm) grid (a typical value today) have a pin density of 40 pins/linear inch of PCB edge (as shown in Figure 1.5). However, if there are no ground pins, pulses having a 500 ps risetime will generate an unacceptable crosstalk of 25% on adjacent pins⁽³⁶⁾. If a 2:1 SGR is prescribed for such connectors in order to lower crosstalk to acceptable levels (shown in Figure 1.5), then the number of true signal carrying pins falls to $2/3 \times 40 = 26$ /linear inch (1.02/ mm).

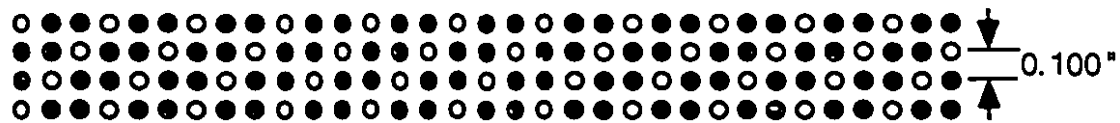


Figure 1.5 Pin allocation scheme for a 4 row connector showing a 2:1 SGR (solid dot: signal pin; hollow dot: ground pin) and featuring 40 contacts per linear inch of PCB edge, only 26 of which are actual signal carrying pins.

While equations for determining the actual crosstalk are extremely complex functions of signal rise time, pin length, SGR, fabrication and material⁽³⁷⁾, many theoretical and experimental studies have been performed which indicate a very rapidly diminishing return on total data throughput (total number of pins \times data rate/pin) over a PCB-backplane connector when the SGR is reduced^(35,37,38). For example, reducing the SGR from 7:1 to 2:1 (a 175% increase in the number of ground pins) on a modern top-of-the-line controlled impedance pinned connector results in an increased data throughput of only 30% for the entire connector⁽³⁵⁾.

Furthermore, increasing the number of pins increases the force required to physically insert a PCB into its appropriate receptacle on the backplane: one high performance pin requires a 0.46 N insertion force ⁽³⁹⁾. Consequently, ergonomic arguments alone eliminate the possibility of adding thousands of pins to a PCB-backplane connector.

Finally, an increased number of connector I/Os creates a diminishing return in electronic backplane production since yields fall due to the fabrication complexities brought about by increased PTH density and more demanding PTH geometry ⁽⁴⁰⁾.

In order to bypass these problems associated with pinned PCB-backplane connectors, many different types of PCB-backplane connectors have been studied or produced. A summary of these is shown in Table 1.4.

Despite all these improvements, reliable separable electronic interconnects still cannot offer considerably more than 2500 pin-outs for a 10 inch wide PCB, and again, the tradeoff between signal speed and grounding constraints very quickly reduces the overall throughput or cost effectiveness or both of a connector onto an electronic backplane.

Type	Signal contacts per linear inch of PCB edge	Comments
HDC ⁽⁴¹⁾ (High Density Connector)	100	AT&T design; conducting polymer accommodates play between connecting gold dots on module and backplane.
Metal and/on elastomer ⁽⁴²⁾	200	Low density due to high area requirements, contact resistance higher.
Area Array ⁽⁶⁾	100	S shaped conductors in elastomer matrix; good wiping mechanism.
Button ⁽⁴³⁾	250	Compressed wire forms a spring; wire can be any metal (gold, copper); zero insertion force; daisy-chain boards.
stripline ⁽⁴⁴⁾ connector	100	Ground shell around the plug provides ground planes around all pins, higher SGR.
BetaPhase ⁽⁴⁵⁾	32 high speed	Beta Phase connector for Apple's Quick Ring& others; impedance on each line individually controlled; high-speed point-to-point links.
Coax Matrix ⁽⁴⁴⁾	141 coax	Insertion time very long; research discontinued by Molex Inc. due to lack of interest.
Gold Dot ⁽⁴⁶⁾	100	Controlled impedance; offers flex circuitry as well.
ASC ⁽⁴⁴⁾ (Application Specific Connector)	132	Flexible film, easily reconfigurable.

Table 1.4: Proposed and emerging non-pinned high throughput PCB-backplane connectors.

1.5 Optical backplane demonstrators

For data transfer over backplanes, it can be seen that optical interconnects have few of the limitations of electrical interconnects: 1) the optical equivalent of electronic transmission line effects, namely reflections at optical surfaces, is simpler to analyze and quantify than electronic transmission line effects, and can be greatly reduced by anti-reflection (AR) coatings on the surfaces, 2) optical interconnects have lower skew and require less energy per bit, and 3) optical signals do not suffer from crosstalk proportional to signal pulse

frequencies since photons, unlike electrons, do not usually interact with each other in free-space and conventional materials. Consequently, researchers have explored optical backplanes, either in free-space^(47,48,49) or in guided-wave media^(50,51,52). As well, off-the-shelf fibre-optic backplane connectors are now available⁽⁵³⁾, or are being designed⁽⁵⁴⁾, although these tend to be quite big (the ferrule alone of a conventional fibre optic connector is usually 2.5 mm in diameter), and wiring and routing problems present in electronic backplanes are also present in fibre-based backplanes. In general, free-space optical links have an advantage over guided wave links in that an effectively unlimited number of architectures can be implemented; furthermore, the parallelism and interconnectivity of optics facilitate the implementation of structures requiring global communication ^(55,56).

In order to fully exploit the advantages of free-space optical interconnects, the McGill photonic systems group is presently designing and building a free-space optical backplane demonstrator, a simplified rendition of which is shown in Figure 1.6 ⁽⁵⁷⁾. Such a system will offer massive connectivity between removable PCBs along the backplane. However, if this free-space optical backplane is to achieve and maintain reliable operation, certain key problems must be solved. One of the many key problems that must be solved is the alignment of the smart pixel arrays with each other along the free-space optical communication channels in the optomechanical support structure. Since the PCBs in Figure 1.6 are to be inserted manually, the task of achieving and maintaining proper alignment tolerances will be critical.

All the optical backplane products or demonstrators mentioned above which function outside a controlled laboratory environment require sophisticated mechanical retaining systems to maintain proper alignment tolerances between the smart pixels (or other transceivers on the PCBs) and the optical channels on the backplane. These sophisticated mechanical systems are either bulky (which reduces I/O density and as such the total data throughput) or increase the required insertion force, or both.

Active alignment is a closed-loop control process in which system parameters such as throughput or error in image position are monitored and fed back to a controller which realigns the system by altering the state of optics. This technique may be used to preserve the alignment tolerances in all axes within a high density separable optical interconnect, and is the subject of this thesis.

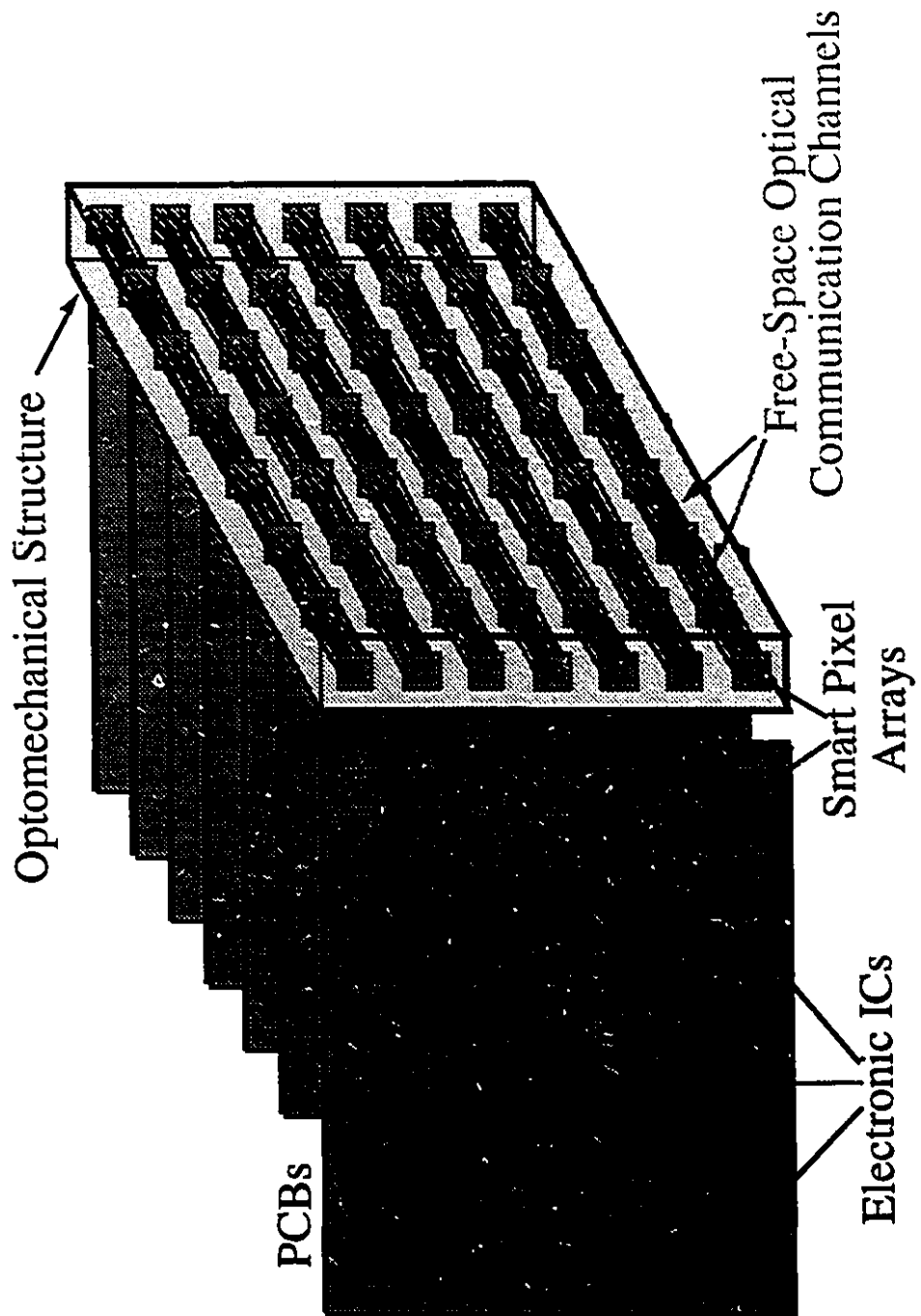


Figure 1.6: Rendition of free-space optical backplane designed by McGill Photonic Systems group.

1.6 Organization of the thesis

The thesis outline is as follows. Chapter 1 demonstrates that conventional backplanes implementing electronic interconnects are rapidly encountering fundamental limitations which will prevent any major economical performance improvements in the future. Backplanes implementing free-space optical interconnects are shown to be an advantageous alternative. Chapter 2 indicates that the performance of free-space optical backplanes will be seriously hampered if the optical interconnects are misaligned. The six different mechanical misalignments in free-space optical interconnects, namely lateral misalignment in the x-y-z directions and rotational misalignment about the x-y-z axes, are analyzed, and it is shown that active alignment is one solution to overcome these misalignment problems. Chapter 3 further defines active alignment and describes existing active alignment systems that have been reported and described in depth, such as those found in space observation telescopes and CD players. The review of existing systems shows that active alignment is an emerging multidisciplinary field in which optical, electrical, mechanical, and computer engineering are all important. Furthermore, the review reveals many concepts that are applicable for active alignment in free-space optical backplanes in digital systems

In order to determine the complexity of constructing an active alignment system which requires such multidisciplinary contributions, it was decided to design, simulate, build, and test an active alignment system which could ultimately fit into the above-described free-space optical backplane demonstrator built by the McGill Photonic Systems Group in conjunction with the National Research Council. Chapter 4 describes the theoretical underpinnings and the main centering algorithms of the active alignment system, which uses Risley Beam Steerers (RBSs) to re-align an interconnect which had been misaligned in the x-y directions. Chapter 5 describes the fabrication and characterization of the system. Chapter 6 describes the experimental results, and chapter 7 gives future directions for research in active alignment.

1.7 References

- [1] R. R. Tumala and E. J. Rymaszewski, Microelectronics Packaging Handbook, Van Nostrand Reinhold, New York (1989).
- [2] T.C. Banwell, R.C. Estes, S.F. Habiby, G.A. Hayward, T.K. Helstern, G.R. Lalk, D.D. Mahoney, D.K. Wilson, and K.C Young, "Physical design issues for very large ATM switching systems", *IEEE J. Selected Areas in Comm.*, **9**, 1227 (1991).

- [3] IEEE Std 583, *Modular Instrumentation and Digital Interface System(CAMAC)*, (1982).
- [4] M. B. Raynham and D. M. Thom, "The EISA Connector", *Hewlett-Packard Journal*, 42, 73, October (1991).
- [5] R. M. Cram, *Microcomputer Busses*, Academic Press, San Diego (1991).
- [6] J. DiGiacomo, *Digital Bus Handbook*, McGraw-Hill Publishing , New York , 1990.
- [7] S. Muchmore, "A comparison of the EISA and MCA architectures", *Electronic Engineering*, 91, March (1989).
- [8] J. D. Mosley, "Bypass the PC bus to speed up your system", *EDN*, 38, 65, 18 February (1993).
- [9] PCI Revision 2.0, *Peripheral Component Interconnect Local Bus Specification* (1993).
- [10] M. J. Dougherty, "A SEM-E module avionics computer with PI-bus backplane communication", *Proc. IEEE National Aerospace and Electronics Conference*, 169 (1990).
- [11] K. Griffin, "VHSIC phase 2 test requirements for the depot" *Proc. AUTOTESTCON*, 289, (1989).
- [12] Data Translation Inc. Publication UM11355B *DT-Connect II Standard* (1992).
- [13] P. Ponting and H. Verweij, "Instrumentation buses for high energy physics, past , present, and future", *IEEE Transactions on Nuclear Science*, 38, 322 (1991).
- [14] IEEE Std 960, *Fastbus Modular High Speed Data Acquisition system* (1989).
- [15] STD 32 Special Interest Group Publication, "STD32: Compact High Performance Computers for Control" (1993).
- [16] IEEE Std 1014, *VMEbus* (1987).
- [17] W. Fischer, "VMEbus and VME64", *Proc. Buscon West*, 171 (1992).
- [18] IEEE Std 896.1, 896.2, *Futurebus+ physical layer and profile specifications* (1987).
- [19] D. B. Gustavson, "The Scalable Coherent Interface and related standards projects", *IEEE Micro*, 11, 10, February (1992).
- [20] J. Regula, "The proposed SSBLT standard doubles the VME64 transfer rate", *IEEE Micro*, 11, 64, February (1992).
- [21] B.P. Aichinger, "Futurebus+ as an I/O bus: profile B", *Computer Architecture News*, 20, 300, (1992).
- [22] W. Andrews, "Extender board brings live insertion to VME systems", *Computer Design* , 31, 120, August (1992).
- [23] R. V. Balakrishnan, "The proposed IEEE 896 futurebus – a solution to the bus driving problem", *IEEE Micro*, 3, 23, August (1984).

- [24] S. Ramo, J. R. Whinnery, T. VanDuzer, Fields and Waves in Communication Electronics, John Wiley and Sons, Toronto, (1984).
- [25] D. Telian, "Treat pc-board traces as transmission lines to specify drive buffers", *EDN*, 38, 129, 2 September (1993).
- [26] IEEE Std 1194, *Backplane Transceiver Logic* (1991).
- [27] R. Lipp, "LTL: A high performance CMOS transceiver technology". Paper 1.4.1, *Proc. Hot Interconnects I* (1993).
- [28] R. A. Quinnell, "High-speed bus interfaces", *EDN*, 38, 43, 30 September (1993).
- [29] P. L. Borrill, "A Comparison of 32-bit buses", *IEEE Micro*, 4, 71, December (1985).
- [30] W. Andrews, "Futurebus+ conformance: Part paper, part reality", *Computer Design*, 33, 65, February (1994).
- [31] H. S. Hinton, An Introduction to Photonic Switching Fabrics, Plenum Press (1993).
- [32] L. Geppert, "The new contenders", *IEEE Spectrum*, 30, 20, December (1993).
- [33] R. A. Nordin, F.J. Levi, R.N. Nottenburg, J. O'Gorman, T. Tanbun-Ek, and R. A. Logan, "A systems perspective on digital interconnections technology", *J. of Lightwave technology*, 10, 811 (1992).
- [34] P. J. Ayliffe, J. W. Parker, and A. Robinson, "Comparison of optical and electrical data interconnections at the board and backplane levels", *Proc. SPIE: Optical Interconnections and Networks*, 1281 (1990).
- [35] R. Lord and S. Auja, "High density backplane connector", *Interconnection Technology*, 10, 8 January (1994).
- [36] D. M. McNamara, "A high density, flex circuit based, pressure interconnect system for high speed backplane applications", *Proc. International Electronics Packaging Conference* (1991).
- [37] M. Hayward, "Backplanes for bus systems", *Proc. Buscon East*, 153 (1988).
- [38] N. Sugiura and K. Yasuda, "A high-density multipin connector for high speed signal transmission in a rack system", *Proc. 41st Electronic Components and Technology Conference*, 256 (1991).
- [39] J. M. B. Van Woensel, "A design review of a 2mm pitch high density connector system", *Proc. 41st Electronic Components and Technology Conference*, 245 (1991).
- [40] H. Lawrence, "Noise margin budgeting and backplane design", *Electronic Product Design*, 13, 31, September (1992).
- [41] K. S. Akkapeddi, "The design of some novel 0.05in grid high-density circuit pack-to-backplane connectors" *Proc. 39th Electronic Components and Technology Conference*, 92 (1989).

- [42] L. S. Buchoff, "Solving high density electronic problems with elastomeric connectors", *Proc. National Electronics and Packaging Conference*, 3 (1990).
- [43] S. MacCorquodale, "Button connectors – solderless, low-thermal rise interconnect for high-speed signal transmission", *Interconnection Technology*, 6, 25, August (1990).
- [44] F. Caruthers, "High-performance connectors enter system spotlight", *Computer Design*, OEM-15, September (1993).
- [45] Molex Inc., Beta-Phase Connector system, May, 1992.
- [46] Hughes Interconnect Inc. publication (1993).
- [47] M. Feldman, "Holographic optical interconnects for multichip modules", *Electronic Engineering*, 64, 49, September (1992).
- [48] K. Hamanaka, "Integration of free-space interconnects using selfoc lenses: image transmission properties", *Jpn. J Appl. Phys.*, 31, 1656 (1992).
- [49] R. C. Kim, E. Chen, and F. Lin, "An optical holographic backplane interconnect system", *J. Lightwave Technology*, 9, 1650 (1991).
- [50] C.T. Sullivan, B. L. Booth, and A. Husain, "Polymeric waveguides", *IEEE Circuits and Devices*, 8, 27, January (1992).
- [51] R. T. Chen, "Cross-link induced linear and curved polymer channel waveguide arrays for massively parallel optical interconnects", *Spie Vol. 1774 Nonconducting photopolymers and applications*, 1992.
- [52] M. Verghese, "Comparison of electrical and optical free-space and waveguide backplanes", and references therein, *Proc. Topical meeting on logic devices and systems*, 216, McGill University Course 304-688, H. S. Hinton ed. (1993).
- [53] For example, Molex Inc. Fiber optic product catalog 1093 (1992).
- [54] R. J. Pimpinella, "A new type of fiber optic connector designed for military optical backplanes", *Proc. 42nd Electronic Components and Technology Conference*, 643, (1992).
- [55] T. Szymanski and H. S. Hinton, "Architecture of a terabit free-space photonic backplane", *Proc. Optical Computing 94*, accepted for publication.
- [56] B. Robertson, Free-Space Holographic Optical Interconnects in Dichromated Gelatin, Ph. D. Thesis, Physics Department, Heriot Watt University, Edinburgh (1993).
- [57] D. V. Plant, B. Robertson, W. M. Robertson, T. H. Szymanski, H. S. Hinton, G. C. Boisset, P. Desai, S. Gagnon, M. Kim, N. H. Kim, Y. S. Liu, M. R. Otazo, D. R. Rolston, A. Z. Shang, M. Shmaitelly, and B. Supmonchai, "Phase II optical backplane demonstrator functional specifications", Canadian Institute for Telecommunications Research, 1994 Technical conference.

Chapter 2

Alignment constraints within a free-space optical backplane

2.1 Introduction

In order for a free-space optical backplane to function properly, the transmitter and receiver planes must always remain aligned to each other regardless of the surrounding environmental and physical conditions. In addition, this alignment must be maintained after repeated mechanical insertions and withdrawals of the PCBs. Consequently, if practical free-space optical backplanes are to be designed and built, alignment tolerances must be fully quantified, and the impact of environmental, physical, and mechanical conditions on these tolerances must be fully understood.

The following chapter is organized as follows. In section 2.2 a preliminary analysis of optical misalignment mechanisms and alignment tolerances which affect a backplane based on a 'generic' lenslet-array based free-space optical interconnect is presented. The analysis indicates that even slight mechanical misalignments can severely affect system performance.

Section 2.3 outlines the harsh conditions that exist within a backplane environment and presents, as an example, a basic optical engineering dilemma in which problems of mechanical, thermal, and physical rigidity often have solutions which adversely affect optical integrity and vice versa.

Finally, section 2.4 presents the conflict between the tight alignment tolerances that a free-space optical system must respect and the looser mechanical tolerances that are present in the separate interconnects of existing backplanes.

In conclusion, it is argued that active alignment is a solution to the problem of preserving the alignment of a free-space optical backplane in which the cumulative effect of physical and mechanical conditions can lead to mechanical misalignment.

2.2 Basic misalignment mechanisms

Most free-space optical systems are designed to image an array of focused signal beams, or spots, onto an array of optoelectronic devices^(1,2). For optimal performance, the optical and optomechanical system must ensure that these signal beams remain properly aligned with respect to the device array. In addition, the interconnect must be designed to

minimize the amount of aberration introduced by the optics. This section will discuss the main misalignment mechanisms by which a spot array can be misaligned with respect to a device array in order to give an idea of required alignment tolerances. For this analysis, the interconnect shown in Figure 2.1 will be studied, in which light from a power supply is reflected off a plane of transmitter devices, and is imaged by a telecentric $4f$ lenslet array system onto a device array on the receiver plane. The lenslet array is assumed to be made up of square lenslets having dimension $D \times D$.

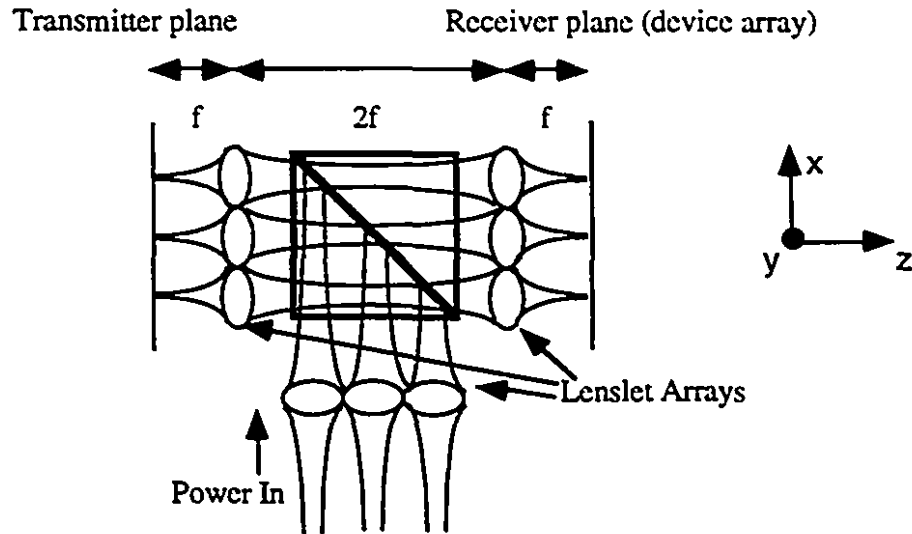


Figure 2.1: Optical interconnect studied to determine impact of misalignments.

Figure 2.2 shows the six degrees of freedom of an object in space, such as an array of devices: three linear directions, x , y , z , and three rotational directions, θ_x , θ_y , θ_z .

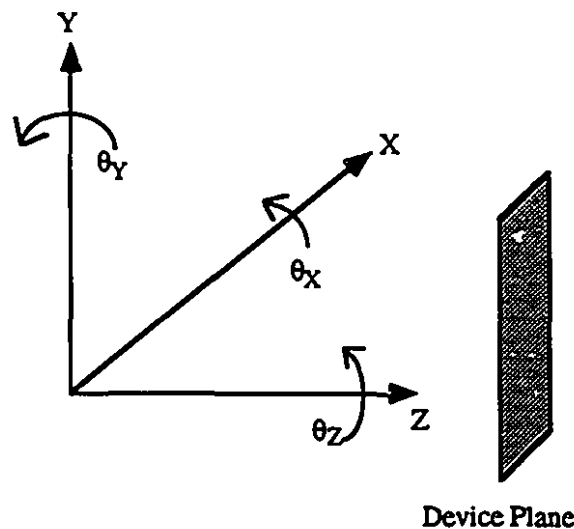


Figure 2.2: Six degrees of freedom of an object in space.

In the following analysis, it is assumed that each focused signal beam has a Gaussian irradiance pattern $I(x,y)$. If $(\Delta x_e, \Delta y_e)$ is the misalignment between the centre of the irradiance pattern and the centre of the device, then

$$I(x,y) = I_0 e^{-2[(x-\Delta x_e)^2 + (y-\Delta y_e)^2]/w_0^2} \quad (2.1)$$

where the power outside the circle of radius w_0 is only 13.5% (e^{-2}) of the total power contained within the beam. The integral of the irradiance over the device area is equal to the total power coupled into the device and is an important parameter since the switching speed for many classes of devices such as SEEDs (Self Electro-optic Effect Device) is directly related to the total power coupled into the device (3).

It is further assumed that the device array is an $N \times N$ array with each device being a square of dimensions $a \times a$, and the centre-to-centre distance being D , as shown in Figure 2.3. The spot array is also assumed to be an $N \times N$ array with centre-to-centre distance of D . For all misalignment calculations performed below, the impact of varying w_0 will also be studied, when relevant.

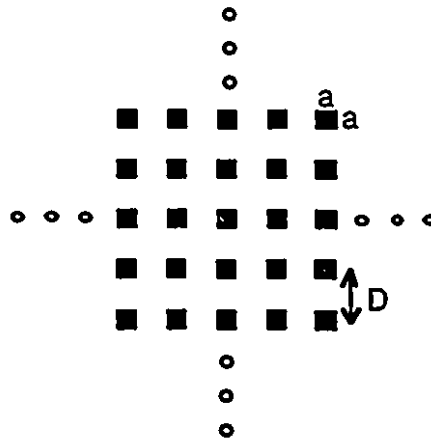


Figure 2.3: Geometry of device array.

The following subsections show the impact of mechanical misalignments along each of the above directions. Unless otherwise specified, in all cases it will be assumed that the optics and emitter are perfectly aligned and that only the receiver plane has a misalignment error.

2.2.1 Misalignment in the x-y plane

As will be shown in Chapter 4, the total light power coupled into a device of size $a \times a$ is the integral of the irradiance over the device area:

$$P = I_0 w_0^2 \frac{\pi}{8} \left\{ \operatorname{erf} \left[\frac{(a/2 - \Delta x_e)}{w_0 / \sqrt{2}} \right] - \operatorname{erf} \left[\frac{(-a/2 - \Delta x_e)}{w_0 / \sqrt{2}} \right] \right\} \times \left\{ \operatorname{erf} \left[\frac{(a/2 - \Delta y_e)}{w_0 / \sqrt{2}} \right] - \operatorname{erf} \left[\frac{(-a/2 - \Delta y_e)}{w_0 / \sqrt{2}} \right] \right\} \quad (2.2)$$

where w_0 is as defined above. A plot of the change in total light power coupled into the device for misalignment errors along the x-direction is shown in Figure 2.4. By symmetry, similar displacements along the y-direction produce the same results. It is interesting to note that for a small Δx_e error, more power is coupled into the receiver when the spots are small (small w_0) than when the spots are larger (larger w_0). However, beyond a certain displacement, the total power coupled rolls off more rapidly for a small spot than for a large spot. Therefore, smaller spots have better maximum power coupling, but are more vulnerable to large misalignments than are larger spots.

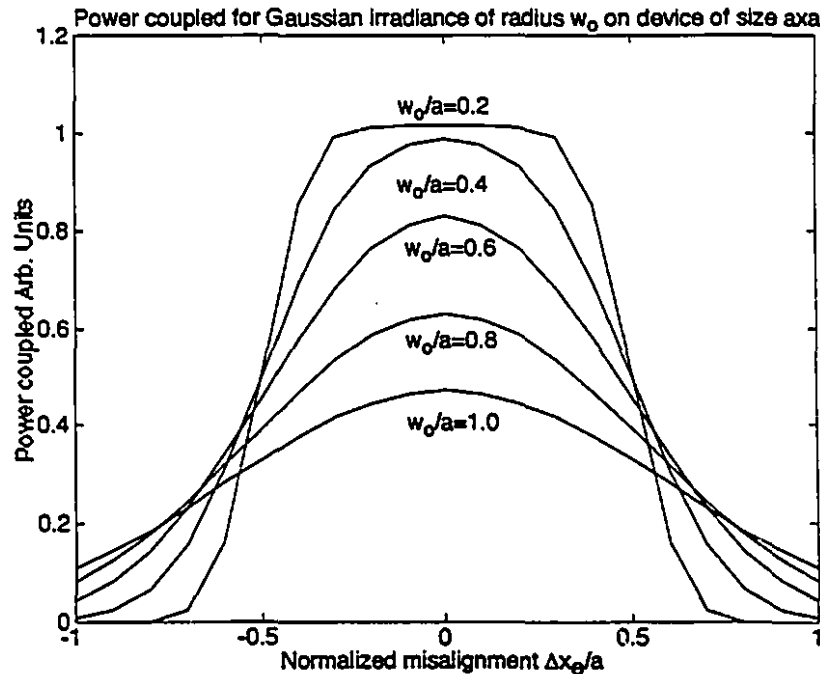


Figure 2.4: Normalized change in power coupled into a device for a misalignment along the x-direction.

2.2.2 Misalignment in the z-direction

When the device array is misaligned along the z-direction, the error will just cause a defocus and a widening of the spot since the system was defined to be telecentric. This is shown in Figure 2.5. This will cause the spots to be larger than their optimal value.

The spot is smallest at the beam waist, and has a diameter (e⁻² power) $2w_0$:

$$w_0 = \frac{\lambda f}{\pi w} \quad (2.3)$$

where w is the radius of the beam at the front focal plane.

For a displacement of Δz_e away from the beam waist, the radius $w(\Delta z_e)$ of a spot is given by (4):

$$w^2(\Delta z_e) = w_0^2 \left[1 + \left(\frac{\lambda \Delta z_e}{\pi w_0^2} \right)^2 \right] \quad (2.4)$$

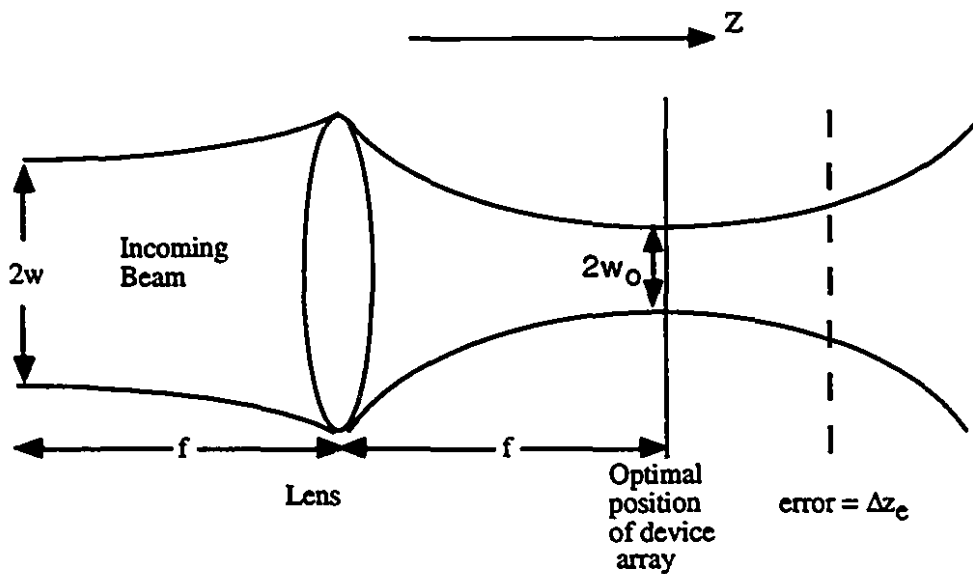


Figure 2.5: Misalignment error along the z direction.

A plot indicating the change in total light power coupled into the device for misalignment errors along the z-direction is shown in Figure 2.6. It can be seen that a beam with a smaller initial w_0 couples more power into the receiver when the misalignment error Δz_e is small. However, the total power coupled rolls off more slowly for a given

defocus when w_o is larger, which is to be expected since a beam with a smaller w_o diverges faster than a beam with a larger w_o .

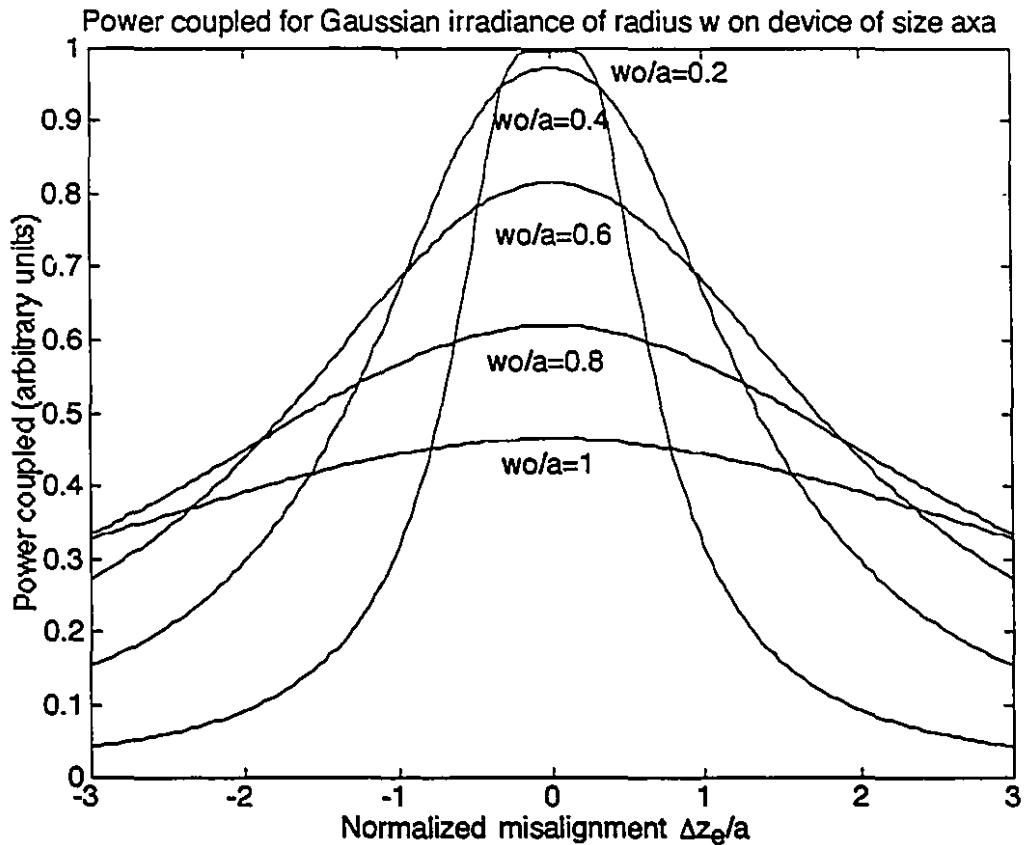


Figure 2.6: Change in total power coupled for normalized values of Δz_e and w_o .

2.2.3 Tilt about the x and y axes

For the interconnect in Figure 2.7, a tilt of $\Delta\theta_x$ about the x-axis at the array centre will cause the light reflected off the transmitter plane to be reflected at an angle of $2\Delta\theta_x$ from its nominal (untilted) direction. Assuming a negligible defocus for small $\Delta\theta_x$, the beam of light impinging on the lenslet array A will have a lateral misalignment error of Δy_e where

$$\Delta y_e = f \tan(2\theta_x) \quad (2.5)$$

If the interconnect is such that for an angular misalignment of $\Delta\theta_x = 0$ the (99% power) beam diameter $3w_o = D$, where D is the length of a side of square lenslet, then any

Δy_e misalignment will increase the clipping, leading to a loss of power transmitted to the receiver plane.

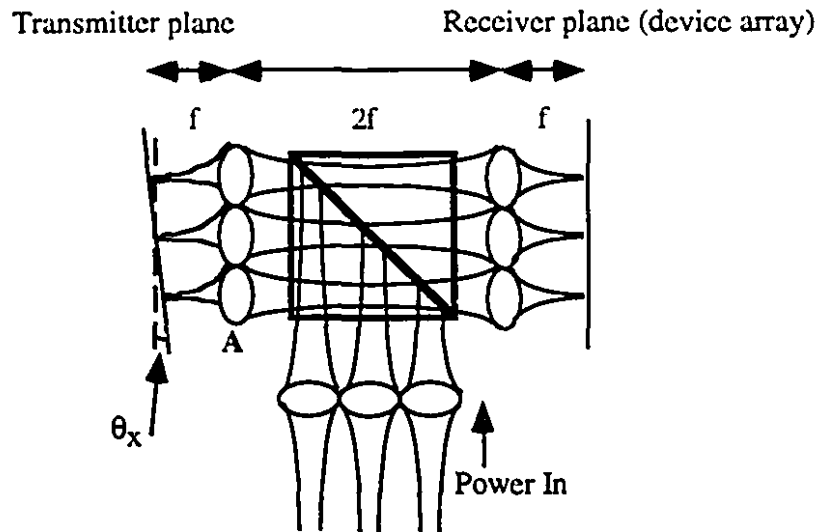


Figure 2.7: Effect of tilt $\Delta\theta_x$ on beams reflected from transmitter plane.

Given the symmetry of the setup, an analogous result is obtained for $\Delta\theta_y$.

Plots of total power coupled at the receiver plane vs misalignment error $\Delta\theta_x$ are shown in Figure 2.8. In the plots, D is kept constant at $3w_o$, and the focal length of the lenslet is changed. It can be seen from Figure 2.8 that the loss of coupled power increases as the lens' focal length increases.

The above analysis is valid only for small angles $\Delta\theta_x$, $\Delta\theta_y$, since the difference between the ideal distance travelled and the actual distance travelled, which can be expressed as a Δz_e error and which is shown in Eq. (2.4) to be a parameter determining the spot size, is small.

The $\Delta\theta_x$, $\Delta\theta_y$ errors in tilt described above are especially serious in interconnects using lenslet arrays such as the present model, and must carefully be studied in order to determine the angular misalignment tolerance of such systems ⁽⁵⁾.

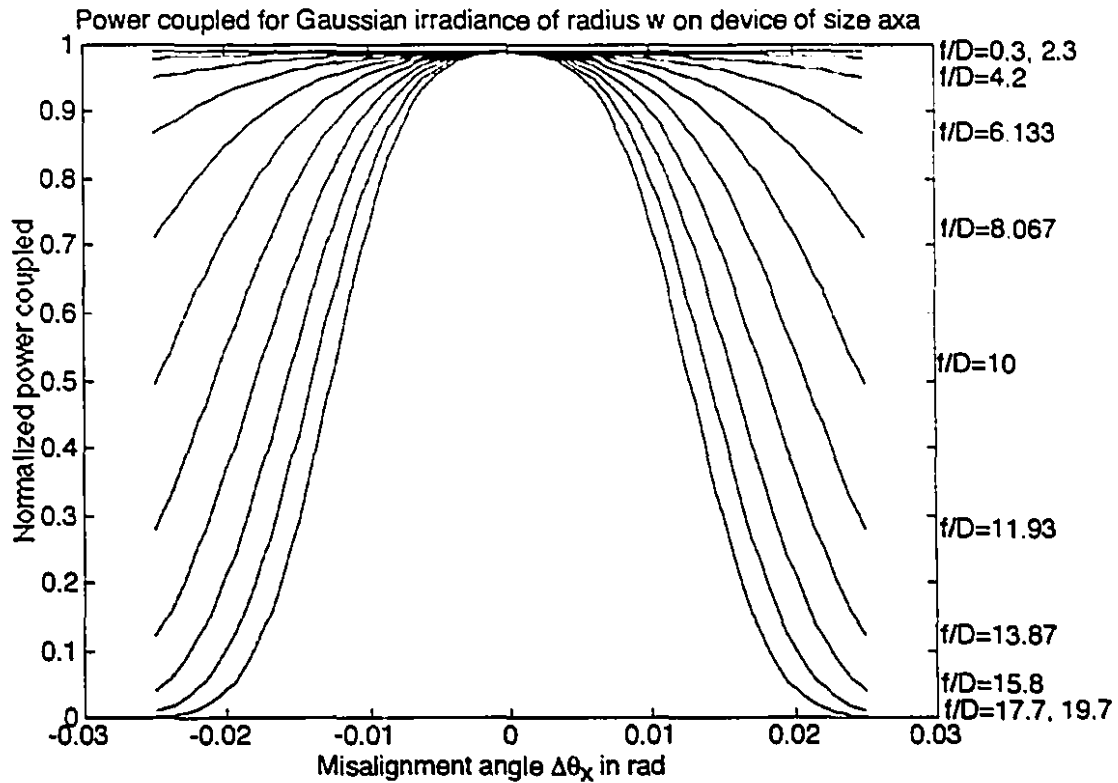


Figure 2.8: Effect of $\Delta\theta_x$ tilt of modulator on power coupled by receiver device.

2.2.4 Rotation about the z-axis

A rotation $\Delta\theta_z$ of the spot array about the z-axis coincident with the centre of the device array, as shown in Figure 2.9, results in a circular translation of the spot array about the x-y plane. The devices farthest from the centre, one of which is labelled p in Fig 2.9, will be the most affected by the rotational displacement.

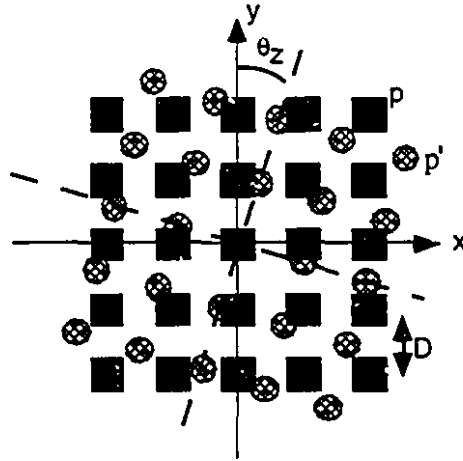


Figure 2.9: Effect of $\Delta\theta_z$ rotation of spot array relative to device array.

If an $N \times N$ device array with centre-to-centre spacing of D is properly centered with respect to a spot array of the same dimensions, then both the farthest device and the farthest spot are at point $(x_p, y_p) = (r, r)$ where $r = D \times N / 2$ (for even N).

If the spot array is rotated by $\Delta\theta_z$ relative to the device array, the position of the device is unchanged but the position of spot p' (x'_p, y'_p) in Figure 2.9 becomes

$$(x'_p, y'_p) = (r[\cos(\Delta\theta_z) - \sin(\Delta\theta_z)], r[\cos(\Delta\theta_z) + \sin(\Delta\theta_z)]) \quad (2.6)$$

A plot of power coupled vs $\Delta\theta_z$ is shown in Figure 2.10. Again, the smaller spot is less sensitive to smaller displacement than to large displacements and the larger spot is less sensitive to all displacements. The value $r = 180a$ corresponds to a 32×32 array having a centre-centre spacing of $D = 8\sqrt{2}a$. In order to couple at least 90% of the power for such a case, the $\Delta\theta_z$ error must be under 0.001 rad (0.057°)— a formidable packaging and alignment challenge.

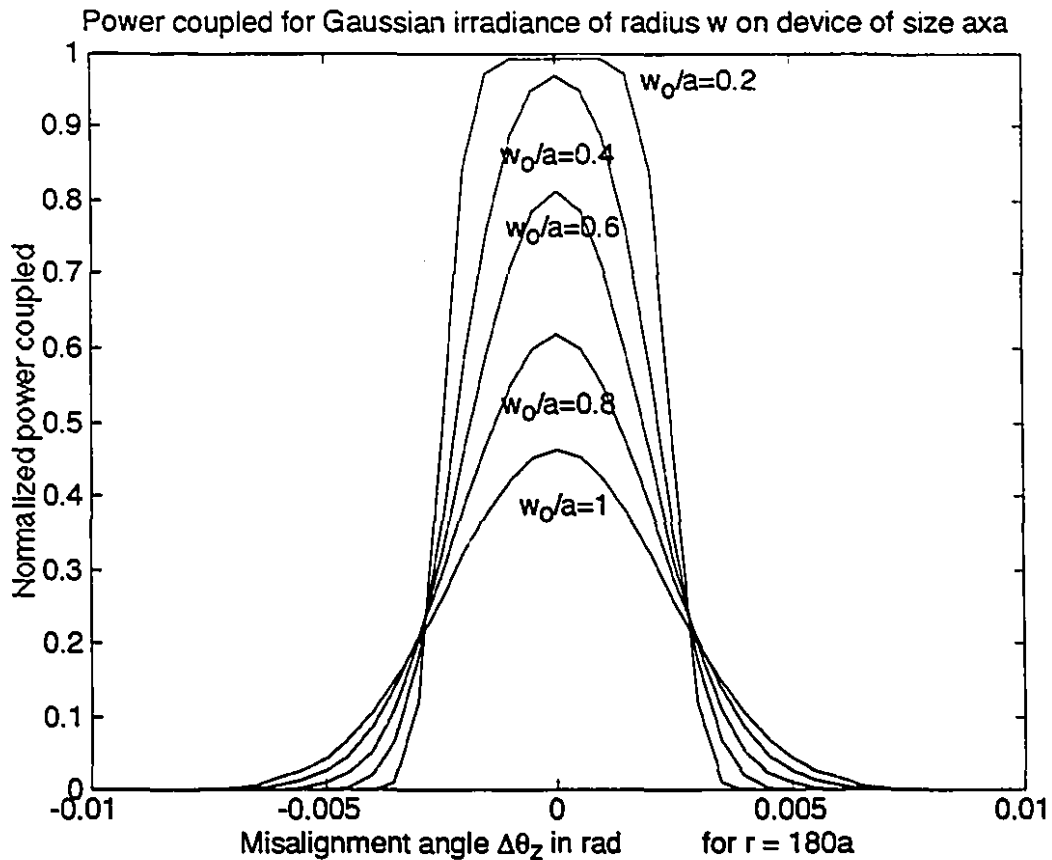


Figure 2.10: Effect of $\Delta\theta_z$ misalignment error on power coupled into device for $r=180a$.

2.2.5 Further comments on misalignment mechanisms

The above analyses only study misalignment from a mechanical viewpoint: they do not take into account misalignments brought about by optical effects. For example, optical contributions to misalignment in the x-y plane include: lack of telecentricity in a defocused system, distortion not equal to $f \sin\theta$ for a spot array produced by a Binary Phase Grating (BPG), magnification of the spot array image brought about by a mismatch of the focal length of lenses in an imaging system, and spot displacement due to a change in wavelength in a spot array produced by a BPG⁽⁶⁾. These must be added to the mechanical misalignment when determining alignment tolerances.

The above analyses also do not take into account optical crosstalk, a situation in which part of the power intended for one device is coupled into an adjacent device. However, the analysis in Chapter 4, in which the power coupled into adjacent detectors is calculated, is very similar to such crosstalk calculations.

In addition, these analyses just look at individual misalignments and do not take into account different combinations of misalignment, which is a complex problem.

Having performed a theoretical analysis of the effect of misalignment errors, it is instrumental to look at an actual demonstrated system and its numerical alignment tolerances in order to better appreciate the issues. For System₄, an AT&T free-space photonic switching demonstrator⁽⁷⁾, $(\Delta x_e, \Delta y_e, \Delta z_e) = (0.5 \mu\text{m}, 0.5 \mu\text{m}, 3 \mu\text{m})$, $(\Delta\theta_x, \Delta\theta_y, \Delta\theta_z) = (20', 20', 2')$. The analyses clearly indicate the serious impact of even minor mechanical misalignments in a free-space optical system. As such, in typical high-performance optical systems, the initial assembly requires much pre-aligning. Even after such pre-aligning, installing one hardware module on a demonstrator requires several minutes of adjusting various components⁽⁷⁾.

This section considered the importance of the alignment of optics. The following section outlines the real environmental conditions in which an optical backplane system must operate and how these conditions affect the optics and their mechanical alignment.

2.3 Effect of the harsh conditions in a backplane environment on optomechanics

A basic problem which all optomechanical engineers must face is the difficult compromise between mechanical rigidity and optical integrity.

On one hand, physical mechanisms such as thermal gradients and fluxes can introduce axial and radial stresses which distort the lenses or other optical components. This distortion can harm image quality, induce birefringence, and, ultimately, damage the optics⁽⁸⁾. Consequently it is desirable that the optomechanics apply a minimum of force on the component or that the component be held with flexible or elastic retaining mechanisms.

On the other hand, given the forces a backplane is subjected to and the vibrations to which it is exposed, a lens or optical component must be held as tightly as possible in order to preserve the initial system alignment and prevent misalignments described in the previous section.

This dilemma is further outlined in this section. The analysis below concentrates on circular lenses in circular cells, but similar analyses are applicable to other optical components such as lenslet arrays or planar optics since most optical components in free space optical systems are glass components mounted in analogous optomechanical mounts and subjected to similar physical conditions^(9,10).

2.3.1 Thermal effects: mechanical stress on optics

Commercially available advanced electronic microprocessors can operate in temperatures ranging from 0 to 85 °C ⁽¹¹⁾. Military specifications are even more stringent, specifying the operating and storage temperatures to be between -55°C and 85°C, and between -62 °C and 125 °C respectively ⁽¹²⁾. Since photonic backplanes are expected to complement, not replace, electronics, it is reasonable to assume that thermal specifications for photonic interconnects will have to match those for electronics.

For a lens mounted in a simplified cell whose dimensions are specified in Figure 2.11, an increase in ambient temperature will cause the lens and simplified cell to expand at rates determined by their relative Coefficient of Thermal Expansion (CTE). If the CTEs are not matched, both the lens and the cell will be subjected to stress. The stress on the lens is of most concern to the system designer since the lens' condition will affect the quality of the beam; the axial stress, S_{Ga} , and radial stress, S_{Gr} , are specified by equation (2.7) ⁽⁸⁾:

$$S_{Ga} = \frac{(\alpha_B - \alpha_G)E_G E_B \Delta T}{E_G + E_B} \quad (2.7a)$$

$$S_{Gr} = \frac{(\alpha_B - \alpha_G)\Delta T}{\left[\frac{1}{E_G} + \frac{r}{E_B \times t} \right]} \quad (2.7b)$$

where

- 1) t and r are defined in Figure 2.11,
- 2) α_g and α_M are the CTEs of the cell metal and the lens glass respectively,
- 3) E_g and E_M are Young's Modulus for the cell metal and the lens glass respectively,
- 4) and ΔT is the change in ambient temperature.

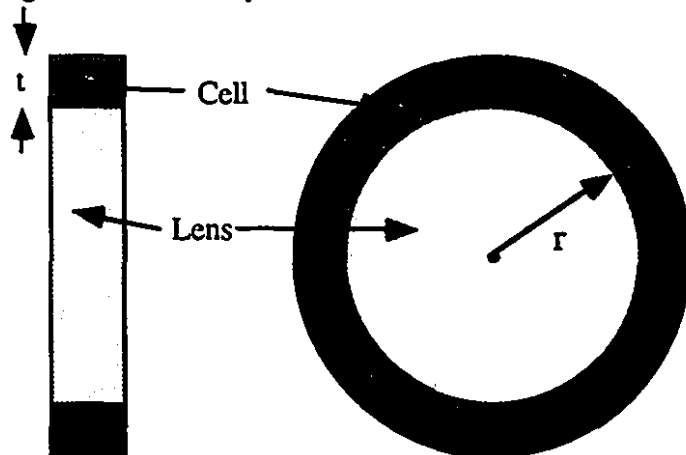


Figure 2.11 Geometry of lens and simple cell for thermal-induced stress calculations.

As an example, it is worth considering a lens holder used in a prototype optical backplane (Phase I, McGill-NRC). This lens holder ⁽¹⁰⁾ is shown in Figure 2.12. The inner cell has a thickness $t = 1.49$ mm and is made of 416 steel which has $E_M = 1.994 \times 10^{11}$ N/m² and $\alpha_M = 9.9$ ppm/°C. A lens fitting into that cell has a radius $r = 9$ mm and is made of BK7 which has $E_g = 8.135 \times 10^{10}$ N/m² and $\alpha_g = 7.1$ ppm/°C.

If the lens is to be held using a drop-in mounting technique with a sliding fit, which is the case for the lens element in the Phase I system, then the force holding the lens must be axial, as indicated in Figure 2.12. Assuming a sliding fit, letting $\Delta T = 80$ °C, and substituting into Equation (2.7b), the axial stress on the glass component is found to be $S_{Gr} = 12.9 \times 10^6$ N/m². While this stress is less than the ultimate compressive strength of glass (3.5×10^8 N/m²), this stress is still much greater than the recommended operating limit of 3.5×10^6 N/m² for BK7 and as such will cause birefringence which will degrade the optical performance for systems in which the polarization of light must be controlled^(8, 13).

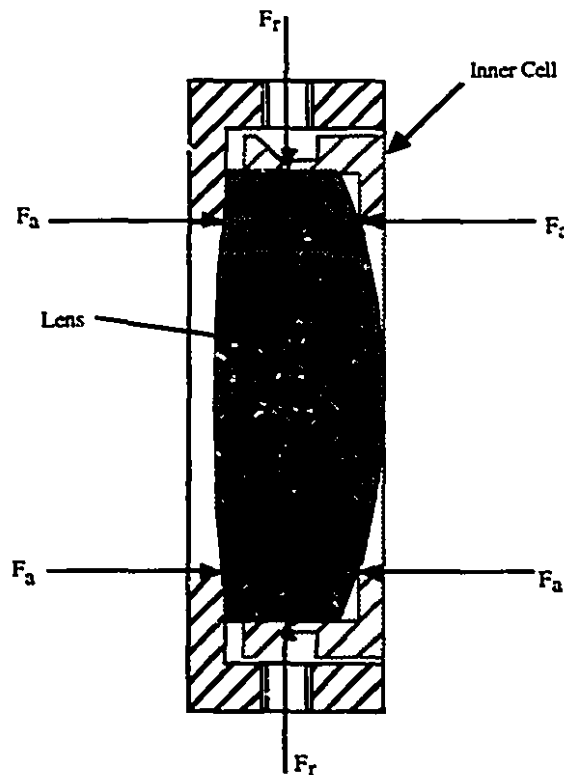


Figure 2.12: Lens in realistic cell and holding forces exerted on lens in cell. F_a : axial force; F_r : radial force. Usually, only one type of force is present.

If, on the other hand, a lens is to be hard mounted, then there must be an interference fit (no clearance) between the lens OD (Outer Diameter) and the cell ID (Inner Diameter). As such, the resulting interference fit will cause the force holding the lens to be radial, as

shown in Figure 2.12. Again assuming $\Delta T = 80^\circ\text{C}$ and substituting into Equation (2.7b) yields the result $S_{Gr} = 5.26 \times 10^6 \text{ N/m}^2$. While this stress is much less than the maximum compressive strength of glass, it is still 50% greater than the recommended operating limit of $3.5 \times 10^6 \text{ N/m}^2$ for BK7 and as such will also cause birefringence and image degradation.

It should be noted that birefringence will be most harmful in systems employing polarized light, such as those in which polarized beam-splitters or retarders are used.

One way to remedy the above problems is athermalization, a process in which the lens and cell materials are carefully chosen so as to minimize the difference in CTE between the two materials and as such reduce thermal-induced stress. However, athermalization increases design complexity by limiting the choice of lens and barrel material available to the designer⁽¹⁴⁾. As well, many of the common metals having a CTE matching that of commonly used glasses, such as steel, titanium, or beryllium, are expensive or hard to machine or both⁽⁸⁾.

Another remedy to thermal-induced stress effects consists of gluing a component into a cell. Specific thicknesses of elastomers can accommodate thermal expansion. This solution, however, entails an assembly that is considerably more complex and time consuming^(15,16).

2.3.2 Thermal Effects: movement of optics

The preceding subsection indicated how thermal fluxes create stress on optics. However, there is also the possibility of actual movement of optics due to thermal expansion, which is specified by a material's CTE. An interesting example to study is the baseplate on which Phase I is mounted, a simplified engineering drawing of which is shown in Figure 2.13. The baseplate is made of magnesium AZ31B, which has a CTE of $25.2 \text{ ppm}/^\circ\text{C}$ ⁽¹⁷⁾. For a $\Delta T = 80^\circ\text{C}$, the baseplate's thickness will increase from its nominal 25.4 mm (1 inch) thickness to $25.4 + 25.4 \times 25.2 \times 10^{-6} \times 80 = 25.451 \text{ mm}$, an increase of $51 \text{ }\mu\text{m}$. For a system such as system₄ described above which has a tolerance on Δx_e of only $0.5 \text{ }\mu\text{m}$, the impact of this thermal movement on the optical performance is sufficient to render the system effectively non-functional.

Other thermal effects include the effect of a temperature change on the index of refraction of a lens and as such on its focal length. These effects are also quite small, however, and are mostly of the order $10^{-6} \text{ mm/mm}/^\circ\text{C}$ ⁽¹⁴⁾. Nonetheless, these thermal induced problems accumulate and can cause misalignment problems.

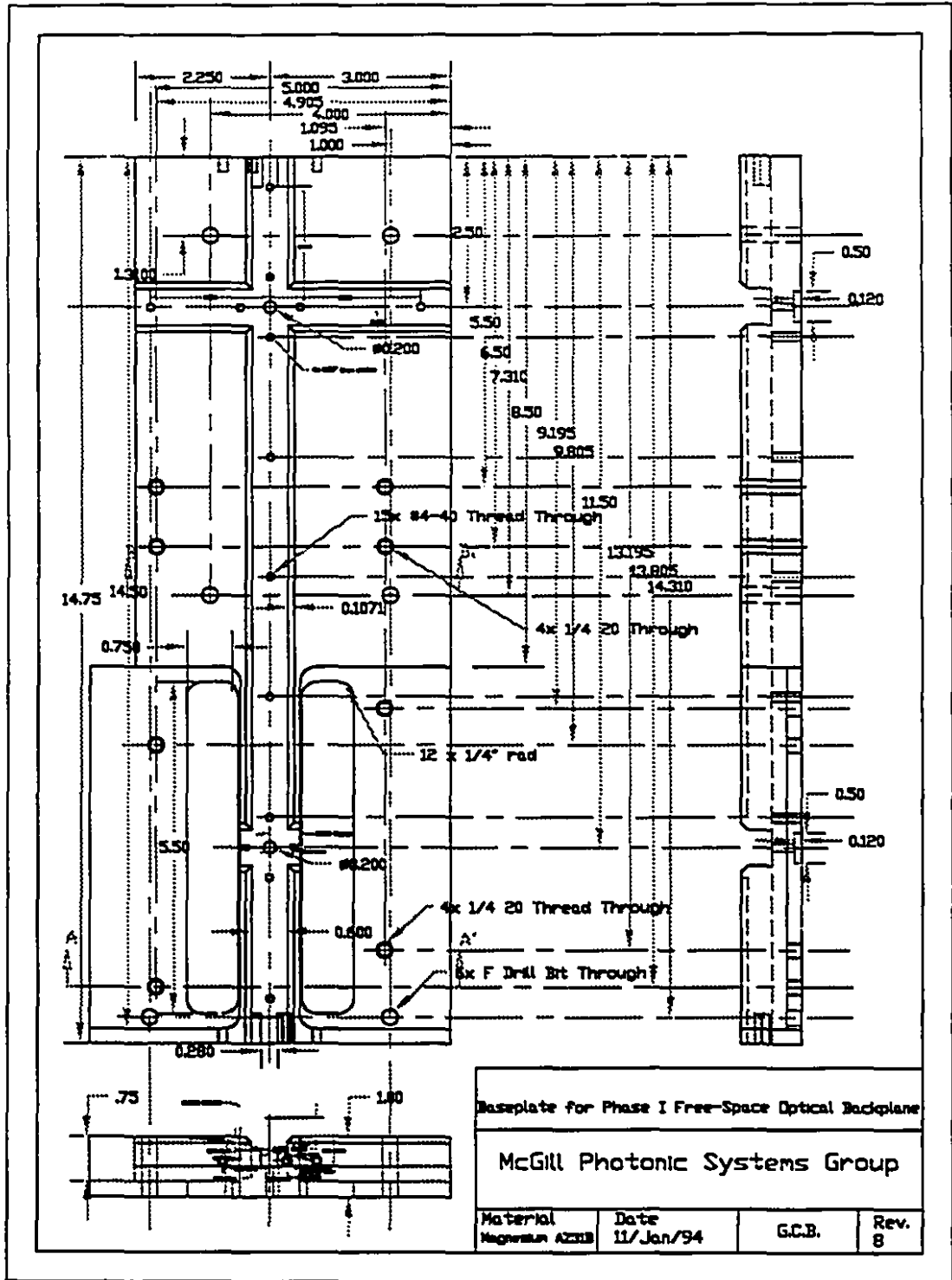


Figure 2.13: Simplified engineering drawing of McGill Phase I baseplate.

2.3.3 Vibration and shock

In most high-performance computing environments the backplane is located in a chassis in which fans blow a considerable volume of air over the PCBs and the backplane transceivers. A fully loaded Futurebus+ chassis, for example, must have fans blowing between 119 and 161 litres of air per second in order to meet the cooling specifications⁽¹⁸⁾. On average, these fans rotate at angular speeds of up to 3200 rpm (~60Hz)⁽¹⁹⁾. These requirements are mainly driven by the electronics on the PCBs and as such any backplane standard must respect them. The resulting vibrations from the fans and accompanying massive airflow must be considered in all photonic backplane system designs.

Traditional techniques developed to accommodate shock and vibrations, such as the use of springs, rubber pads, or other tensioned or elastic elements should not be used since they are susceptible to drift⁽⁷⁾. For vibrational analysis, such soft mounts can be modelled as springs having linear resonance frequency, f_{lr} , and angular resonance frequency, f_{ar} , described by⁽²⁰⁾:

$$f_{lr} = \frac{1}{2\pi} \sqrt{\frac{K_L}{M_L}} \quad (2.8a)$$

$$f_{ar} = \frac{1}{2\pi} \sqrt{\frac{K_A}{I_A}} \quad (2.8b)$$

where K_A and K_L are the angular and linear spring constants respectively, and I_A and M_L are the moment of inertia or mass of the oscillating bodies.

If the frequency of the disturbances such as the cooling air or fans matches the fundamental frequency of the tensioned element, resonance will occur, which can seriously damage or even destroy the element. As a result, it is recommended that the resonant frequency be at least three times greater than the disturbing frequency⁽²¹⁾. Even for nonresonant modes, wear and relative motion will cause a premature aging of the components. For these reasons, tensioned mounts, which are acceptable and used in other optical systems, are unacceptable in a backplane environment given the rough vibration conditions.

Another problem is the force required to insert a PCB into the backplane environment. For Futurebus+, this force is of the order of 200N⁽¹⁸⁾. Furthermore, this insertion force is perpendicular to the backplane, which is unusual in optical design: in most optical systems exposed to high shock, such as sights on rifles or missile tracking heads, the optics are parallel to the main shock vector⁽²²⁾. Shocks perpendicular to the optics further complicate

optomechanics. A typical example of this complication is the fact that unthreaded rings tend to back out of engagement after shocks, forcing the designer to forgo such components (22).

2.4 Consequences of board insertion on mechanical specifications in backplane chassis

While tomorrow's photonic backplane standards are in no way obliged to respect the mechanical specifications of today's electronic backplane standards, today's specifications are nonetheless a reflection of the physical and industrial environment in which backplanes must reliably operate and as such are worthy of study.

As was outlined in chapter 1 and shown in Figure 2.14, most backplane standards today explicitly specify that the backplane itself be mounted in a metal chassis which offers protection from environmental, mechanical, electromagnetic and other disturbances. A PCB is usually inserted into the backplane by sliding the PCB along guide rails which run along the inner sides of the chassis, as shown in 2.14. The guide rails ensure that the connectors on the PCB mate with the appropriate receptacle on the backplane.

The separation of the rail's edges shown in Figure 2.14 must be kept relatively large in order to accommodate PCBs of varying thicknesses. Futurebus+ specifies a rail edge separation of 2.90 ± 0.1 mm and PCBs of thickness between 1.4 and 2.57 mm in order to allow for PCBs of various thicknesses to slide down the chassis and mate into the backplane; as well, maximum warpage must be kept to below 0.6 mm (peak to valley) over the entire length of the board, which is 297 mm. For a perfectly rigid board of minimal (1.4 mm) thickness, the tilt of the board would be of the order of $\Delta\theta_y = \arcsin [(2.9 - 1.4)/297] = 0.29^\circ$. Moreover, alignment pins on the PCB are specified such that the total lateral play in the y-z direction is $\pm 100 \mu\text{m}^{(18)}$. These misalignments are large compared to the alignment tolerances required by current free-space optical interconnects.

2.5 Possible solutions to mechanical misalignment

The cumulative result of all the misalignment mechanisms described in this chapter, both those that apply to all free-space interconnects in general as well as those that apply specifically to backplanes, indicate that maintaining the proper alignment of a free-space optical backplane in an industrial environment (as opposed to a controlled laboratory environment) would be challenging.

One way to eliminate these cumulative misalignments would be the extensive athermalization of all components and the construction of extremely rigid, precisely

fabricated, and hard modules in a backplane. Such passive solutions have been implemented before, but these solutions are generally confined to unique or very expensive systems^(22,23,24). Ingenuity in mechanical design, however, could solve these problems. Another way to ensure alignment on the backplane would be to resort to periodic visits by maintenance crews, but this could be an expensive proposition.

A potentially cheaper and more effective way could be to implement active alignment, which is a closed-loop control process in which system parameters such as throughput or error in image position are monitored and fed back to a controller which realigns the system by altering the state of optics. The following chapters will explore the concept of active alignment in order to determine the feasibility and implications of implementing active alignment in free-space optical backplanes.

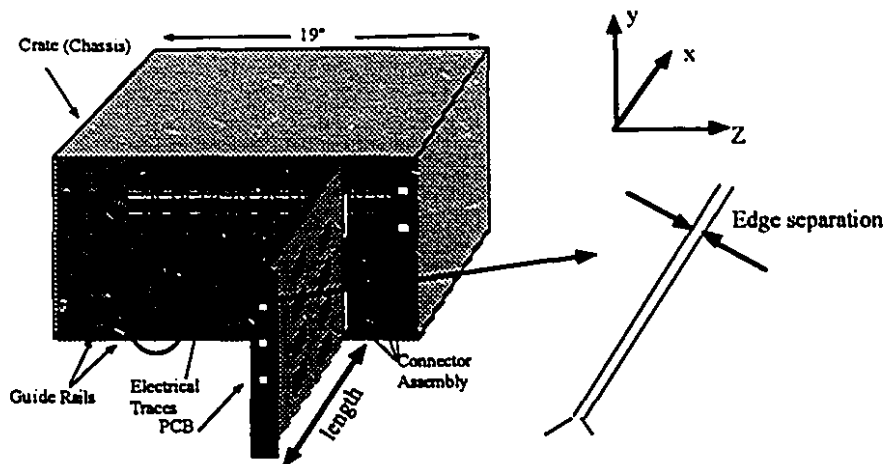


Figure 2.14: Backplane chassis and guide rails.

2.6 Conclusion

This chapter described the negative impact of mechanical misalignments on free-space optical systems and the major physical conditions that can contribute to such mechanical misalignments within a backplane environment.

A combination of all the above sources of misalignment will bring about considerable misalignment which, depending on the optical tolerances, will considerably impair system performance.

Proposed methods of overcoming these misalignment mechanisms included extensive athermalization and rigid fabrication, periodic site visits by maintenance crews, or active alignment. It was argued that active alignment could be potentially cheaper and more effective than the other two solutions. The next chapters will explore active alignment in order to determine its feasibility and practicality for free-space optical backplanes.

2.7 References

- [1] F. B. McCormick, F. A. P. Tooley, T. J. Cloonan, J. L. Brubaker, A. L. Lentine, R. L. Morrison, S. J. Hinterlong, M. J. Herron, S. L. Walker, and J. M. Sasian, "Experimental investigation of a free-space optical switching network by using symmetric self-electro-optic-effect devices", *Appl. Opt.*, **31**, 5431 (1992).
- [2] A. W. Lohman, W. Stork, and G. Stucke, "Optical perfect shuffle", *Appl. Opt.*, **25**, 1530 (1986).
- [3] A. L. Lentine and D. A. Miller, "Evolution of the SEED technology: bistable logic gates to optoelectronic smart pixels", *IEEE J. of Quant. Elect.*, **29**, 655 (1993).
- [4] H. Kogelnik and T. Li, "Laser beams and resonators", *Appl. Opt.*, **5**, 1550, (1966).
- [5] F. B. McCormick, F. A. P. Tooley, T. J. Cloonan, J. M. Sasian, H. S. Hinton, K. O Mersereau, and A. Y. Feldblum, "Optical interconnections using microlens arrays", *J. Opt. and Quant. Elect.*, **24**, 465 (1992).
- [6] F.B. McCormick, Optical and mechanical design issues in free-space optical interconnection and processing, Ph. D. Thesis, Heriot Watt University, Edinburgh, UK (1993).
- [7] F. B McCormick, F. A. P. Tooley, J. L. Brubaker, J. M. Sasian, T. J. Cloonan, A. L. Lentine, R. L. Morrison, R. J. Crisci, S. L. Walker, S. J. Hinterlong, M. J. Herron, "Optomechanics of a free-space photonic switching fabric: the system", *SPIE Proc.*, **1533** , 97 (1991).
- [8] M. Bayar, "Lens barrel optomechanical design principles", *Optical Engineering*, **20**, 181 (1981).
- [9] J. L. Brubaker, F. B. McCormick, F. A. P. Tooley, J. M. Sasian, T. J. Cloonan, A. L. Lentine, S. J. Hinterlong, and M. J. Herron, "Optomechanics of a free-space switch: the components", *SPIE Proc.* , **1553**, 88 (1991).
- [10] S. Wakelin, Design and construction of a free-space digital optical information processor, Ph. D. Thesis, Heriot-Watt University, Edinburgh, UK (1992).
- [11] *Intel 486™DX2 Mechanical and Thermal Guide*, Intel Publication# 7124, September 1993.
- [12] MIL-STD-810E, *Environmental Test Methods and Engineering Guidelines*, 1993.
- [13] W. F. Riley, and L. Zachary, Introduction to Mechanics of Materials, (John Wiley and Sons, Toronto, 1989).
- [14] T. H. Jamieson, "Thermal effects in optical systems", *Optical Engineering*, **20**, 156 (1981).

- [15] R. E. Hopkins, "Some thoughts on lens mounting", *Optical Engineering*, 15, 428 (1976).
- [16] G. E. Jones, "High performance lens mounting", *Quality assurance in optical and electro-optical engineering SPIE Proc.* 73, 9 (1975).
- [17] C. T. Lynch, Handbook of materials science volume II: metals, composites, and refractory materials (CRC Press, Cleveland, 1989).
- [18] IEEE Std 896.1: *Futurebus* (1991).
- [19] Augat Inc. VME/VXI Engineering Design Guide, (1991).
- [20] C. A. Richey, "Acrospace mounts for down-to-earth optics", *Machine Design*, 121, December 12, 1974.
- [21] D. S. L. Duric, "Stability of optical mounts", *Machine Design*, 184, May 23, 1968.
- [22] J. G. Lecuyer, "Maintaining optical integrity in a high-shock environment", *SPIE Proc.* 250, 45 (1980).
- [23] J. P. Mehlretter, "On thermal-optical distortions of glass disks", *Nouv. Rev. Optique*, 10, 93, (1979).
- [24] M. H. Krim, "Design of highly stable optical support structure", *Optical Engineering*, 14, 552, (1975).

Chapter 3

Review of active alignment

3.1 Introduction

In the previous chapters it was shown that free-space optical backplanes could overcome the fundamental throughput limitations inherent in electronic backplanes. It was further shown that in order to fulfill the potential of optical free-space interconnects, one of the problems that had to be addressed was the alignment of a separable interconnect. Given the strict alignment and mechanical tolerances as well as the physical constraints to which an interconnect is subjected, active alignment was shown to be worthy of further study in order to determine its feasibility and practicality in free-space optical backplanes.

It is thus essential to perform a review of existing active alignment systems in order to determine their capabilities and to judge if certain features from these systems can be implemented into an active alignment system for a free-space optical backplane.

The organization of the chapter is as follows. In section 3.2, the concept of active alignment, which was introduced and defined at the end of chapter 2, is further outlined and the basic closed-loop control diagram is given. The field of active alignment is then divided into categories which are consistent with the misalignment mechanisms described in chapter 2 and each category is explored in turn: section 3.3 deals with active alignment for the correction of lateral (x-y-z) errors, section 3.4 deals with correction of angular alignment errors and section 3.5 explores techniques for correcting jitter, which is a rapidly and randomly changing combination of both lateral and angular misalignment. In each section a review is given of representative active alignment schemes that were successfully implemented and published. Finally, section 3.6 defines and explores three key issues confronting all active alignment systems regardless of the misalignment errors they correct: reliability, accuracy, and cost.

3.2 Definition of active alignment

Active alignment can be defined as a closed-loop control process in which system parameters such as throughput or error in image position are monitored and fed back to a controller which realigns the system by altering the state of optics.

All the active alignment systems described in this chapter feature a control loop similar to the one in Figure 3.1 and which has the following features: a means of determining a

misalignment or throughput error, a method for computing the displacement required for one or more actuators to correct the misalignment, and actuators that move the optics to correct for the misalignment.



Figure 3.1: Basic control loop for active alignment.

3.3 X-Y-Z active alignment: compact disk and optical disk players

Compact disk (CD) players are very interesting to study since they are one of the few mass-market and inexpensive optical systems implementing active alignment – such qualities are very important for backplanes. Furthermore, their general principle of operation is well known and published.

In a hard Compact Disk (CD), binary information is encoded into small grooves spaced about $1.6\ \mu\text{m}$ apart. As the CD turns, these grooves pass under a laser beam focused into a spot. The reflectivity of the groove determines how much light is reflected; based on the reflected light power, the decoder decides whether the groove represents 0 or 1. Keeping the rapidly rotating CD aligned to the laser beam spot requires active alignment. A typical optical train for active alignment in a CD is shown in Figure 3.2 a).

In order to keep the CD's grooves aligned in the x-y plane and within the required depth of focus of $\pm 0.5\ \mu\text{m}$ ⁽¹⁾, part of the reflected beam is fed into a quadrant detector, as shown in Figure 3.2b). As can be seen in Figures 3.2b)(i) and (ii), a Δx_e or Δy_e error can be deduced based on the differential light power on each quadrant. Another technique in which two additional beams are required (one on each side) can also be used⁽²⁾.

To determine the Δz_e error, the light incident on the quadrant detector also passes through an astigmatic lens ⁽²⁾. The optical system is designed such that when $\Delta z_e = 0$, the quadrant detector is resting at the focal plane of least confusion ⁽³⁾. On the other hand, when $\Delta z_e < 0$, the defocus of the sagittal rays will cause the spot to appear as in Figure 3.2b)(iii). Conversely, when $\Delta z_e > 0$, the defocus of the tangential rays will cause the spot to appear as in Figure 3.2b) (iv). Again, the controller can deduce the Δz_e error and move the objective lens to correct for the defocus error. The control bandwidth for such a system can approach 1 kHz ⁽⁴⁾.

Recently, the optomechanical design for an air-supported floppy optical disk was proposed ⁽⁴⁾, but its optomechanical design is both more critical and more complex than the

already challenging conventional hard CD's. In order to reduce the optomechanical design complexity, integrated holographic laser/detector CD heads ⁽⁵⁾ as well as molded glass optical elements for focusing servos⁽⁶⁾ have been proposed .

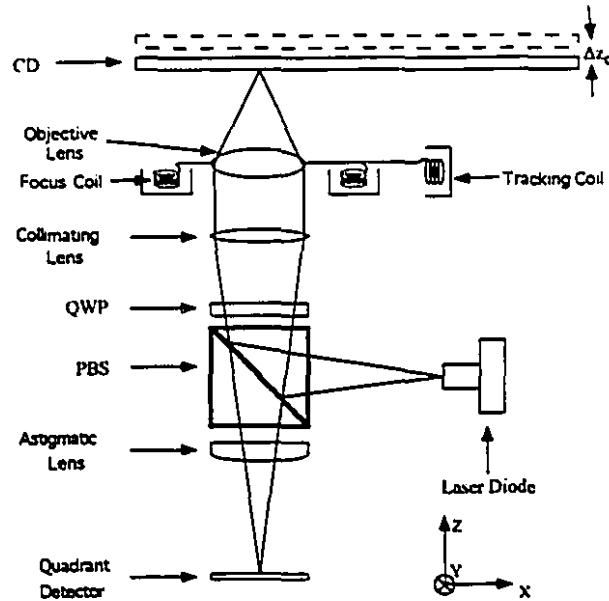


Figure 3.2a): Simplified schematic of optical train for error tracking and active alignment on CD player. QWP: Quarter Wave Plate; PBS: Polarized Beam Splitter.

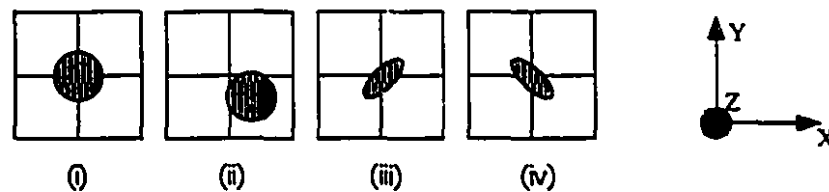


Figure 3.2b): Misalignment errors detected by quadrant detector on CD player:
 (i) $\Delta x_e = \Delta y_e = 0$ (ii) $\Delta x_e > 0, \Delta y_e < 0$ (iii) $\Delta z_e < 0$ (iv) $\Delta z_e > 0$.

3.4 Angular correction: Hubble Space Telescope

The Hubble Space Telescope (HST) is interesting to study since it requires extremely high alignment tolerances and must properly function in harsh thermal and physical conditions in orbit. These harsh conditions, while extreme, make the HST worthy of study since backplanes also must function in difficult thermal and physical environments.

During an observation, the HST line of sight must be stabilized to better than 0.007 arcsec rms in order to achieve the full image resolution which its optics can theoretically

attain⁽⁷⁾. Failure to do so introduces considerable coma in the image. This required stabilization is independent of the large spherical aberration in the primary mirror which was subsequently corrected in a spectacular NASA shuttle mission.

A key challenge is the detection and correction of small angular deviations in the line of sight. A similar challenge, albeit with less demanding tolerances, was shown in chapter 2 to be present for free-space optical backplanes. In order to detect such small deviations, the HST uses an interferometric procedure implementing FGSs (Fine Guidance Sensors) shown in Figure 3.3.

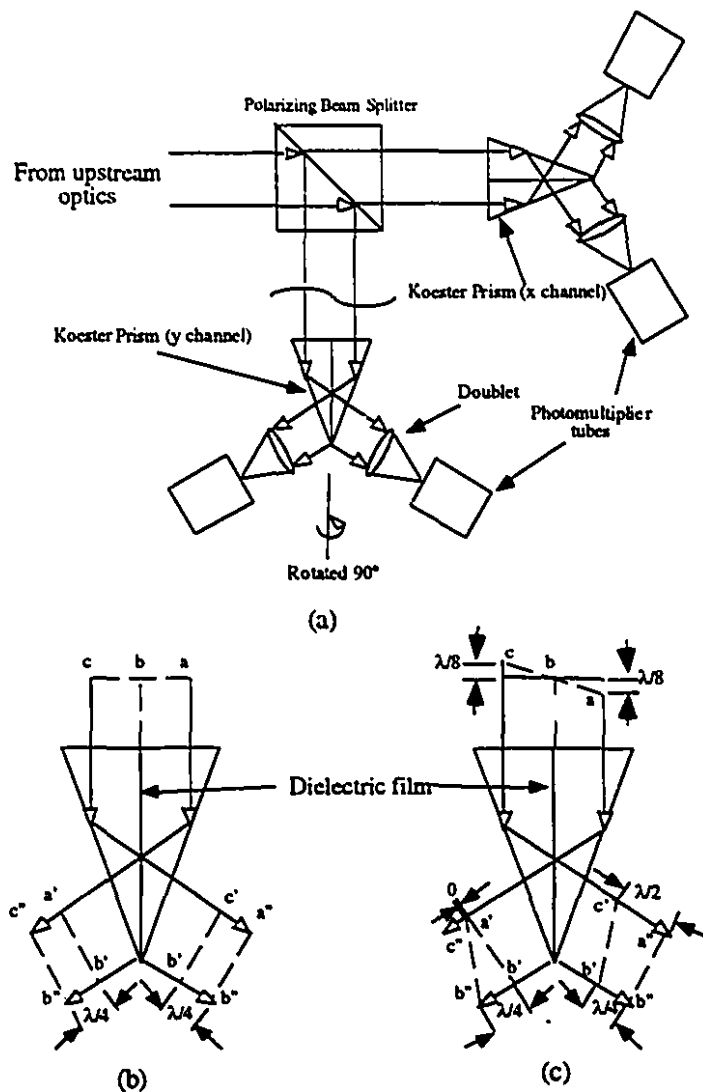


Figure 3.3: a) Simplified schematic diagram of an FGS interferometer optical train ⁽⁷⁾ b) untilted wave front emerging from Koester's prism c) wave front with initial zero to peak tilt of $\lambda/8$ emerging from Koester's prism. Note in b) and c) how reflected component is advanced in phase by $\lambda/4$ relative to transmitted beam component.

In Figure 3.3a), the light coming from upstream optics (upper left corner) is a small part of the light collected by the two principal mirrors and sent to the imaging instruments. This unpolarized light from the upstream optics is equally divided by a PBS (Polarized Beam Splitter) and each half is sent to a Koester Prism. Since each Koester prism/Photomultiplier tube setup is similar, only one is described here.

The Koester prism, effectively a folded version of a Michelson interferometer using a shearing dielectric film ⁽⁸⁾, is shown in greater detail in Figures 3.3b) and 3.3c) and works as follows. In Figure 3.3b), a plane wave front *c-b-a* enters the prism and, after an internal reflection, encounters the dielectric film. At the dielectric film, half the wave is reflected and advanced in phase by $\pi/2$, and half is transmitted. For example, half the power in point *c* maps to point *c''* when it is reflected and advanced in phase by $\pi/2$; the other half is transmitted and maps to point *c'*. All other points on the wave front from *c* to *a* behave similarly. The emerging wavefronts are thus phase shifted by $\pi/2$ with respect to each other and on each side this will cause an interference pattern which will be picked up by the photomultiplier.

However, when a wave front having a small tilt of ϵ encounters the Koester prism, similar geometric ray-tracing indicates that the spacing between the emerging wavefronts will vary by a factor 2ϵ . The 2ϵ factor will cause a sharply non-linear modulation of the interference pattern described above. It can be shown that the non-linear modulation, *m*, is proportional to the following quantity:

$$m \propto \frac{1}{\epsilon} \left(1 - \cos \frac{4\pi\epsilon}{\lambda} \right) \quad (3.1)$$

Equation (3.1) is plotted in Figure 3.4. It can be seen that any tilt of the telescope causes a sharp change in the modulation function away from zero. The output of this function is used to drive the servos. When the tilt error is zero, the servos receive no input; when the tilt is non-zero, the servos quickly receive a large driving voltage which is required to correct the telescope pointing ⁽⁷⁾.

Despite minor implementation problems, such as polarization-induced and chromatic aberration in the FGS optics, and despite the well-publicized spherical aberration which ultimately reduced the overall measurement sensitivity of the FGSs, this system met all required alignment specifications.

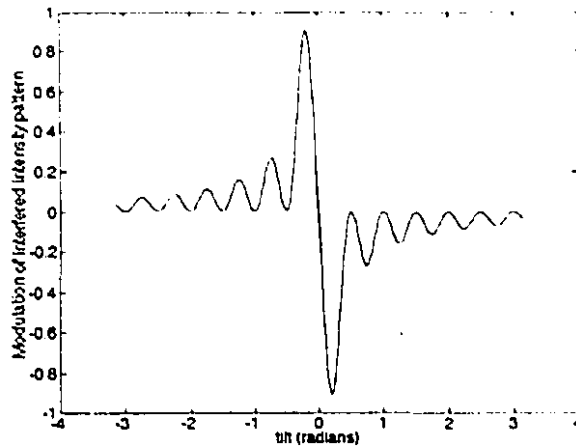


Figure 3.4: Ideal transfer function of Hubble Space Telescope Fine Guidance Sensor.

3.5 Image jitter compensation: ground-based astronomical telescopes

Image jitter is caused by vibration of the optics or by disturbance of the medium through which the light propagates. Jitter causes parts of the image in the image plane to move rapidly in a non-uniform manner, deteriorating the image quality. While it is unlikely that air turbulence along a 20 mm beam path in a backplane would cause noticeable jitter, image jitter could still be a problem in optical backplanes if cooling fans and other sources of mechanical movement vibrate the receiver or transmitter devices. Consequently, it is necessary to study existing jitter-compensation systems to determine the issues involved.

According to astronomical terminology ⁽⁹⁾, 'active optics' are used to compensate permanent or slowly time-varying aberrations and jitter in the image brought about by mirror imperfections, slow-changing thermal fluxes, and so on. 'Adaptive optics', on the other hand, deal with quickly time-varying jitter due to atmospheric disturbances. While telescopes implementing adaptive optics to compensate for atmospheric fluctuations have been in use for many years, they were used mainly by the military and as such were kept secret. Only recently has the theory behind their operation been disclosed ⁽⁹⁻¹²⁾.

It has been shown that the OTF (Optical Transfer Function) of the atmosphere varies widely and that these variations are correlated only over small viewing angles of a telescope⁽¹⁰⁾. The size of the viewing angle over which the OTF, and as such the phase of the incoming wave front, does not change significantly is defined as θ_{ip} , the isoplanatic angle. θ_{ip} can be approximated as:

$$\theta_{ip} = \frac{r_o}{3} \left(\frac{1}{h_o} - \frac{1}{h} \right) \quad (3.2)$$

where it is assumed the atmospheric distortion is confined to a layer of thickness h_o and of height h above the ground; as well, r_o is termed the Fried coherence diameter and is a function of the observation wavelength, the fluctuations in the index of refraction and the optical path length from the source to the aperture entrance plane. For $\lambda = 500$ nm and assuming typical astronomical viewing conditions, $r_o \approx 0.2$ m.

The impact of r_o is as follows. The angular resolution of a telescope of aperture D in an ideal environment is:

$$\theta_r = \frac{1.22\lambda}{D} \quad (3.3a)$$

However, in a real terrestrial environment the phase front is constant only over a subaperture of diameter r_o , and as such the angular resolution of the subimage coming from the subaperture of constant wavefront is limited to:

$$\theta_r' = \frac{1.22\lambda}{r_o} \quad (3.3b)$$

Furthermore, since the phase front varies randomly from subaperture to subaperture, the subimages are shifted relative to each other in the image plane, causing unacceptable deterioration in the image quality.

In an adaptive telescope, a deformable mirror in the optical train is divided into cells of diameter smaller than r_o , and these cells are moved in real time to compensate for the phase front variations due to atmospheric turbulence. A typical system is shown in Figure 3.5. Part of the incoming light is tapped off at the dichroic filter and the orientation of the phase front of each subaperture is monitored. The controller then determines both the coarse alignment which is performed with the tip-tilt mirror as well as the fine alignment which is performed by moving the cells in the deformable mirror.

If the observed star is not bright enough, a reference star within the isoplanatic angle is used for the alignment information, and if no reference star is found an artificial illumination is created by focusing a high power laser beam in the stratosphere such that the Rayleigh scattering forms a bright spot within the isoplanatic angle.

Such operational systems have produced near diffraction limited imaging with a Strehl ratio of approximately 0.67 and an angular resolution of ~ 0.07 arcsec at an observation wavelength of 500 nm⁽¹⁰⁾. However, an advanced operational system such as the US military's Short Wavelength Adaptive Technique (SWAT) system at the Firepond facility in Massachusetts demands an enormous computing bandwidth of around several hundred billion operations per second and requires about 250 piezo actuators⁽⁹⁾. For expensive systems with many actuators, piezos and similar compounds are often chosen as the actuators since their reliability is judged to outweighs their undesirable properties such as hysteresis and creep^(13,14). Piezos and similar compounds are further discussed in section 3.6.

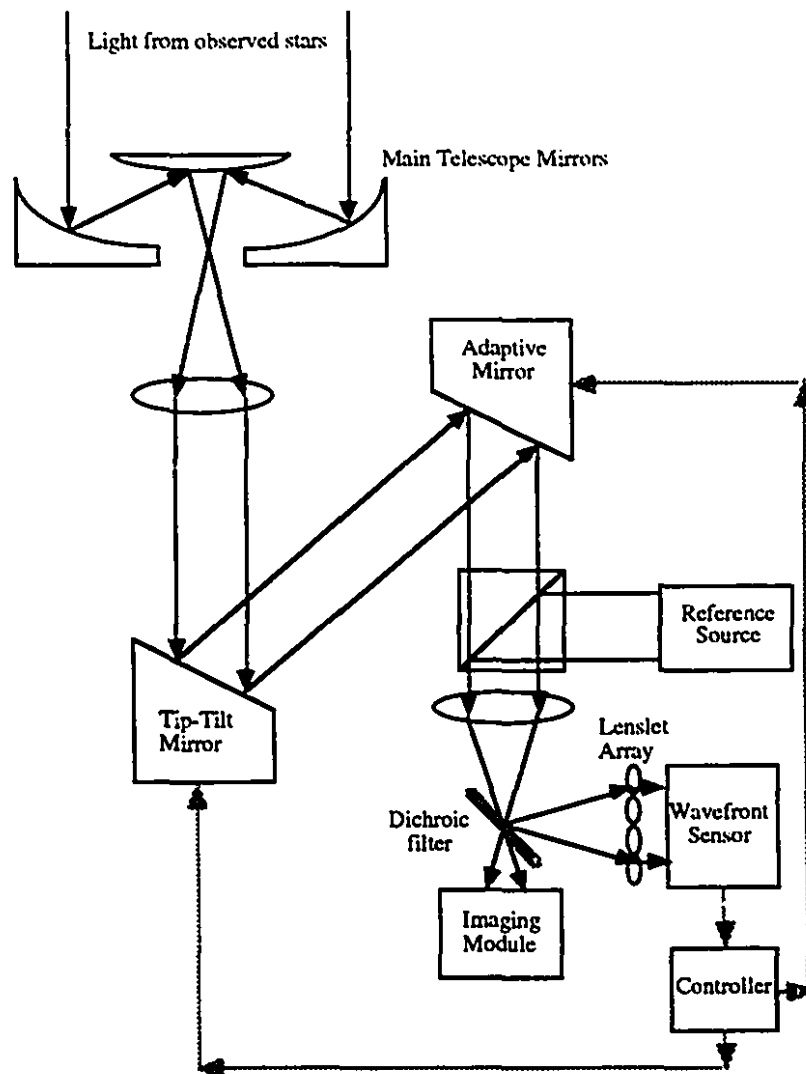


Figure 3.5: Simplified schematic of an adaptive telescope compensating for errors in wave front phase.

3.6 Issues in active alignment

Although the active alignment systems described above compensate for different types of misalignment errors, they all represent different compromises between three important issues in active alignment: reliability, accuracy, and cost. This section further explains how these issues will affect active alignment considerations for a free-space optical backplane.

3.6.1 Reliability

If a backplane fails, the performance of the entire computing system will suffer. The reliability of the backplane, and as such the reliability of any active alignment on a backplane, is critical.

One way to improve the reliability of an active alignment system is to eliminate as many moving parts as possible. The use of solid-state optics in alignment experiments has been tried, with moderate success. For example, in one experiment⁽¹⁵⁾, a large liquid crystal spatial light modulator (SLM) was built. By varying the voltage applied to various positions of the SLM, a graded index profile could be given to the SLM – in effect transforming the SLM into a lens. By changing the voltage applied to the SLM, the focal length of the lens could be changed. This theoretically allowed for correction of Δz_e misalignment errors (i.e. defocus) without mechanically moving a component. However, the best result that could be attained using this technique was a change in the lens' focal length from $f = \infty$ to $f = 1.32$ m; these numbers are clearly too large for backplane dimensions since PCB spacing was shown in Chapter 1 of this thesis to be on the order of 20-30 mm. Similar solid-state alignment experiments with similar results have been tried to correct for defocus in CD players as well ⁽¹⁶⁾.

Other methods for reducing the number of moving parts in an active alignment system include the use of piezoelectric (PZT) or electrostrictive (ESA) actuators. These actuators have crystal structures which exhibit strain when a voltage is applied to them. PZTs and ESAs have key advantages: 1) the actuators themselves have no moving parts since all strain is a result of crystal relaxation and contraction, and 2) small volumes can move great mechanical loads (for example, a 6 mm x 15 mm ESA stack can exert a force of 750 N ⁽¹⁷⁾). There are, however, many drawbacks: 1) they require substantial drive voltages (the 750 N force above requires an applied voltage of 150V, for example) 2) the relation between applied voltage and strain is extremely complex. Non-linearities such as creep, hysteresis, and aging complicate the control algorithms for systems implementing these

actuators^(12,18), 3) their travel is very small: a maximum strain of 0.13%, a typical value for a PZT⁽¹³⁾, yields a maximum travel of 19.5 μm for a 15 mm actuator stack, and 4) their performance is strongly affected by temperature: a change of $\Delta T = 50^\circ\text{C}$ can bring about a 50% reduction in strain for certain PZTs⁽¹⁷⁾. A major difference between the ESAs and PZTs is that ESAs exhibit smaller non-linearities but require greater drive power and can only be moved at slower speeds than PZTs.

The analysis and examples in this chapter indicate that highly reliable components and actuators featuring little or no moving parts do exist and are in use in specialized and expensive systems featuring active alignment. For example, PZTs are used in the SWAT telescope described above or in certain specialized laser cavities⁽¹⁹⁾. Furthermore, adaptive alignment systems featuring over 1000 PZT actuators have been built, which further demonstrates that reliable systems employing large numbers of actuators can be built⁽²⁰⁾. However, the major drawbacks such as limited travel, temperature dependence, and difficult control have prevented their widespread use in mass-produced optical systems. More research on these highly reliable but complex devices is necessary before they can be put into backplanes.

3.6.2 Accuracy

Chapter 2 indicated that lateral resolution on the order of several μm and angular resolution on the order of several arc minutes will be required in order to maintain alignment in high-performance free-space optical interconnects. PZTs or ESAs were shown in subsection 3.6.1 to be a solution. There are, however, other high accuracy solutions for applications not requiring the nanometer resolution of PZTs and ESAs. Servo motors are used in many high accuracy applications such as the above-mentioned Hubble Space Telescope (HST) and other high accuracy space-based and ground-based beam steering systems⁽²¹⁾. Furthermore, extremely high resolution can be achieved with standard off-the-shelf gear and encoder combinations attached to servo motors or stepper motors⁽²²⁾. The demonstrator system described in chapters 4 - 6 uses such a stepper-motor gear combination to achieve $<1^\circ$ accuracy.

Another important factor determining the accuracy of an active alignment system is its control bandwidth. Control bandwidth is a system parameter indicating how fast a system can respond to disturbances⁽²³⁾. Control bandwidth is a function of the speed of actuators, the power train, the error detection, and the controller. This will be an important factor for optical backplanes if cooling systems and other mechanical vibrations contribute substantial vibrations: for example, a control bandwidth necessary to compensate for a backplane fan's

60 Hz vibration could be necessary. Further research is needed to determine the control bandwidth necessary for active alignment of a free-space optical backplane.

Finally, there have also been attempts to build high accuracy active alignment systems implementing adaptive algorithms on neural networks in order to improve speed and accuracy in all conditions. Such systems, however, have barely progressed beyond the proof-of-concept stage⁽²⁴⁾.

3.6.3 Cost

A fully equipped state-of-the-art 21 slot VME electronic backplane system complete with chassis, fans and a 600 W power supply cost around US\$4000⁽²⁵⁾ in 1993, and prices are falling. While the higher performance of an optical backplane could arguably command higher cost premiums, backplanes are nonetheless in a very cost-sensitive market. As such, elaborate and expensive active alignment systems which are acceptable for military systems or the HST are unacceptable for a backplane which will be sold in the notoriously cut-throat "boards and busses" market.

Compact disks are an example of a successful high accuracy low-cost mass-market system implementing active alignment: only a laser diode, quadrant detector, actuator coils, and simple optics and electronics are required. Consequently, many ideas from CD systems such as the use of quadrant detectors warrant further study.

3.7 Conclusion

The review indicates that active alignment is still a new field. Designs of many new systems featuring moving optics such as autofocus cameras or jitter correcting binoculars are still kept secret for commercial or military reasons. As well, the terminology is not yet fixed. For example, astronomers have designed and built many various types of active alignment systems and have subdivided the taxonomy ⁽⁹⁾: they term low frequency alignment (<1 Hz) 'active optics', and high frequency alignment (~1kHz) 'adaptive optics'.

Nonetheless, a review of existing active alignment schemes indicates the trends. In many cases, optomechanical issues are fundamental to the whole active alignment system as well as to the whole optical system. Furthermore, computing power is seen to occupy an increasingly important role as systems become more complex.

Many concepts brought up in this review, such as the use of quadrant detectors to determine misalignment error, the use of reference beams in jitter-compensating telescopes,

and different methods of achieving high accuracy movement, are applicable to a harsh backplane environment. In order to determine how many concepts and ideas can be borrowed from other active alignment systems and incorporated into an active alignment system for a backplane, an x-y active alignment demonstrator was designed, simulated, built and tested. This demonstrator is the subject of the next three chapters of this thesis.

3.8 References

- [1] L. Pedulla, "Spinning sound in a different direction", *Optics & Photonics News*, 5, 6 (1994).
- [2] W. H. Lee, "Optical technology for compact disk pickups", *Lasers & Optronics*, 6, (1987).
- [3] E. Hecht, Optics, Addison Wesley Publishing Company, 1990.
- [4] N. Tamaru, "Mechanical Characteristics of air bearings for supporting a flexible optical disk", *Appl. Opt.* 32, 7243 (1993).
- [5] W. H. Lee, "Holographic optical head for compact disk applications", *Optical Engineering*, 28, 650, (1989).
- [6] Y. Tanaka, M. Sunohara, J. Murata, T. Nakamura, and H. Aikoh, "Molded-glass optical element for focusing servos", *Appl. Opt.*, 33, 108 (1994).
- [7] C. Ftacilas, R. Basedow, A. Nonnenmacher, F. Weindling, D. Story, and E. Nelan, "Hubble Space Telescope fine-guidance sensor transfer function and its impact in telescope alignment and guidance", *Appl. Opt.*, 32, 1696 (1993).
- [8] J. R. Meyer-Arendt, Introduction to Classical and modern optics, Prentice Hall Canada Inc, Toronto, (1984).
- [9] N. Hubin and L. Noethe, "Active optics, adaptive optics and laser guide stars", *Science*, 262, 1390 (1993).
- [10] C. S. Gardner, B.M Welsh, and L. A. Thompson, "Design and performance analysis of adaptive optical telescopes using laser guide stars", *Proc. IEEE*, 78, 1721 (1990).
- [11] N. C. Mehta and C. W. Allen, "Segmented mirror alignment with far-field optimization in the presence of atmospheric turbulence", *Appl. Opt.* 32, 2664 (1993).
- [12] E. H. Anderson, D. M. Moore, J. L. Fanson, M. A. Ealey, "Development of an active truss for control of precision structures", *Optical Engineering*, 29, 1333 (1990).
- [13] S. Vorndran and D. Hardwick, "Micropositioning with piezoelectric actuators", *Motion control*, 24, May 1993.

- [14] C. G. O'Neill and C. H. O'Neill, "Ferroelectric actuators in the electromechanical interface", *Optical Engineering*, **29**, 1383 (1990).
- [15] G. A. Melnik, G. C. Gilbreath, T. N. Tsakiris, R. P. Jurgilewicz, D. M. O'Mara, T. N. Horsky, and C. Warde, "Operating modes of a charged-transfer-plate liquid-crystal phase modulator", *Appl. Opt.*, **31**, 3892 (1992).
- [16] K. Osato and G. S. Kino, "Electro-optic focusing system for a high-density optical disk", *Opt. Lett.*, **18**, 1244, (1993).
- [17] J. Galvagni, "Electrostrictive actuators and their use in optical applications", *Optical Engineering*, **29**, 1389 (1990).
- [18] J. L. Fanson, E. H. Anderson, and D. Rapp, "Active structures for use in precision control of large optical systems", *Optical Engineering*, **29**, 1320 (1990).
- [19] D. V. Plant, Measurements of the pressure broadening coefficient of the J=31-> J=32 rotational transition of methyl fluoride and far infrared studies of the phase transition in β -quinol methanol and methanol-D4 clathrates, Ph.D. Thesis, Brown University (1989).
- [20] J. W. Hardy, "Adaptive optics", *Scientific American*, **271**, 60, June (1994).
- [21] L. Germann and J. Braccio, "Fine-steering mirror technology supports 10 nanoradian systems", *Optical Engineering*, **29**, 1351 (1990).
- [22] Micro Mo inc. "Miniature drive systems", catalog (1993).
- [23] Åström and Wittenmark, Computer controlled systems: Theory and Design, Prentice Hall Canada Inc, Toronto, (1990).
- [24] A. J. Decker, "Self-aligning optical measurement systems", *Appl. Opt.*, **31**, 4339 (1992).
- [25] "EDN-New Products", *EDN*, 27 May , 182 (1993).

Chapter 4

Theory of x-y active alignment using Risley Beam Steerers

4.1 Introduction

To gain a first-hand appreciation for the practical challenges and issues which the active alignment of a free-space optical interconnect introduces, an active alignment demonstrator was designed, simulated, built, and tested. This chapter outlines the theory and design required for the demonstrator.

The simplified layout of the demonstrator is shown in Figure 4.1. The system worked as follows: the misalignment error between the actual and desired location of a spot on a quadrant detector was used to compute the angular displacement required for two Risley Beam Steerers (RBSs) to centre the spot in the x-y plane.

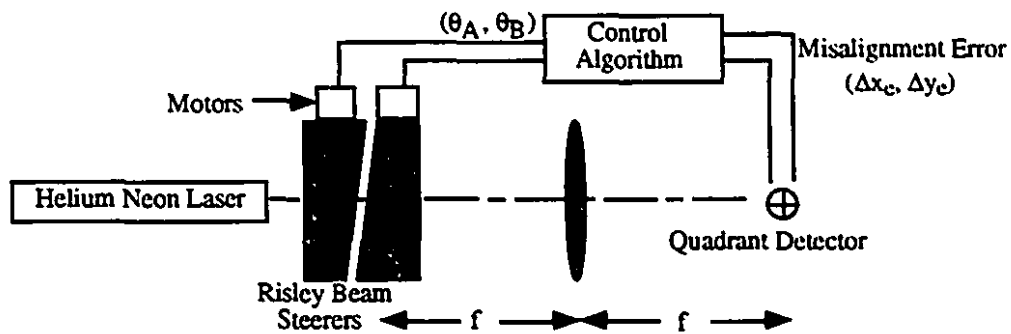


Figure 4.1: Simplified optical and mechanical layout of the demonstrator.

A discussion of how the misalignment error signal is determined is given in section 4.2. It is shown that a spot impinging on a quadrant detector (QD) creates four independent photocurrents each of which creates a voltage when driven across a resistor. The relationship between these four voltages and the spot misalignment error $(\Delta x_e, \Delta y_e)$, where $(\Delta x_e, \Delta y_e) = (0,0)$ represents a centered spot, is determined. It is shown that, within system limits, a larger spot size yields a greater range over which the error $(\Delta x_e, \Delta y_e)$ is linearly proportional to voltage differences. In section 4.3, a justification for the use of RBSs and the optical theory explaining the action of the RBSs are given. An algorithm which uses RBSs to centre a misaligned spot is then derived. Simulations are also presented in order to better illustrate the centering action of the RBSs.

4.2 Determination of misalignment error

In this section it is shown that a spot impinging on the quadrant detector (QD) creates four independent photocurrents which in turn create four independent voltages when driven across resistors. Performing arithmetic on these four voltages yields voltage differences which give information about the misalignment error. However, it is shown that the spot must be of an optimal size for the voltage differences to be linearly proportional to the misalignment error over a given range. The measurement sensitivity, a scaling constant k relating the actual misalignment error of the optimal spot to the voltage difference, is also introduced.

4.2.1 Geometric and opto-electronic features of a quadrant detector

A quadrant detector (QD) is an optoelectronic device composed of four independent photosensitive areas laid out in a quadrant; Figure 4.2 shows a front view of a typical QD. The origin is at the centre of the intersection of the gaps. Figure 4.3a) shows a centered spot and Figure 4.3b) shows a spot misaligned by $(\Delta x_e, \Delta y_e)$.

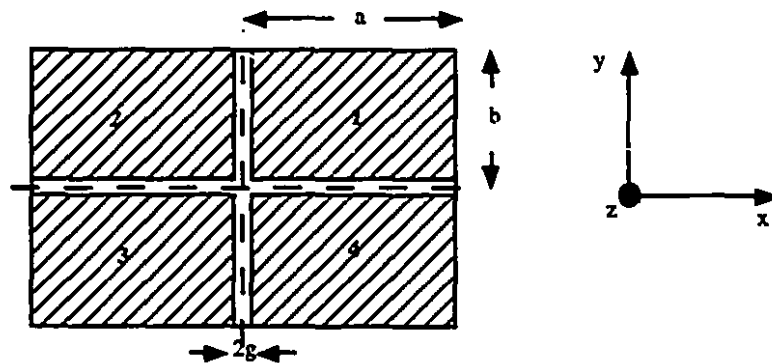


Figure 4.2 Quadrant Detector Geometry.

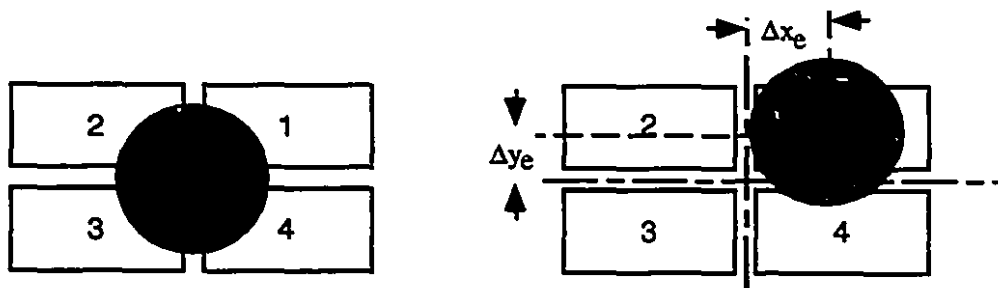


Figure 4.3 a) centered spot and b) spot misaligned by $(\Delta x_e, \Delta y_e)$.

Each photosensitive area can be modeled as a diode which, when reverse biased, produces a photocurrent, i_p , proportional to the integral of the irradiance on the quadrant:

$$i_p = \left(\int \text{irradiance on photosensitive area} \times dA \right) \times S \quad (4.1)$$

$$= P_{q_j} \times S$$

where P_{q_j} is the total light power incident on quadrant j and S is the optoelectronic sensitivity, expressed in units of A/W.

When i_p flows through a resistor, R , a voltage V is produced according to Ohm's law. Figure 4.4 indicates the layout of the circuit containing the resistor, bias voltage, and photosensitive area for one quadrant.

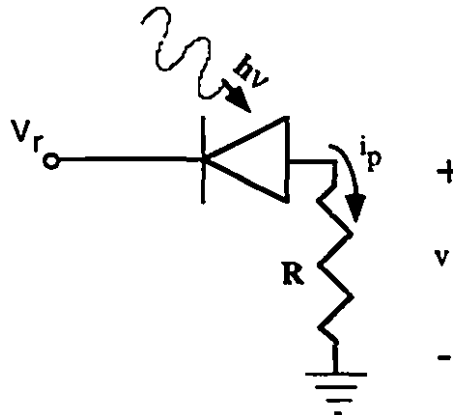


Figure 4.4: Bias circuit for one photosensitive area of the QD.

Consequently, a spot with a Gaussian irradiance pattern impinging on a QD will create four voltages: V_1 , V_2 , V_3 , and V_4 . It is shown in the next subsection that the misalignment error (Δx_e , Δy_e) of a spot of optimal size can then be approximated by the following relations over a small range of misalignments:

$$\Delta x_e = k[V_1 + V_4 - (V_2 + V_3)] \quad \mu\text{m} \quad (4.2a)$$

$$\Delta y_e = k[V_1 + V_2 - (V_3 + V_4)] \quad \mu\text{m} \quad (4.2b)$$

where k , the measurement sensitivity having units of $\mu\text{m}/V$, is a scaling constant relating the differential voltages to the actual spot misalignment error.

Sections 4.2.2 to 4.2.5 solve the integral in Equation (4.1) for an arbitrary spot displacement and size in order to determine the optimal spot size.

4.2.2 Definitions and assumptions

Let

- 1) $P_{q1}, P_{q2}, P_{q3}, P_{q4}$ be the total optical power incident on quadrants 1, 2, 3 and 4 respectively.
- 2) the quadrant detector be composed of four identical and independent photosensitive areas separated by a gap of width $2g$. The detector's dimensions, and the four quadrants numbered from 1 to 4, are shown in Figure 4.2.
- 3) ΔV_x and ΔV_y be defined as follows:

$$\Delta V_x = (V_1 + V_4) - (V_2 + V_3) \quad (4.3a)$$

$$\Delta V_y = (V_1 + V_2) - (V_3 + V_4) \quad (4.3b)$$

- 4) E be the magnitude of the misalignment error, which is the distance from the centre of the spot to the origin of the QD:

$$E = \sqrt{(\Delta x_e)^2 + (\Delta y_e)^2} \quad (4.4)$$

- 5) the spot have a Gaussian irradiance distribution, $I(r)$, with peak irradiance I_0 .

$$I(r) = I_0 e^{-2r^2/w^2} \quad (4.5)$$

4.2.3 Total light power for centered spot

When the spot is centered, $(\Delta x_e, \Delta y_e) = (0,0)$ and $P_{q1}, P_{q2}, P_{q3}, P_{q4} = P_q$.

For a, b , and g defined in Figure 4.2 and for a Gaussian irradiance, P_q is calculated as follows:

$$\begin{aligned} P_q &= I_0 \iint_A e^{-2(x^2+y^2)/w^2} dA \\ &= I_0 \int_{-g}^g e^{-2y^2/w^2} dy \int_{-g}^g e^{-2x^2/w^2} dx \end{aligned} \quad (4.6)$$

Now let

$$t = \sqrt{2} / y \quad (4.7)$$

$$u = \sqrt{2} / x \quad (4.8)$$

$$\alpha = w / \sqrt{2} \quad (4.9)$$

Substituting (4.7),(4.8) and (4.9) into (4.6) yields

$$\begin{aligned} P_q &= \alpha^2 I_o \int_{g/\alpha}^{b/\alpha} e^{-t^2} dt \int_{g/\alpha}^{a/\alpha} e^{-u^2} du \\ &= \frac{\alpha^2 I_o \pi}{4} [\text{erf}(b/\alpha) - \text{erf}(g/\alpha)] [\text{erf}(a/\alpha) - \text{erf}(g/\alpha)] \end{aligned} \quad (4.10)$$

where

$$\text{erf}(z) = \frac{2}{\sqrt{\pi}} \int_0^z e^{-t^2} dt \quad (4.11)$$

4.2.4 Total light power for misaligned spot

In this subsection, the total light power in each quadrant is calculated when the misalignment error of the spot centre is $(\Delta x_e, \Delta y_e)$. In this case, the irradiance $I(x,y)$ is:

$$I(x,y) = I_o e^{-2((x-\Delta x_e)^2 + (y-\Delta y_e)^2)/w^2} \quad (4.12)$$

And the total light power on quadrant 1, P_{q1} , is:

$$\begin{aligned} P_{q1} &= I_o \iint_A e^{-2((x-\Delta x_e)^2 + (y-\Delta y_e)^2)/w^2} dA \\ &= I_o \int_g^a e^{-2(x-\Delta x_e)^2/w^2} dx \int_g^b e^{-2(y-\Delta y_e)^2/w^2} dy \end{aligned} \quad (4.13)$$

Transformations similar to those in the section 4.2.3 lead to:

$$P_{q1} = I_o \alpha^2 \frac{\pi}{4} \left\{ \text{erf} \left[\frac{(a-\Delta x_e)}{\alpha} \right] - \text{erf} \left[\frac{(g-\Delta x_e)}{\alpha} \right] \right\} \left\{ \text{erf} \left[\frac{(b-\Delta y_e)}{\alpha} \right] - \text{erf} \left[\frac{(g-\Delta y_e)}{\alpha} \right] \right\} \quad (4.14)$$

Now, to determine the light power on quadrant 2, P_{q2} , the irradiance described in Equation (4.12) is integrated over area # 2 of the QD described in Figure 4.2:

$$P_{q_2} = I_0 \int_g^b e^{-2(y-\Delta y_e)^2/w^2} dy \int_{-a}^{-g} e^{-2(x-\Delta x_e)^2/w^2} dx \quad (4.15)$$

Similar operations are performed for P_{q3} and P_{q4} ; the resulting power on quadrants 2,3, and 4 is thus:

$$P_{q_2} = I_0 \alpha^2 \frac{\pi}{4} \left\{ \operatorname{erf} \left[\frac{(-g-\Delta x_e)}{\alpha} \right] - \operatorname{erf} \left[\frac{(-a-\Delta x_e)}{\alpha} \right] \right\} \left\{ \operatorname{erf} \left[\frac{(b-\Delta y_e)}{\alpha} \right] - \operatorname{erf} \left[\frac{(g-\Delta y_e)}{\alpha} \right] \right\} \quad (4.16a)$$

$$P_{q_3} = I_0 \alpha^2 \frac{\pi}{4} \left\{ \operatorname{erf} \left[\frac{(-g-\Delta x_e)}{\alpha} \right] - \operatorname{erf} \left[\frac{(-a-\Delta x_e)}{\alpha} \right] \right\} \left\{ \operatorname{erf} \left[\frac{(-g-\Delta y_e)}{\alpha} \right] - \operatorname{erf} \left[\frac{(-b-\Delta y_e)}{\alpha} \right] \right\} \quad (4.16b)$$

$$P_{q_4} = I_0 \alpha^2 \frac{\pi}{4} \left\{ \operatorname{erf} \left[\frac{(a-\Delta x_e)}{\alpha} \right] - \operatorname{erf} \left[\frac{(g-\Delta x_e)}{\alpha} \right] \right\} \left\{ \operatorname{erf} \left[\frac{(-g-\Delta y_e)}{\alpha} \right] - \operatorname{erf} \left[\frac{(-b-\Delta y_e)}{\alpha} \right] \right\} \quad (4.16c)$$

4.2.5 Application of equations describing total light power

In this subsection, the equations of total light power derived in the previous subsections are used to determine the optimal spot size which will yield a linear relationship between voltages and misalignment error for a range of misalignment errors on a given QD geometry.

Combining Eq (4.1) with (4.14), (4.16a), (4.16b), and (4.16c) yields the photocurrent produced by the part of the spot on quadrants 1, 2, 3 and 4, respectively. An optoelectronic sensitivity of $S = 0.41 \text{ A/W}$ is assumed since this is the optoelectronic sensitivity of the photosensitive devices for the QD used in the demonstrator (at $\lambda = 632.8 \text{ nm}$)⁽¹⁾. The analysis given in this section is valid for any optoelectronic sensitivity, however. When the four photocurrents are each passed through a resistor, four voltages V_1 , V_2 , V_3 and V_4 are produced. At this point, it is useful to plot ΔV_x vs the distance from the spot centre to the QD centre (E) The plot is given in Figure 4.5.

In Figure 4.5 can be seen the plot of ΔV_x vs E as the centre of the spot moves along the mathematical line $y = x$ between points P_3 and P_1 shown in Figure 4.6 (E is set negative for spots centered in quadrant 3). In this case, $a \gg g$ and $b \gg g$; as well, w and E are both normalized with respect to g . The resistance and total light power in the spot are fixed arbitrary values.

Figure 4.5 indicates that for $w < g$, the curve ΔV_x vs E is highly non-linear. On the other hand, for $w > g$, the curve is approximately linear. Furthermore, as w increases, ΔV_x varies linearly with displacement over a greater displacement range, but the lower the slope $d\Delta V_x/dE$ becomes. Simple algebra indicates that for $w > g$ the slope $d\Delta V_x/dE$ is the constant k in Eq. (4.2).

The constant k is the measurement sensitivity of the setup: a small k yields a small voltage change (ΔV) for a given displacement. Conversely, a large k yields a large ΔV for the same given displacement. A large measurement sensitivity is desirable since it yields more precise measurements for a given signal to noise ratio and simplifies the electronics.

For large spots, i.e. for $(w/g) > 1$, the most accurate information is obtained when the spot centre is closest to the gap, which indicates that this method theoretically is most accurate for detecting small misalignment errors about the origin - an interesting fact.

To summarize, Figure 4.5 indicates that an optimal spot size can be chosen such that Eq. (4.2) holds for a certain linear range. The determination of this optimal spot size for the actual demonstrator is given in the next chapter.

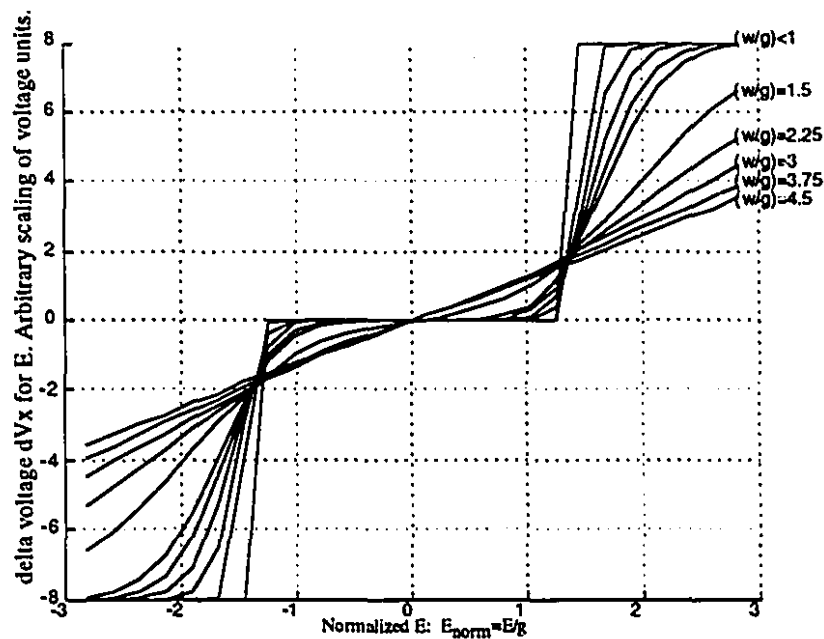


Figure 4.5: Ideal dV_x for normalized spot displacement along $y = x$ line (rectangular QD).

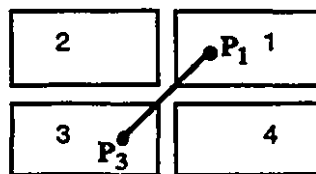


Figure 4.6: Trajectory of centre of spot used to obtain graph in Figure 4.5.

4.3 Model of Movement of Risley Beam Steerers

In this section, the use of RBSs for this active alignment demonstrator is justified, their non-linear motion is explained, and an algorithm transforming a desired Cartesian displacement into an equivalent movement performed by two RBSs in series is derived.

4.3.1 Justification for using Risley Beam Steerers in active alignment

Three reasons for choosing Risley Beam Steerers (RBSs) as the optical components to move in an active alignment experiment are:

1) They have already been used for x-y alignment in free space-optical systems⁽²⁾ and have proven to be a simple and cheap way of aligning free-space interconnects.

2) Optical steering components requiring rotational, as opposed to lateral, displacement can more easily fit into a barrel or other integrated optomechanical setup. In addition, angular motion is easier to control than rectilinear motion when compensating for vibrational effects⁽³⁾.

3) As will be shown below, the deviation of a spot by RBSs, while inherently non-linear, can be modeled algorithmically with high accuracy.

4.3.2 Definitions and assumptions

Let

- 1) An RBS be a nearly cylindrical optical component with a wedge in it, and whose purpose is to steer beams of light by imparting an angular displacement to them, as shown in Figures 4.7 and 4.8.
- 2) The two RBSs in the system be named RBS A and RBS B.
- 3) β_A and β_B be the wedge angle of RBS A and RBS B respectively.
- 4) θ_A and θ_B be respectively the angular rotation of RBS A and RBS B about the z-axis, as shown in Figure 4.8.
- 5) (x_1, y_1) be the Cartesian representation of an arbitrary displacement imparted to a spot by the RBSs, and let d_1 be the magnitude of the displacement (x_1, y_1) :

$$d_1 = \sqrt{x_1^2 + y_1^2} \quad (4.17)$$

- 6) θ_1 be a modified form of $\arctan(y_1/x_1)$, such that $0 \leq \theta_1 < 2\pi$.
- 7) (x_u, y_u) be the position of the spot on the QD had it been unchanged by the RBS pair.

4.3.3 Effect of two RBSs in series on the trajectory of a beam

From first order theory ⁽⁴⁾, the angular deviation, δ , imparted by a wedge on a beam is:

$$\delta = (n-1)\beta \quad (4.18)$$

where n is the index of refraction of the RBS. As such, at the focal plane of a lens with focal length f , the lateral displacement, r , to the spot imparted by the RBS is:

$$r_A = f \tan \delta_A = f \tan((n-1)\beta_A) \quad (4.19a)$$

$$r_B = f \tan \delta_B = f \tan((n-1)\beta_B) \quad (4.19b)$$

The graphical representation of equations (4.18) and (4.19) is given in Figure 4.7.

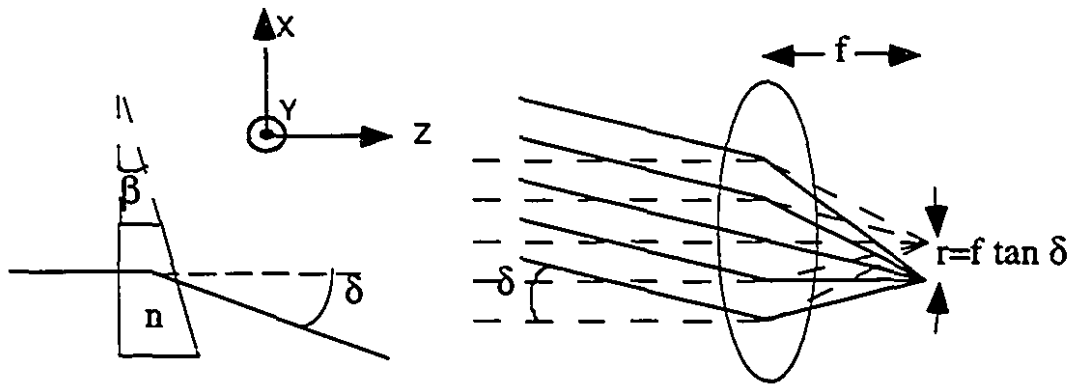


Figure 4.7: Effect of wedge on beam propagation and resulting displacement due to a lens. An RBS is effectively an element with a wedge in it.

Rotating the wedge about the z axis will cause the spot in the focal plane to move along the circumference of a circle of radius r in the x - y plane at the lens' focal plane.

If RBS A and B are laid out in series along the beam path, the angular displacements imparted by the two RBSs will add. When RBSs A and B are rotated about the z -axis, the spot will move on the periphery of a first circle of radius r_A whose centre is located on the periphery of a second circle of radius r_B . This is shown in Figure 4.8b). A more formal definition is given below. The maximum deviation of the beam with respect to the optical axis will thus be equal to $r_A + r_B$. This maximum deviation will arise when the angular rotation of the wedges is identical. A more formal analysis is carried out in the following subsections, and in appendix A a full optical calculation of the effect of two RBSs shows

that the "circle on circle" approximation is valid to well within one percent for the physical values used in the demonstrator.

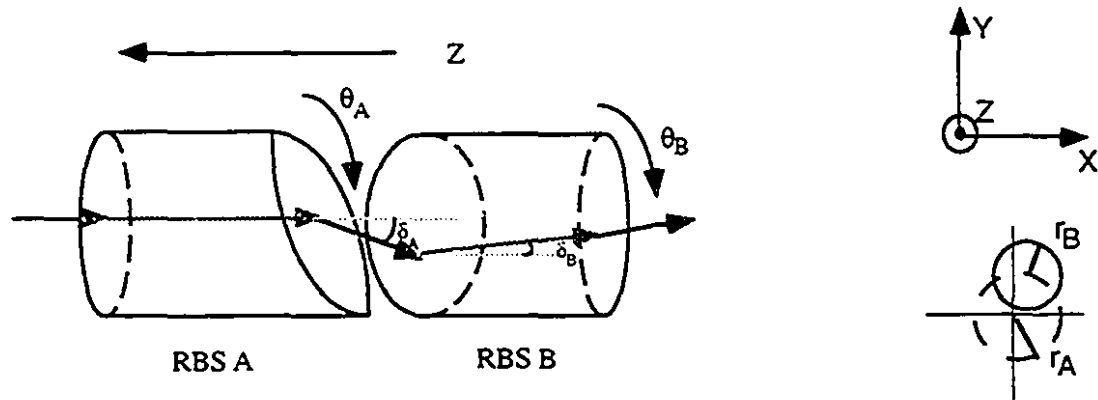


Figure 4.8 a) Effect on beam of two RBSs in series . Z-axis is coaxial with RBSs.
b) locus of spot movement on the focal plane, looking down the z-axis.

4.3.4 Transformation expressing lateral Cartesian displacement as an angular RBS displacement (CtoR transform)

In this subsection, a more formal description of the phenomenon described in the previous subsection and pictured in Figure 4.8b) is given. As well, a transformation is found which maps a Cartesian displacement (x_I, y_I) into a rotational displacement (θ_A, θ_B) of two RBSs, as outlined in Figure 4.9.

The angles θ_A and θ_B are illustrated in Figure 4.9. By definition, these angles are like conventional geometric angles: they are zero when in the "3 o'clock" position and increase in a counter-clockwise direction. At this point, before starting the geometric analysis, it is best to give a few examples: (i) the CtoR transform of the Cartesian displacement $(x_I, y_I) = (r_A + r_B, 0)$ yields the RBS angles $(\theta_A, \theta_B) = (0, 0)$; (ii) the CtoR transform of the Cartesian displacement $(x_I, y_I) = (0, r_A + r_B)$ yields the RBS angles $(\theta_A, \theta_B) = (\pi/2, \pi/2)$. A complete simulation of the RBS movement is given in subsection 4.3.9.

There are three distinct cases to be considered when studying the CtoR transform:

- 1) $d_I > r_A + r_B$ yields an impossible solution
- 2) $d_I < |r_A - r_B|$ yields an impossible solution
- 3) $|r_A - r_B| < d_I < r_A + r_B$ yields a solution

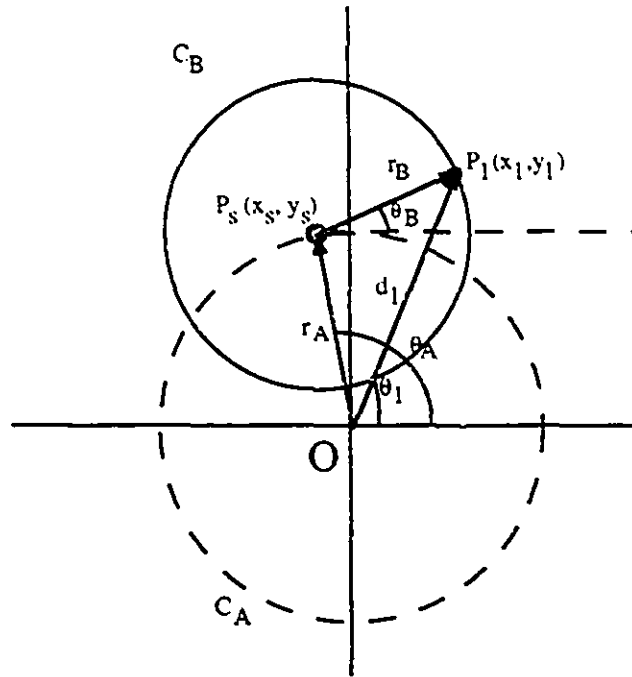


Figure 4.9: Desired Cartesian displacement (x_1, y_1) with corresponding angular rotation of RBSs (θ_A, θ_B) , along with other mathematical points and constructions used in derivation of CtoR transform.

From Figure 4.9, it can thus be seen that the displacement imparted by RBS A and RBS B in series is equal to the displacement between (i) the tip of a first vector of length r_B and rotated by θ_B , and (ii) the tail of a vector of length r_A and rotated by θ_A whose tip is at the tail of the first vector.

From the geometry defined in Figure 4.10, the following relationships are obtained from the cosine law:

$$r_B^2 = r_A^2 + d_1^2 - 2r_A d_1 \cos(\theta_a) \quad (4.20a)$$

$$r_A^2 = r_B^2 + d_1^2 - 2r_B d_1 \cos(\theta_b) \quad (4.20b)$$

Simplifying yields:

$$\cos \theta_a = \frac{r_B^2 - r_A^2 - d_1^2}{-2r_A d_1} \quad (4.21a)$$

$$\cos \theta_b = \frac{r_A^2 - r_B^2 - d_1^2}{-2r_B d_1} \quad (4.21b)$$

Simple geometry from Figure 4.10 yields the following relationships:

$$\theta_A = \theta_1 + \theta_a \quad (4.22a)$$

$$\theta_B = \theta_1 - \theta_b \quad (4.22b)$$

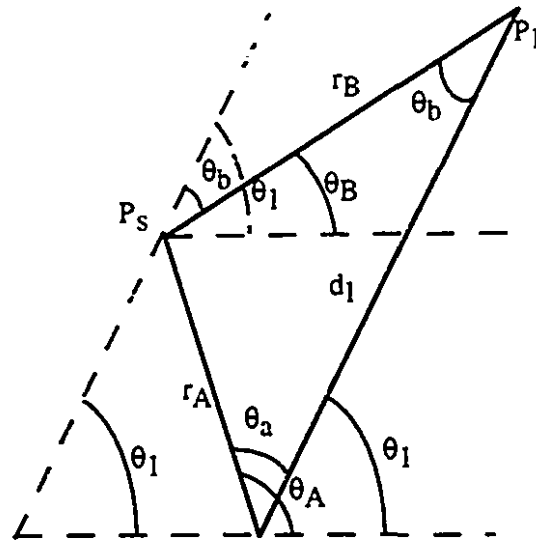


Figure 4.10: Geometry of RBS movement.

For there to be a real solution to equation (4.21a), the inequality $|\cos(\theta_a)| < 1$ must hold, which means that

$$\left| r_B^2 - r_A^2 - d_1^2 \right| < \left| -2r_A d_1 \right| \quad (4.23)$$

Solving (4.23) yields two conditions (an analogous result is obtained for θ_b):

$$1) d_1 < r_A + r_B \quad \text{and} \quad 2) d_1 > |r_A - r_B|$$

The first condition simply implies that the total misalignment distance, d_1 , must be less than the total radius of action of the RBSs. The second condition is more problematic and implies that there is a region, a 'blind area', to which the RBSs cannot centre a spot.

The blind area does not mean that the mismatched RBSs will never be able to centre a spot. Rather, the blind area means that the RBSs will never be able to impart a net displacement of zero μm to the spot. The corollary of this statement is: if the spot is perfectly centered before the insertion of the RBSs, the spot will never be centered after their insertion, regardless of their angular rotation. Only if the spot is more than $|r_A - r_B|$ away from the centre before the RBS insertion can it be centered after the RBS insertion.

4.3.5 Cartesian displacement of spot imparted by two RBSs with known angular rotation (RtoC Transform)

The RtoC transform is the inverse of the CtoR transform. The RtoC transform is simply the sum of two displacements expressed in polar coordinates.

$$\begin{aligned}x_1 &= r_A \cos \theta_A + r_B \cos \theta_B \\y_1 &= r_A \sin \theta_A + r_B \sin \theta_B\end{aligned}\quad (4.24)$$

4.3.6 Formal algorithm for calculating the angular displacement necessary for two RBSs to correct a lateral misalignment error detected by a quadrant detector

In this subsection a formal algorithm is developed for the centering of a spot which is misaligned by $(\Delta x_e, \Delta y_e)$. The 'circle on circle' model outlined above is used and it is assumed that the algorithm is working in the steady-state, i.e. the current value of (θ_A, θ_B) is known.

The following is an algorithm for determining the angular rotation of the two RBSs required to centre on the QD a spot which is currently misaligned by $(\Delta x_e, \Delta y_e)$:

- 1) Determine $(\Delta x_e, \Delta y_e)$
- 2) Determine (x_u, y_u) by the following calculation in which the RtoC transform is used:

$$\begin{aligned}x_u &= \Delta x_e - (r_A \cos \theta_A + r_B \cos \theta_B) \\y_u &= \Delta y_e - (r_A \sin \theta_A + r_B \sin \theta_B)\end{aligned}\quad (4.25)$$

3) Given the nature of the CtoR transform which models how two RBSs impart a displacement on a spot, perform the CtoR transform on $(-x_u, -y_u)$ in order to determine (θ_A, θ_B) which will centre the spot.

$$d_1 = \sqrt{x_u^2 + y_u^2}\quad (4.26)$$

$$\theta_1 = \arctan\left(\frac{y_u}{x_u}\right) \text{ where } 0 \leq \theta_1 < 2\pi.\quad (4.27)$$

and θ_a and θ_b are determined as per equation (4.21).

The new value of (θ_A, θ_B) is thus:

$$\theta_A = \theta_1 + \theta_a \quad (4.28a)$$

$$\theta_B = \theta_1 - \theta_b \quad (4.28b)$$

(θ_A, θ_B) is now the desired input pair of angles to be fed to the stepper motor system controlling the RBSs. Note that (θ_A, θ_B) obtained in Eq. (4.28) is valid for case 3) in subsection 4.3.4. For the cases in which more than one solution is possible (equal wedge angles), the algorithm chooses the solution consistent with the geometry of Figure 4.10.

4.3.7 Formal algorithm for determining initial (θ_A, θ_B) given arbitrary initial angular displacement of RBSs

The assumption at the start of subsection 4.3.6 states that the initial angular displacement of the RBSs must be known. However, in order to begin, there must be an initialization routine which determines the initial angular displacement of the RBSs. This initialization routine should be as simple as possible and minimize all alignment and pre-alignment. This initialization process is called hunting.

In order to facilitate the explanation that follows, a Matlab™ simulation of the hunting process is included at the end of this subsection.

The geometry from the above subsections indicates that for the particular case of $r_A = r_B = r$, there may be two solutions for (θ_A, θ_B) for a non-zero displacement imparted by the RBSs. This multiplicity of solutions is problematic; if the hunting algorithm is to be useful in all circumstances, it must accommodate this particular case. A solution to this problem is as follows. From the explanation of the algorithm in the preceding subsections, it can be seen that the maximum deviation imparted by the RBSs will occur when $\theta_A = \theta_B$ and that such a solution is unique. This unique solution is the key to the hunting. Furthermore, when $(\theta_A, \theta_B) = (0,0)$, the spot is deviated to its maximum rightmost displacement (maximum value of Δx_e). In other words, all spot displacements of magnitude $r_A + r_B$ will always be brought about by a unique pair of angular RBS displacements. The simplest case is $(\theta_A, \theta_B) = (0,0)$. Given the definition of θ_A and θ_B , this situation corresponds to a spot displacement of $r_A + r_B$ in the x-direction and 0 in the y-direction.

A general algorithm for determining a known (θ_A, θ_B) given an unknown arbitrary initial angular displacement (θ'_A, θ'_B) of the RBSs and an arbitrary $(\Delta x'_e, \Delta y'_e)$ is thus:

- 1) Keeping RBS B fixed, rotate RBS A until spot is at position $(\Delta x_{emaxA}, \Delta y_{exmaxA})$, which is a maximum displacement in the +x direction.
- 2) Keeping RBS A fixed in the position just obtained, rotate RBS B until spot is at position $(\Delta x_{emaxB}, \Delta y_{exmaxB})$, where Δx_{emaxB} is the maximum displacement in the +x direction obtained by rotating RBS B.
- 3) Let $(\theta_A, \theta_B) = (0, 0)$
- 4) Let the new $(\Delta x_e, \Delta y_e) = (\Delta x_{emaxB}, \Delta y_{exmaxB})$

$(\Delta x_e, \Delta y_e)$ and (θ_A, θ_B) can then be fed into the steady-state algorithm described in subsection 4.3.6.

As stated above, a Matlab™ simulation was performed on the hunting algorithm. The results of the hunting simulation are shown in Figure 4.11. The RBSs are sequentially rotated until the spot is at its rightmost displacement. The spot is determined to be at its rightmost displacement when the x value starts to decrease for the first time after it had been monotonically increasing. The theoretical error in this determination is bounded by the angular resolution of the RBS rotation: if at each step the RBS rotates by 1° , the worst case error will be 1° .

4.3.8 Resolution of RBS angular movement required for $1 \mu\text{m}$ alignment accuracy

From an optomechanical point of view, it is interesting to determine what angular rotation of an RBS is required to achieve a spot movement of $\varepsilon = 1 \mu\text{m}$:

Let ϕ = angular rotation (in radians) of 1 RBS corresponding to a spot displacement of ε .

By simple geometry:

$$\phi = \frac{\varepsilon}{r} \quad (4.29)$$

For example, if $r = 242 \mu\text{m}$ (a value determined by the components used in the actual demonstrator) then $\phi = 1/242 \text{ rad}$ (0.23°) is required for a $1 \mu\text{m}$ resolution. This is a major constraint driving the choice of the stepper motors and the optomechanics.

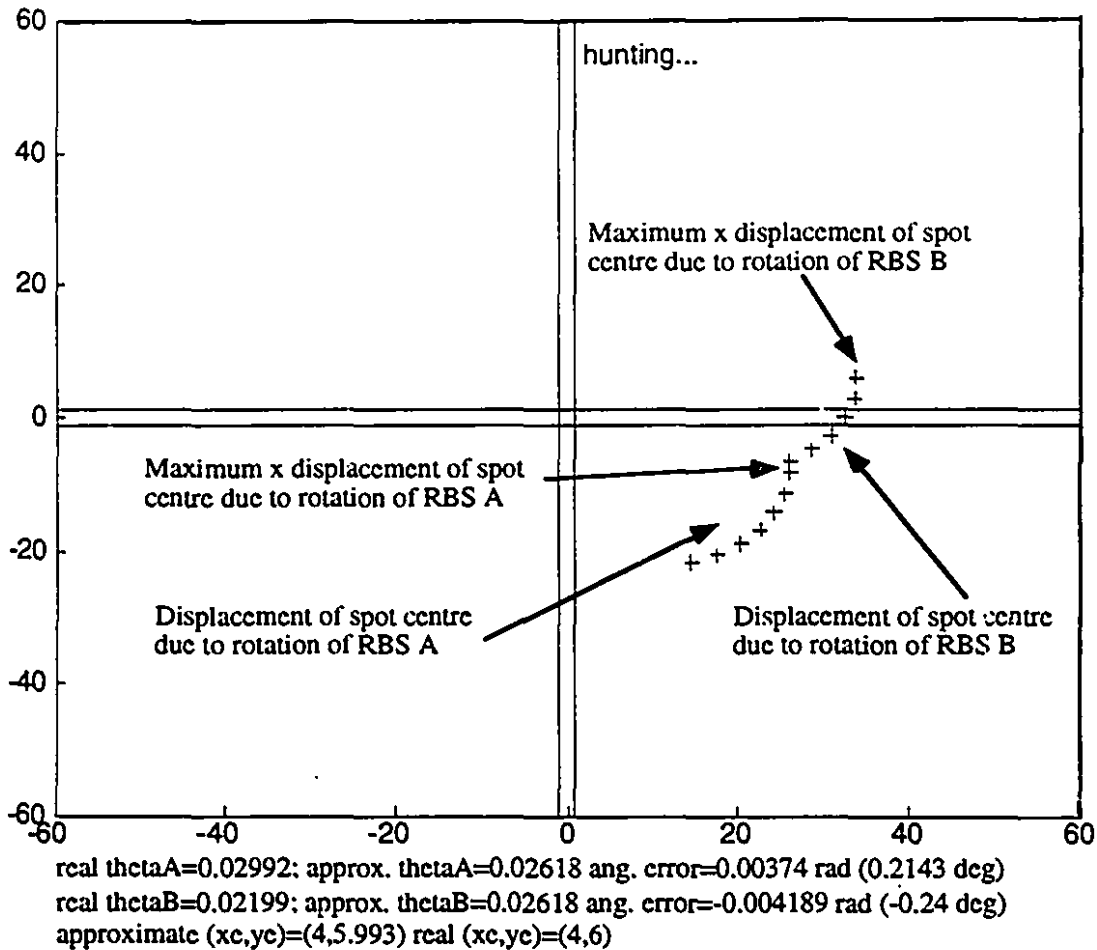


Figure 4.11: Result of hunting algorithm simulated on Matlab™.

4.3.9 Simulation of movement due to rotating RBSs

In order to verify the validity of the algorithm and illustrate the movement brought about by rotating RBSs, simulations were written and executed under Matlab™. In Figures 4.12 through 4.15, a sequence of perturbations and automatic realignments is simulated. The meaning of the displayed values is as follows:

oldthetaA, oldthetaB: current values of RBS angular rotation

xu, yu: position of spot had there been no RBS

xe, ye: magnitude of perturbation that has just occurred.

thetaA, thetaB: calculated value of RBS angle which will recentre the spot

In these simulations, the RBSs are moved one after the other in order to show the movement. In the real demonstrator, however, they are moved concurrently. As well, the simulations show only the centre of the spot. The spot itself is considerably larger.

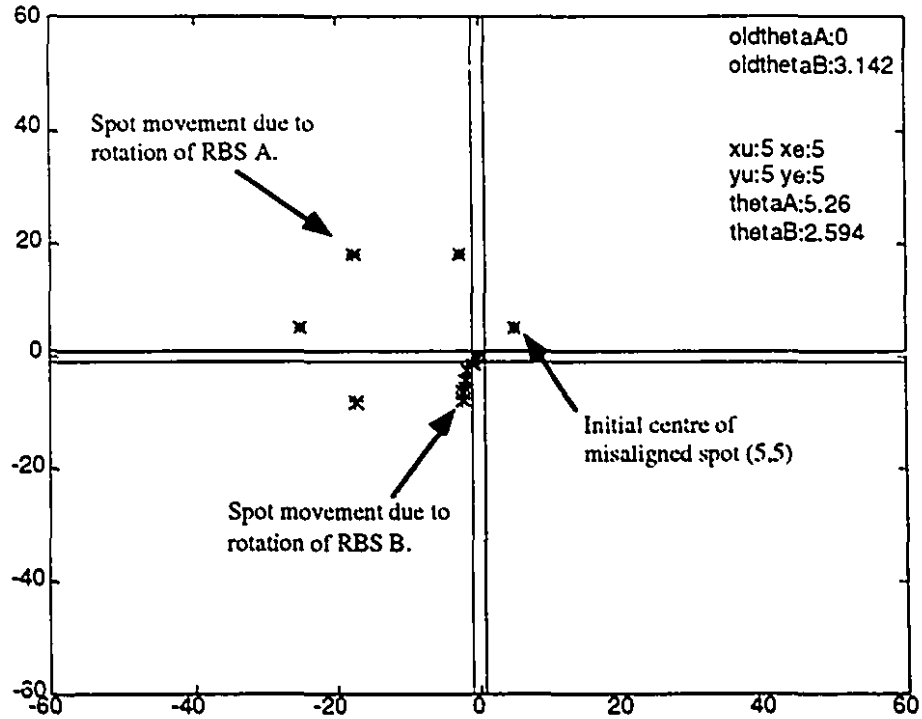


Figure 4.12: Simulation of RBS rotation required to centre spot on QD after perturbation of $(\Delta x_e, \Delta y_e) = (5, 5)$. Angles are in radians, displacements are in arbitrary units.

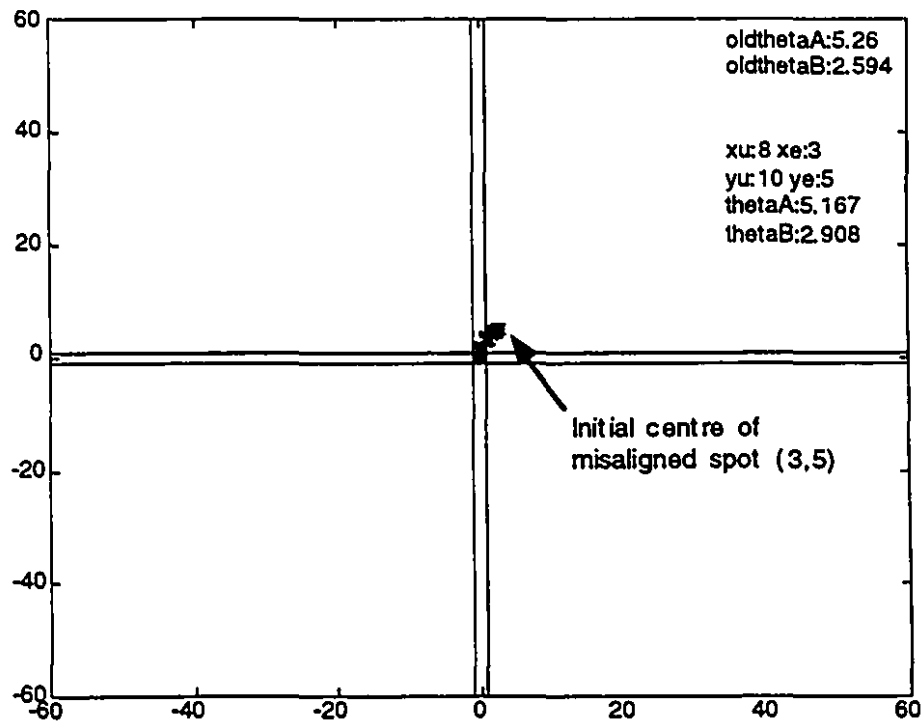


Figure 4.13: Continued from Figure 4.12. Simulation of RBS rotation required to centre spot on QD after second additional perturbation of $(\Delta x_e, \Delta y_e) = (3, 5)$.

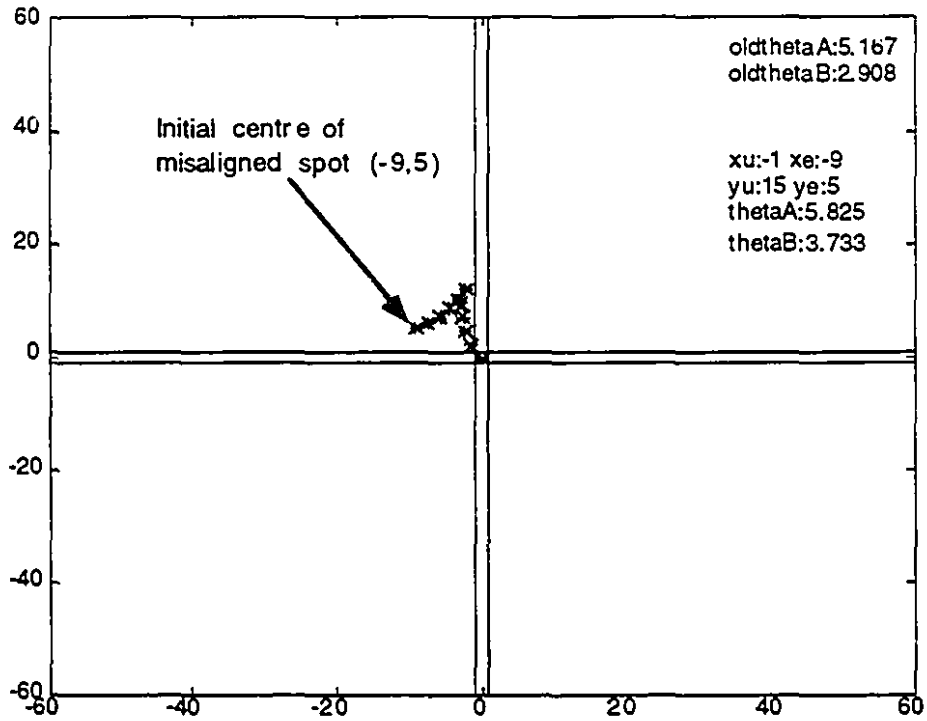


Figure 4.14: Continued from Figure 4.13. Simulation of RBS rotation required to centre spot on QD after third additional perturbation of $(\Delta x_e, \Delta y_e) = (-9, 5)$.

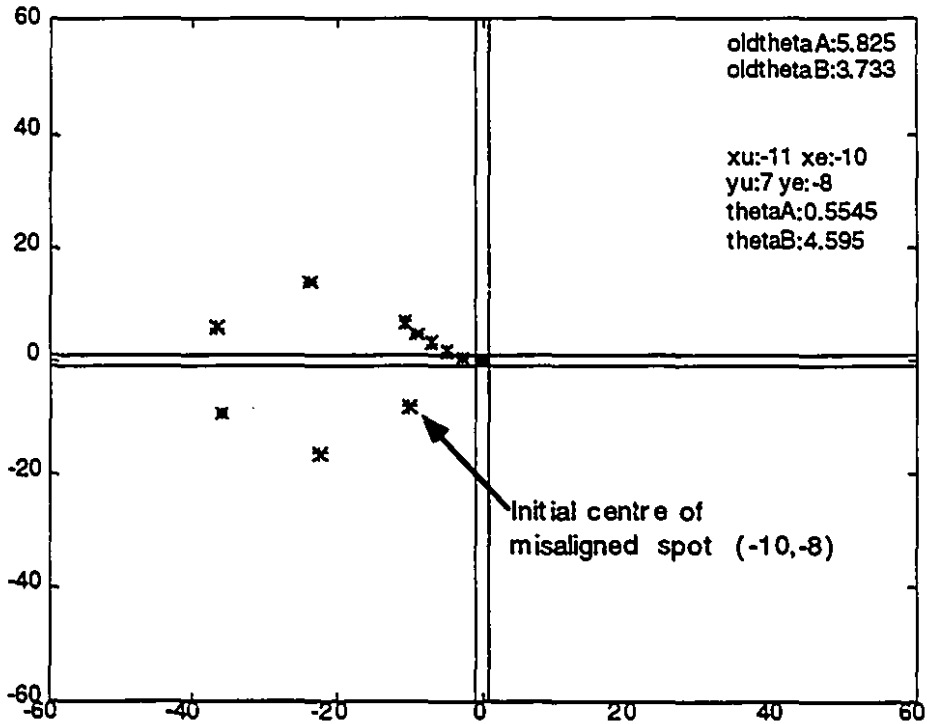


Figure 4.15 Continued from Figure 4.14. Simulation of RBS rotation required to centre spot on QD after fourth additional perturbation of $(\Delta x_e, \Delta y_e) = (-10, -8)$.

4.4 Conclusion

The theory, design and simulation of the demonstrator given in this chapter indicate that an active alignment demonstrator using RBSs is indeed possible.

A method for determining the misalignment error of a spot impinging on a QD was described and analyzed. A novel algorithm for centering a spot in the x-y plane using RBSs was derived. Potential sources of inaccuracies such as the effect of first order optics and the finite resolution of stepper motors were identified and quantified.

The building and testing of the demonstrator described in the next two chapters reveal these and other issues.

4.5 References

- [1] Hamamatsu Multi-Element Silicon Photodiodes Data Sheet KMP01001E01, QD # S4349.
- [2] F. B. McCormick, F. A. P. Tooley, T. J. Cloonan, J. L. Brubaker, A. L. Lentine, R. L. Morrison, S. J. Hinterlong, M. J. Herron, S. L. Walker, and J. M. Sasian, "Experimental investigation of a free-space optical switching network by using symmetric self-electro-optic-effect devices, *Appl. Opt.*, **31**, 5431 (1992).
- [3] Y. Netzer, "Line-of-Sight steering and stabilization", *Optical Engineering*, **21**, 96 (1982).
- [4] E. Hecht, *Optics*, Addison Wesley Inc., Reading, Mass. p. 164 (1987).

Chapter 5

Design and construction of active alignment demonstrator

5.1 Introduction

In this chapter, the main steps in the construction of the demonstrator which successfully implemented the active alignment algorithm using RBSs are outlined. By outlining the main steps carried out during the actual construction, it is shown that various engineering disciplines were required to build a real system based on a theoretical design. A schematic of the built system is shown in Figure 5.1. The complete system was designed and built in the lab over the course of several months.

Over the course of the system construction, optical, optomechanical, optoelectronic and computer considerations imposed engineering constraints which had to be addressed. The schematic in Figure 5.1 as well as the constraints encountered and solutions chosen are further explained in the sections below. Section 5.2 explores the optoelectronic and electronic devices and circuitry that were used, and describes the tests that were performed to characterize these. Section 5.3 addresses optical issues such as lens focal length and spot size, as well as the methodology followed to produce the desired spot size on the quadrant detector (QD). Section 5.4 describes the power train used to couple the power of each motor to its respective RBS holder assembly in order to rotate the RBS to the angular position calculated by the algorithm. The design and fabrication of the RBS holder assembly itself is also discussed. Section 5.5 describes the issues involved in the optomechanical packaging of the QD onto a support plate which is bolted onto a Newport x-y-z positioner. It is shown that packaging issues are vitally important: for example, a small rotational misalignment of the QD package can cause a substantial error in the misalignment error (Δx_e , Δy_e) input to the algorithm. Finally, section 5.6 briefly overviews the computing platform, both hardware and software, on which the algorithm was encoded.

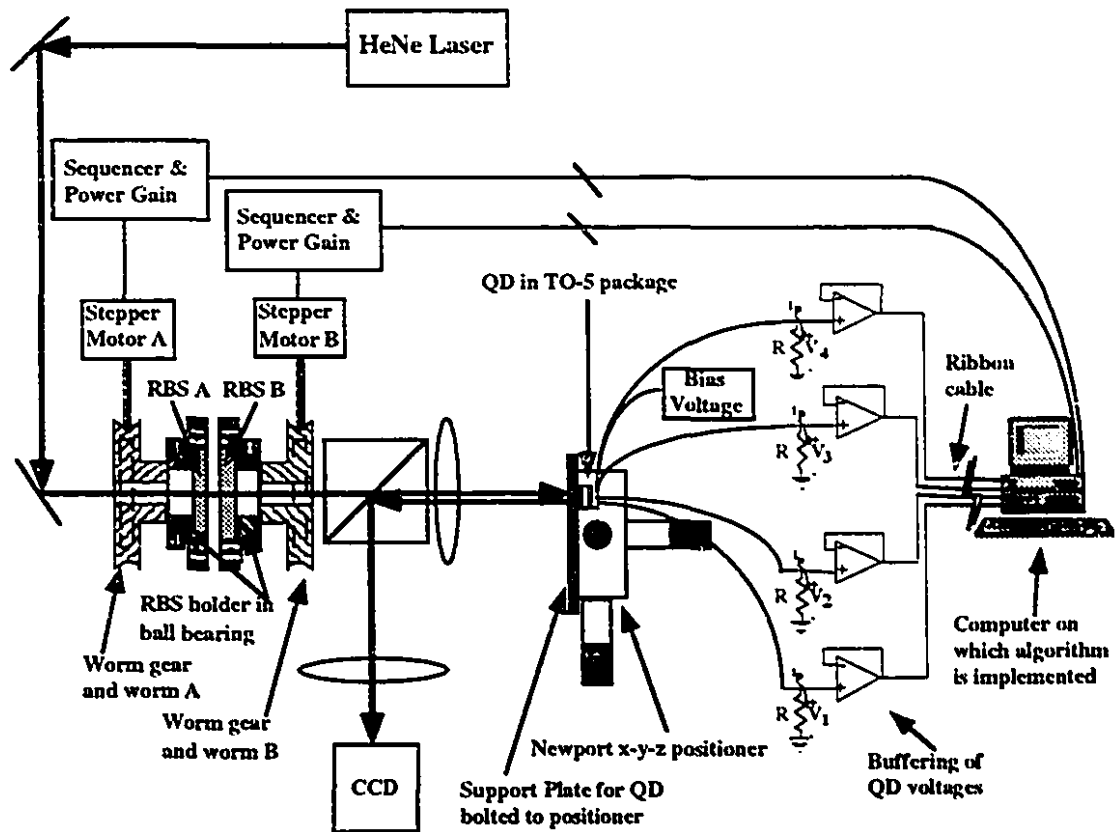


Figure 5.1: Setup of active alignment demonstrator (Illumination LED not shown for simplicity).

5.2 Optoelectronics and electronics for detection and transmission of error signal

5.2.1 Choice of resistor value

The QD chosen for the demonstrator was the Hamamatsu S4349 which has a measured optoelectronic sensitivity of 0.41 A/W , as is indicated in subsection 5.2.3. The Hamamatsu S4349 has the following geometry: $a = b = 1500 \text{ }\mu\text{m}$ and $2g = 100 \text{ }\mu\text{m}^{(1)}$, where a , b , and g are defined in Figure 4.2 .

Given the power of the HeNe laser used in the demonstrator and the losses in the optical train, the total measured light power of the spot on the QD was $73 \text{ }\mu\text{W} \pm 3\%$. Since it was desired to have a maximum voltage swing of approximately 10 V , the resistor value was calculated as follows.

From Eq. (4.1) and Figure 4.4:

$$\begin{aligned} \frac{V}{R} &= i_p = (\int \text{irradiance on photosensitive area} \times dA) \times S \\ &= 73\mu W \times 0.41 \\ \implies R &= \frac{V}{73\mu W \times 0.41} = \frac{10}{73\mu W \times 0.41} = 334 \text{ k}\Omega \end{aligned} \tag{5.1}$$

To simplify circuit assembly, the closest standard resistor value (330 k Ω) was chosen. This choice of a practical resistor added an error of $\sim 1\%$, and was deemed tolerable since it simplified circuit assembly. However, care was taken to choose resistors that were as closely matched as possible.

A plot of the ideal voltage swing vs misalignment in the x direction, (ΔV_x vs Δx_e) for a spot displacement along the $\Delta y_e = \Delta x_e$ line is shown in Figure 5.2. This plot is similar to Figure 4.5. The difference between these two plots, however, is that Figure 5.2 incorporates the real physical values for the experimental setup, not arbitrary units or normalized values.

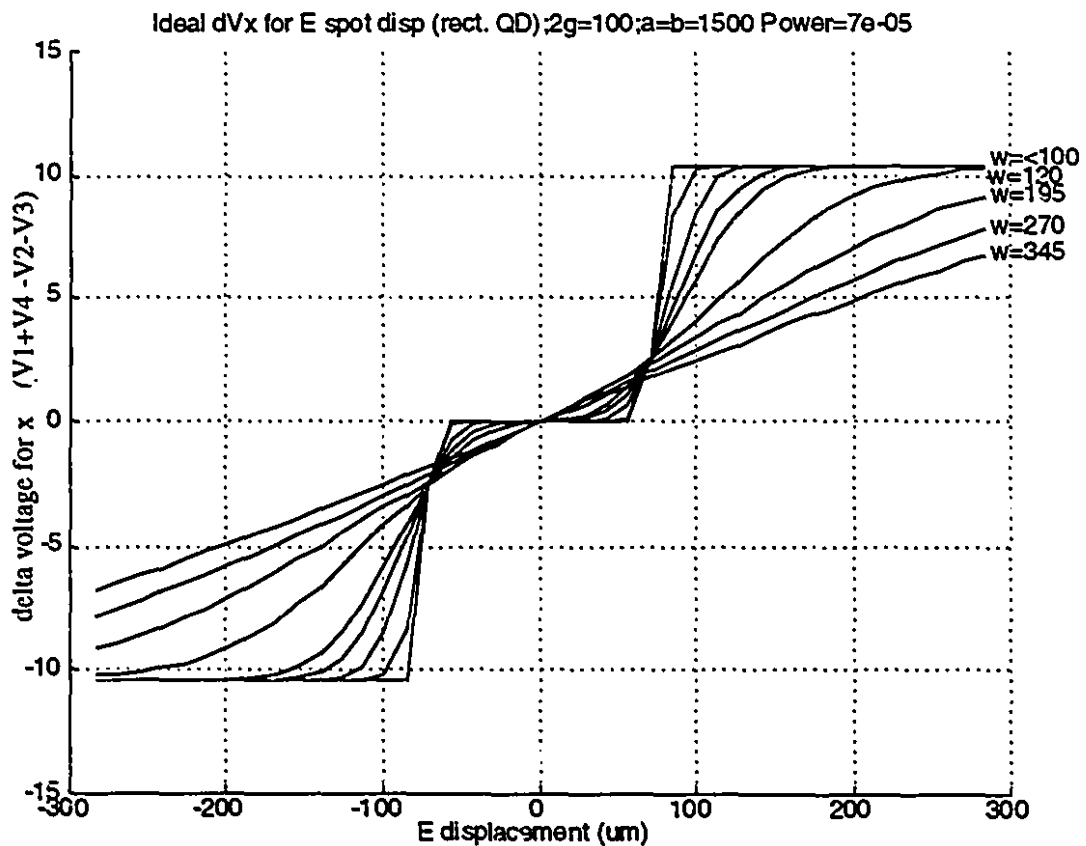


Figure 5.2: Ideal dV_x for spot displacement along $\Delta y_e = \Delta x_e$ line (rectangular QD) using actual physical parameters.

5.2.2 Choice of reverse bias voltage for photodetectors on quadrant detector

Another key parameter to choose was the voltage applied to the biasing circuit, V_a , shown in Figure 5.3. An experiment was conducted to determine the range of desirable V_a . In this experiment, a small spot was focused onto the middle of quadrant 2 (Q2). The voltages V_1 , V_2 , V_3 , and V_4 , were measured as V_a was swept from 0 to 20 V, which is the breakdown voltage specified in the data sheets ⁽¹⁾. The resulting measured values are plotted in Figure 5.4.

The analysis of Figure 5.4 yields insight about the circuit operation. For the illuminated Q2, the maximum voltage across R_2 should be: $V_2 = 73 \mu\text{W} \times 0.41 \text{ A/W} \times 330 \text{ k}\Omega = 9.9 \text{ V}$, as was calculated in subsection 5.2.1. ($R_1 = R_2 = R_3 = R_4 = R = 330 \text{ k}\Omega$). However, Kirchoff's voltage law dictates that $V_2 = V_a + V_{bi}$, where V_{bi} is the built-in voltage of the diode. Consequently, V_2 increases with increasing V_a , until $V_2 = 9.9$, at which point V_2 does not increase for increasing V_a . Figure 5.4 also indicates that for this diode, $V_{bi} = 0.5\text{V}$.

For Q1, Q3, and Q4, the analysis is as follows. For low reverse bias voltages, the dark current is relatively high and as such the current across R_1 , R_3 , and R_4 is high. This current across the very large $330 \text{ k}\Omega$ resistor causes an appreciable voltage increase up to $V_a + V_{bi}$, for low V_a . However, as the reverse bias voltage increases, the dark current decreases, leading to a smaller drop across the resistors. At $V_a > 10\text{V}$, the ratio of V_x to V_2 , ($x = 1, 3, \text{ or } 4$) is < 0.05 , which is as per the specifications. The reason for the difference between, on one hand V_1 and V_3 , and, on the other hand, V_4 , can be attributed to imperfect isolation between the active regions: more of the photocurrents of Q2 go to the quadrants adjacent to Q2, namely Q3 and Q1, than to the farthest quadrant Q4. An analogous behaviour was observed when the spot was kept on the other quadrants.

The conclusion from this experiment was that the applied voltage V_a should be kept in the range $10 \text{ V} \leq V_a < 20$. A value of $V_a = 10 \text{ V}$ was chosen for the experiment.

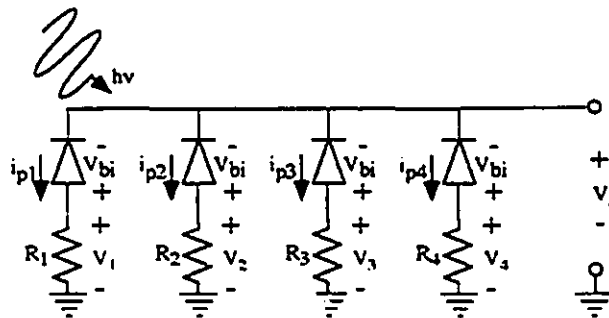


Figure 5.3: Ideal representation of quadrant detector as well as external biasing circuit and resistors.

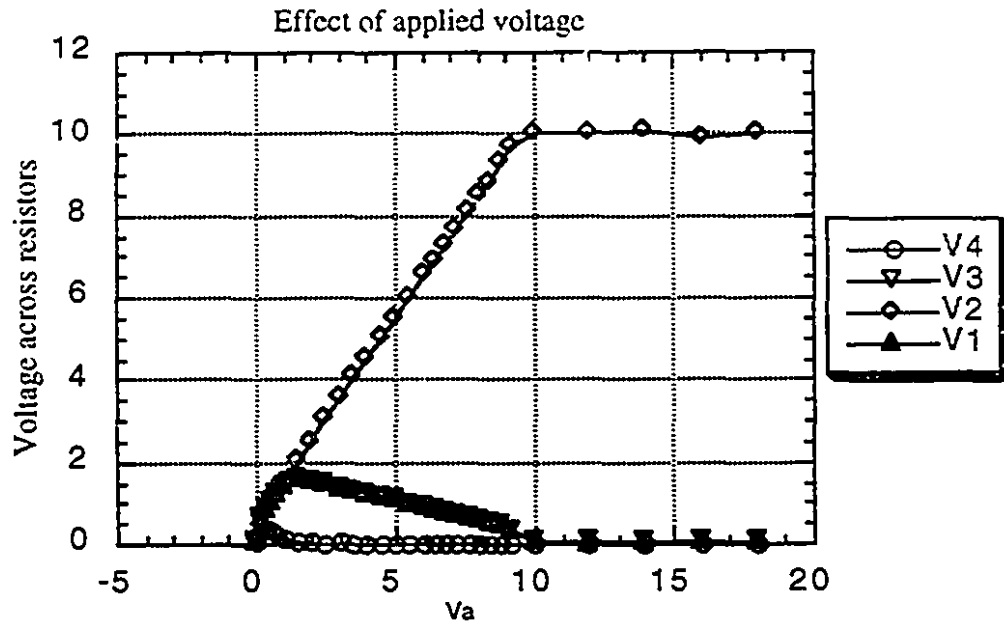


Figure 5.4: Effect of applied voltage, V_a on measured voltages V_1 , V_2 , V_3 , V_4 created by photocurrents across resistors. Focused spot is located at the centre of Quadrant 2.

5.2.3 Uniformity of optoelectronic sensitivity on quadrant detector

The uniformity of the optoelectronic sensitivity, S , is vital: any non-uniformity in S will produce inconsistent photocurrents for an equal illumination, leading to incorrect measurements of $(\Delta x_e, \Delta y_e)$. In order to determine the uniformity of S , measurements were taken at various positions along a quadrant of the QD.

The basic theory is as follows. Figure 5.3, indicates that incident light creates a photocurrent, i_p , which creates a voltage across resistor R ($330 \text{ k}\Omega$). For a total incident light power P_B , the sensitivity is:

$$S = \frac{V}{RP_B} \quad (5.2)$$

For these measurements, the QD was moved such that the full power of the spot impinged on various positions within one quadrant of the QD. At each position, the voltage across the resistor was measured.

A schematic of the components used for the optoelectronic sensitivity measurement as well as their layout is shown in Figure 5.5. The experiment lasted an hour because many points were taken. Since previous measurements indicated that the laser fluctuated by $\pm 3\%$

over this long time span, it was necessary to determine the incident power P_B for each voltage measurement. For every measurement, P_B was determined as follows. P_A was measured using a Newport 1835C power meter and P_B was determined by multiplying P_A by the ratio P_B/P_A , which had previously been measured: $P_B/P_A = 0.855 \pm 0.008$. (Ideally, $P_B/P_A = 1$; this deviation from the ideal can be attributed to 2% reflection losses at each lens surface, as well as to a non-ideal 50:50 beam splitter). As such, all the terms in Eq 5.2 were known for every measurement and the sensitivity could be calculated for every point.

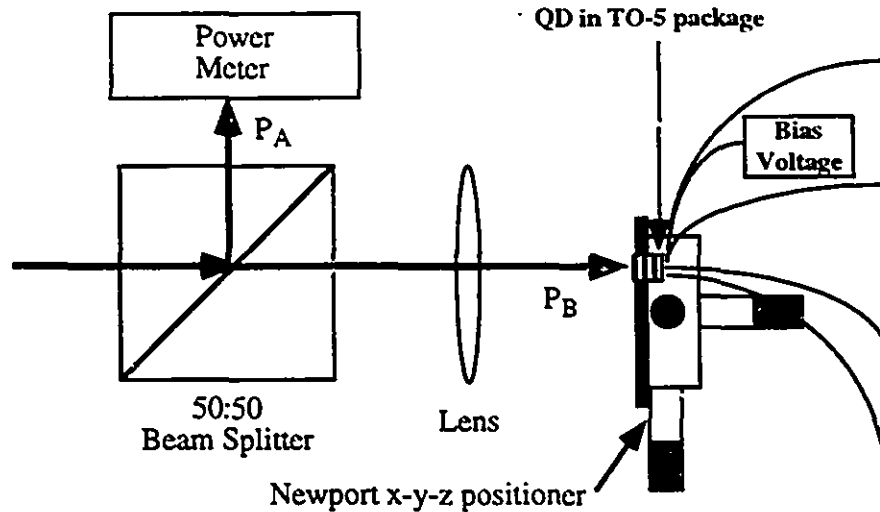


Figure 5.5: Schematic of Optoelectronic sensitivity measurement setup.

The QD was moved such that the spot followed a trajectory along lines 1 and 2 indicated in Figure 5.6. Measurements were made every $50\sqrt{2}$ μm along trajectory 1, and every 50 μm along trajectory 2.

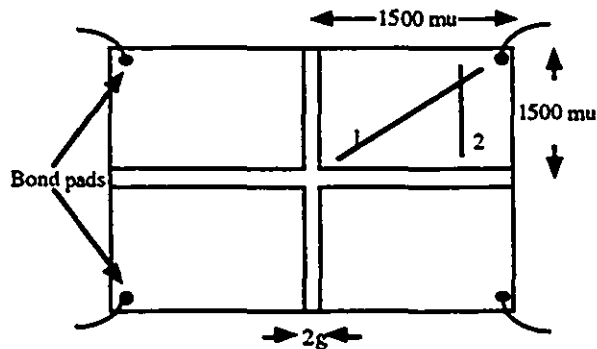


Figure 5.6: Trajectories along which measurements were taken.

The results of the optoelectronic sensitivity measurements are plotted in Figure 5.7.

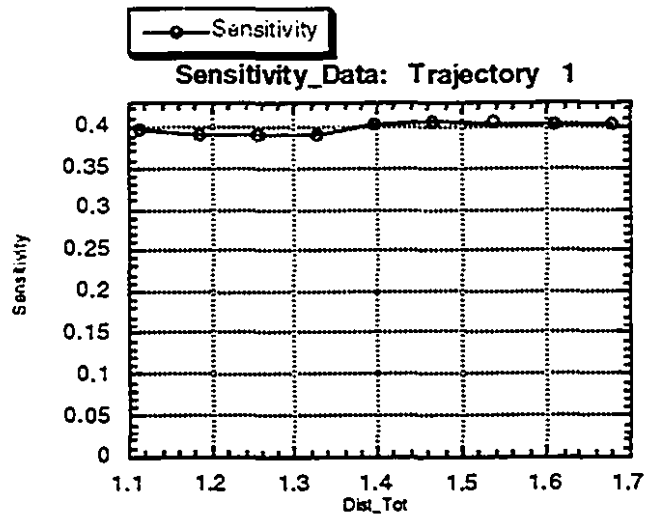


Figure 5.7a): Sensitivity vs total displacement from QD centre, trajectory 1.

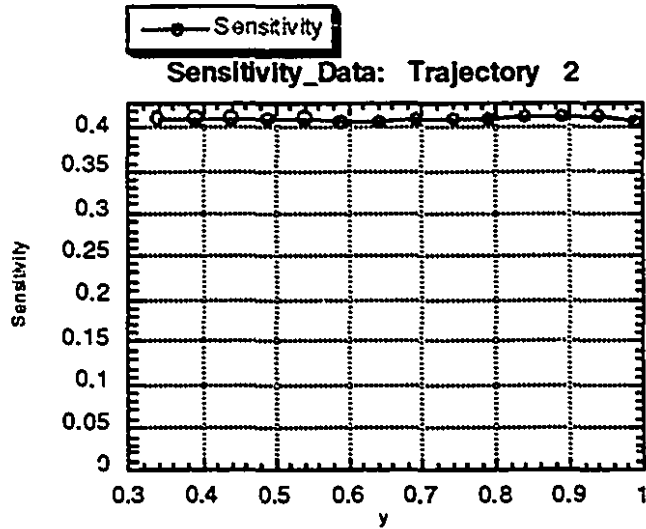


Figure 5.7b): Sensitivity vs y displacement from QD centre, trajectory 2.

Statistical analysis indicates that the uniformity is excellent:

Minimum	0.39066547
Maximum	0.41469944
Points	23
Mean	0.4060216
Median	0.40795931
Std Deviation	0.0072219883
Variance	5.2157115e-05

Table 5.1: Statistical analysis of optoelectronic sensitivity of active area on quadrant of QD.

5.2.4 Experimental analysis of the analog signal transmission setup

Not only was it important for the photocurrents produced by the QD to be consistent in order to produce consistent voltages, it was also important for the computer to properly detect and sample these voltages in order to properly calculate the misalignment error (Δx_e , Δy_e) for input into the algorithm. A Lab-NB™ A/D (Analog to Digital) Board from National Instruments was installed on the computer to perform the sampling. Since the spot only moved very slowly in this experiment, the sampling rate of thousands of samples per second was largely sufficient.

Figure 5.8 indicates how each voltage V_1 , V_2 , V_3 and V_4 , was buffered and then sent down a 15 m ribbon cable to the computer which sampled the voltages and implemented the algorithm using the sampled data (the 15 m length of the interconnect was unfortunately dictated by the layout of the lab and the experimental setup). Measurements were performed to determine if there was a significant difference between the true voltage (located at point T of Figure 5.8) read using a conventional oscilloscope, and the voltage input into the algorithm (displayed on the computer screen), which was affected by the combined effects of the buffering, the transmission and the sampling.

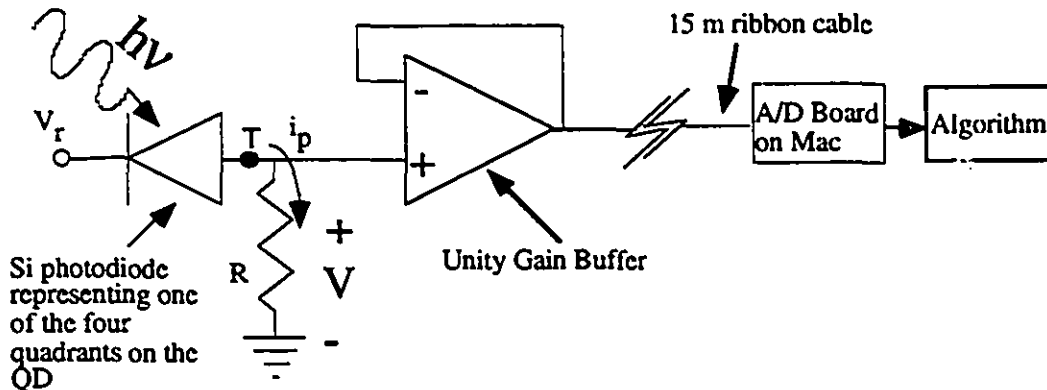


Figure 5.8: Schematic of analog signal transmission setup from detector to algorithm

Various voltage values were compared on each of the four setups (i.e. one for each quadrant) in order to determine the error between the true voltage and the voltage input to the algorithm; these plots are shown in Figure 5.9. Furthermore, statistical analysis in Table 5.2 shows that these two values are on average very close, on the order of 1%. Finally, since these values are subtracted from each other in order to determine the error signal (Eq. 4.2), the effects of the consistently negative mean were reduced. What errors there were can be attributed to many factors:

1) Laser fluctuations: since it took about 90 seconds to measure the 4 voltages with the oscilloscope, write down the values in the notebook, and then walk over to the computer to read off the 4 sampled voltages, the laser could easily have fluctuated within its specified $\pm 1\%$ short term power stability⁽²⁾.

2) Quantization error: the A/D board has a 12 bit representation, which means that the mean error is $10\text{ V} / (2 \times 2^{12}) = 1.22\text{ mV}$.

3) EMI (Electromagnetic Interference): Given the noisy lab environment, the signal could have been corrupted as it propagated along the long 15 m ribbon cable which acted as a long antenna.

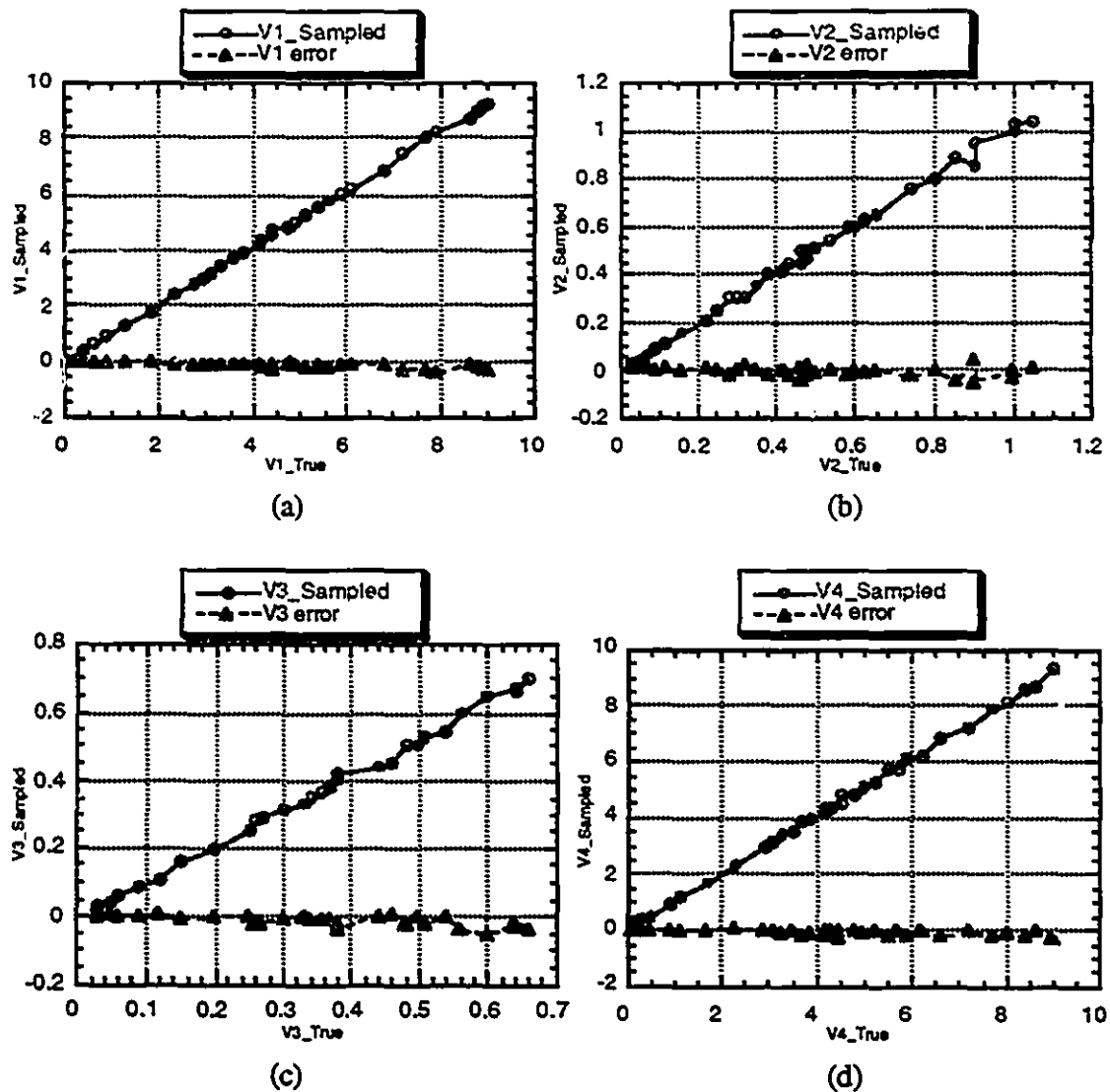


Figure 5.9: Plots of (true voltage) vs (sampled voltage) along with difference between the two (a) Quadrant 1 (b) Quadrant 2 (c) Quadrant 3 (d) Quadrant 4.

	V1 true-sample	V2 true-sample	V3 true-sample	V4 true-sample
Minimum	-0.40	-0.050	-0.049	-0.300
Maximum	0	0.039	0.010	0.049
Points	34	34	34	34
Mean	-0.137	-0.004	-0.013	-0.078
Median	-0.10	0	-0.009	-0.044
Std Deviation	0.102	0.018	0.016	0.096
Variance	0.010	0.0003	0.0002	0.009

Table 5.2: Statistical analysis on error between true voltages and voltages input to algorithm after buffering, transmission over 15 metres, and sampling.

5.3 Determination of optical parameters

In this subsection, the theoretical results obtained in chapter 4 are used to determine the focal length of the lens, and the best size of the spot impinging on the quadrant detector (QD). The method implemented to physically obtain a spot of this size on the QD is also given.

5.3.1 Choice of lens focal length

In chapter 2, it was shown that a mechanical insertion of a PCB into an existing backplane could yield a misalignment of $\sim \pm 100 \mu\text{m}$. Consequently, $100 \mu\text{m}$ was chosen as a minimum misalignment error to be corrected by the RBSs. It was thus necessary to ensure that the movement imparted by the RBSs could cover at least a circle of radius $100 \mu\text{m}$. As stated in Chapter 4, two RBSs each of wedge angle β can impart a maximum displacement of $d = 2 \times f \times \tan((n-1)\beta)$, where f is the lens' focal length. Given RBSs of BK7 ($n = 1.5$ at $\lambda = 632.8 \text{ nm}$), and nominal wedge angles of $\beta = 0.25^\circ$ for both RBSs, the minimum acceptable f was: $f = 22.9 \text{ mm}$. A lens of focal length $f = 100 \text{ mm}$ was chosen; this allowed for a total theoretical radius of action of $2 \times f \times \tan((n-1)\beta) = 436 \mu\text{m}$, largely sufficient for a $\pm 100 \mu\text{m}$ displacement as well as for experimenting with further displacements of larger magnitude.

Measurements of the wedge angles of the RBSs used in the demonstrator indicated that their wedge angles were actually $\beta_A = 0.208^\circ \pm 2\%$ and $\beta_B = 0.278^\circ \pm 2\%$. The RBSs were nonetheless used since those were the only RBSs available at the time. However, since the algorithm was designed for arbitrary wedge angles, this was not a major problem.

5.3.2 Theoretical and experimental determination of optimal spot size and measurement sensitivity constant

In order to obtain linear voltage changes (ΔV_x and ΔV_y) for spot displacements of $\pm 100 \mu\text{m}$ about the centre of the QD, Figure 5.2 indicates that a spot of $w = 195 \mu\text{m}$ yields a linear relationship up to a displacement of $\sim 200 \mu\text{m}$. Furthermore, a spot of $w = 195$ will still bring about monotonically increasing voltage changes (ΔV_x and ΔV_y) for displacements considerably above $200 \mu\text{m}$; these further voltage changes, however, will not be linearly proportional to the spot displacement, as can be seen by the non-linear rolloff of the curves for large displacements in Fig 5.2.

Two different approaches were considered for obtaining a spot of $w = 195 \mu\text{m}$.

The first approach consisted of illuminating the imaging lens of Figure 5.10a) with a Gaussian beam having a specific w_{beam} . Eq (5.3) was used to determine the specific w_{beam} required to achieve a spot $w = 195 \mu\text{m}$:

$$w = \frac{f\lambda}{\pi w_{beam}} \quad (5.3)$$

Given the focal length $f = 100 \text{ mm}$ and the 632.8 nm wavelength of the HeNe laser used in the experiment, Eq 5.3 can be solved for w_{beam} , yielding $w_{beam} = 103 \mu\text{m}$.

The second approach consisted of defocusing the beam as shown in Figure 5.10b).

Given an incoming beam having an approximately Gaussian profile with a diameter (e⁻² points) of $2w_{oi} = 4.38 \text{ mm}$, the diameter of the waist of the beam leaving the lens is $2w_{ol} = 18.4 \mu\text{m}$. The size of the spot $w(z_d)$ on the QD as a function of the defocus z_d is then analogous to Eq (4.4):

$$w^2(z_d) = w_{ol}^2 \left[1 + \left(\frac{\lambda z_d}{\pi w_{ol}^2} \right)^2 \right] \quad (5.4)$$

Solving (5.4) for z_d in order to obtain $w(z_d) = 195$ yields $z_d = 8483 \mu\text{m}$.

After considering both approaches, the second approach was chosen: since the QD was already mounted on an x-y-z positioner with micrometers, it was simpler to slightly defocus the QD than it was to place additional optics to change the beam dimensions. However, the system had to be as telecentric as possible: as a result, the RBSs were both inserted as near the lens' front focal plane as possible.

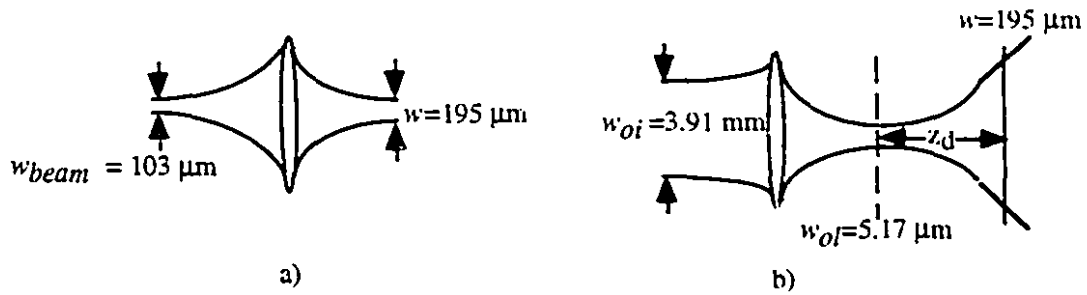


Figure 5.10: Two different approaches for obtaining a spot of $w=195 \mu\text{m}$ a) small incoming w_{beam} b) defocus of a telecentric system.

Once the optimal spot size was achieved, the QD was moved such that the spot swept along the $\Delta y_e = \Delta x_e$ trajectory shown in Figure 4.6; the voltages across the resistors were taken at regular intervals along the trajectory. The resulting voltages across the resistors were used to calculate ΔV_x (Eq. 4.3). Figure 5.11 compares two curves: the plot of theoretical ΔV_x vs Δx_e and the plot of measured ΔV_x vs Δx_e for Δx_e displacements along the $\Delta y_e = \Delta x_e$ line. The measured data in the plot of Figure 5.11 indicates that the theoretical voltage values very closely match the measured ones. The plot of ΔV_y vs Δy_e was similar. The discrepancies between the theoretical and measured voltages can be explained by the fact that the spot had a non-ideal Gaussian irradiance distribution. Causes of the non-ideal Gaussian irradiance distribution are given in section 5.7.

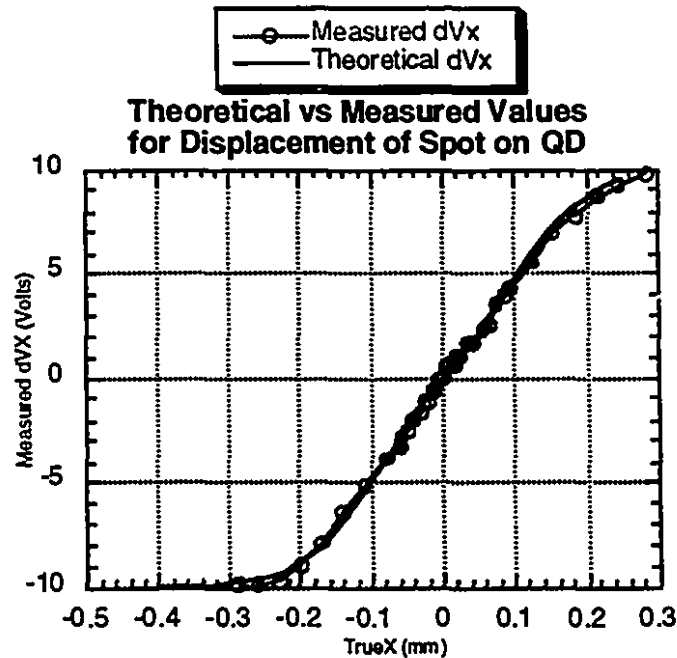


Figure 5.11: ΔV_x vs Δx_e for spot displacement along $\Delta y_e = \Delta x_e$ trajectory shown in Figure 4.6.

Having determined the optimal spot size which yielded a linear ΔV_x and ΔV_y for the misalignment errors of interest, it was necessary to determine the measurement sensitivity k in Eq. (4.2) which related the measured differential voltages, ΔV_x and ΔV_y , to actual misalignment errors, Δx_e and Δy_e respectively. From Eq (4.2), it can be seen that k is the slope of the linear region of the ΔV_y vs Δy_e or ΔV_x vs Δx_e curves. By calculating the slope of the linear region of the curve in Figure 5.11, k was determined to be: $k=26.6 \mu\text{m/V}$. This measurement sensitivity was valid only for small displacements ($<200 \mu\text{m}$). It can be seen from the graph that multiplying ΔV_x by k for larger displacements ($>200 \mu\text{m}$) yielded a measured misalignment error that was smaller than the actual misalignment error.

5.4 Optomechanical design and actuator issues

5.4.1 Power train from actuator to RBS holder

As stated above, the active alignment demonstrator centered a spot by rotating two RBSs to angular positions determined by the algorithm. Two 48-step motors from H&R Inc. (i.e. one for each RBS) were chosen to rotate the RBSs. A 48 step motor has an angular resolution of $360^\circ/48=7.5^\circ/\text{step}$. As such, in order to achieve the angular resolution of $<1^\circ$ specified in subsection 6.3.8, a worm gear setup was used to rotate the RBSs. The worm and worm gear both came from Boston Gear Inc.: worm gear G1024 featuring a diametrical pitch of 31.75 mm (1.2500 inches) and 60 teeth was used in conjunction with worm LSH-1 to achieve a 60:1 gear reduction. The total theoretical resolution was thus $360^\circ/(48 \times 60)=0.125^\circ$. Worm gear G1024 is shown in Figure 5.12.

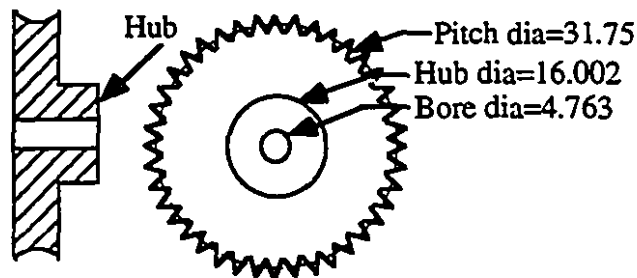


Figure 5.12: Worm gear G1024.

Electrical power considerations were important. As in all stepper motors, there were several windings (4 in this case), and successively energizing the windings in a definite sequence made the motor rotate in discrete steps. Each stepper motor required a DC power

of 330 mA x 6 V at all times, whether or not the motor was moving (one motor winding was energized at all times to ensure a constant holding torque if there was no movement). However, neither the computer (described below) on which the algorithm ran nor other control logic could drive more than a few mA at 5 V (TTL levels). Consequently, there had to be a power gain in order for the computer to drive the motors which rotated the RBSs. The power gain was supplied by a UCN5804B chip. Finally, the motor power was transferred to the worm via a drive shaft coupled to the motor shaft, and the worm rotated the worm gear on the RBS holder assembly.

5.4.2 Fabrication of RBS holder assembly

The two RBSs used were nominally identical and the geometry of each was as follows: each was 18 mm in diameter and 3 mm thick. The nominal wedge angle was 0.25 ° and had a negligible effect on thickness.

Designing and building a holder assembly that allowed for controlled rotation of the RBSs by the power train was a necessary task. For each RBS, an RBS holder assembly was designed and built which consisted of: an RBS, a ball bearing, a worm gear, and an RBS holder mounted into a modified lens holder. Their design and construction is described below.

The design of the RBS holder is shown in Figure 5.13. The RBS holder was custom designed to be glued into ball bearing ABS-A1-68 from Nordex Inc., which has a 25.4 mm (1.0000 inch) outer diameter.

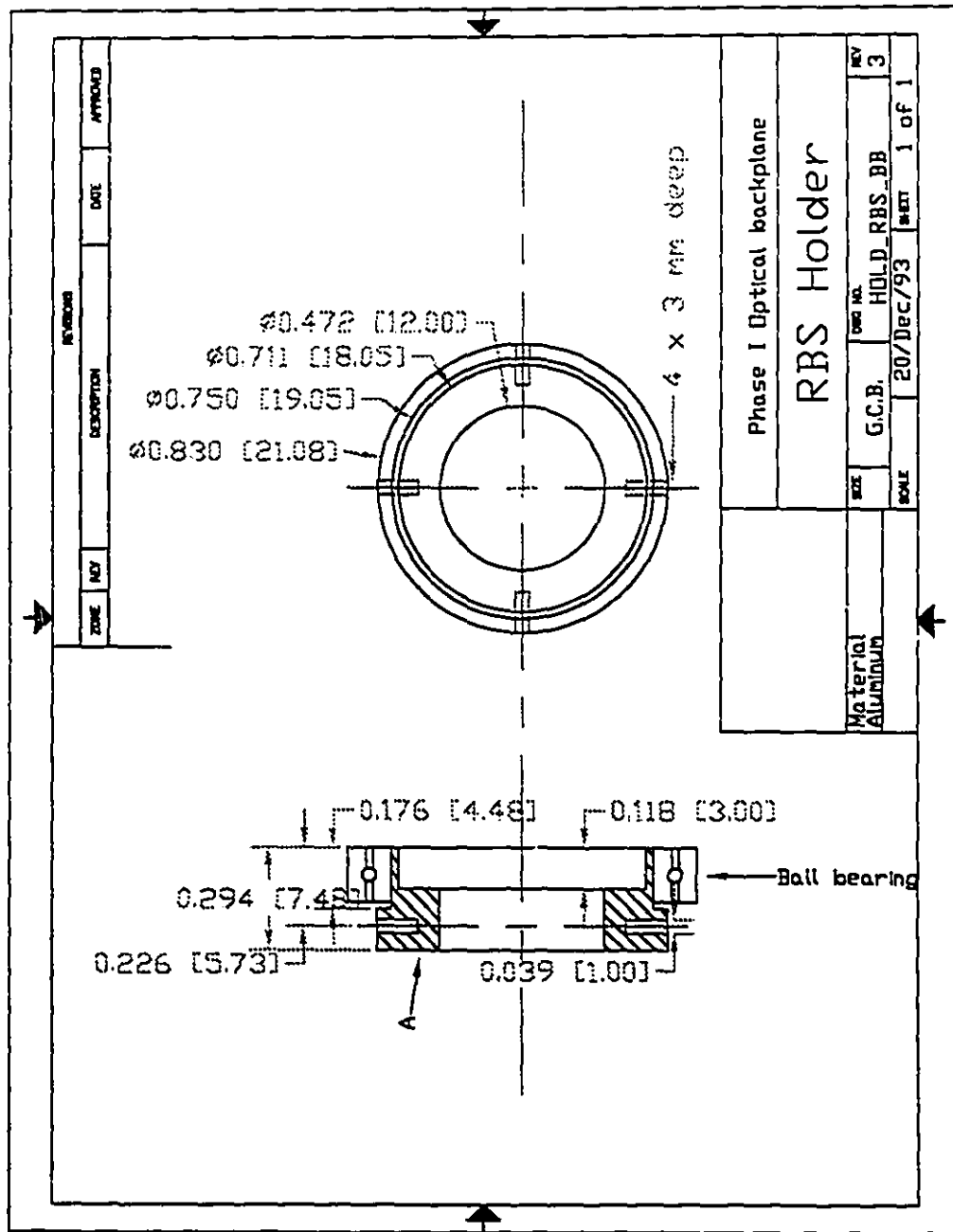


Figure 5.13: RBS holder along with side view of ball bearing. Worm gear must be glued onto face A. RBS glued flat on seat. Tolerances $\pm 25.4 \mu\text{m}$ (± 0.001 inch).

The design of the RBS holder shown in Figure 5.13 was exactly the same design as the one used for the McGill Phase I demonstrator's; as such, it was easy to acquire two of those RBS holders for the active alignment demonstrator. The RBS holder was mounted into a Spindler & Hoyer 061010 mounting plate (modified to have a 1" clear aperture), the RBS holder was glued into the bearing as shown in Figure 5.13, and the RBS was glued

into the RBS holder. However, mounting and centering a worm gear onto this RBS holder assembly was a challenging task. One way would have been to redesign a completely new RBS holder and modify the worm gear in order to bolt the worm gear onto the RBS holder. This presented machining problems and would have taken a long time. Another way was to glue the worm gear onto the RBS holder. The latter course of action (gluing) was chosen and is described in the next paragraphs.

The objective was to centre and glue the worm gear onto face A of the RBS holder. This was a challenging step since it is absolutely vital that a gear be as well centered as possible onto the axis of rotation; failure to do so not only increases backlash but also considerably reduces gear lifetime⁽³⁾. In other words, the bore of the worm gear and the 12 mm clearance hole on the RBS holder had to be concentric. In order to accomplish this step, a gluing jig which facilitated the operation was designed and built. A schematic of this jig is shown in Figure 5.14a). The jig was composed of three main parts: an optomechanical support structure with springs which pressed face A of the RBS holder onto the gear, a Spindler & Hoyer 065070 x-y positioner which moved the RBS holder for fine positioning, and an imaging system which imaged the gear and RBS holder onto a CCD camera.

The imaging system, a 4f system, imaged the centre part of the RBS holder onto the device plane of the CCD. The resulting image simplified measurements taken to ensure the proper centering of the worm gear with respect to the RBS holder. The focal lengths f_1 and f_2 were calculated to image the periphery of the RBS holder's 12 mm clearance hole onto the CCD device plane; f_1 and f_2 thus had to image a 12 mm object onto a device plane of 4.8 x 3.6 mm ⁽⁴⁾. This implied a magnification, M , of at most $M = 0.3$. Since $M = f_2/f_1$, the focal lengths chosen were $f_2 = 10$ mm and $f_1 = 40$ mm. Finally, since the RBS was along the optical path, the total length of the optical train was not simply $2f_2 + 2f_1$, but rather $2f_2 + 2f_1 + \epsilon$, where ϵ compensated for the shorter optical path length seen by the light going through the RBS. For a 3 mm thick RBS made of BK7 ($n=1.5$), $\epsilon = 1$ mm.

The RBS holder was moved with the 065070 x-y positioner until measurements taken on the CCD image indicated that the 12 mm clearance hole on the RBS holder and the worm gear bore were concentric. When concentricity was obtained, RTV 732 elastomer was put on the hub and the RBS holder was lowered onto the hub. The springs ensured a uniform pressure until the glue finished curing, as shown in Fig 5.14b). The final centering accuracy was measured to be better than 100 μ m.

When the complete assembly consisting of the RBS, the RBS holder, the modified lens holder for the RBS holder, and the worm gear was finished, the complete assembly was mounted into the main active alignment setup; the worm was then properly positioned in

order to impart a rotation to the holder, as indicated by Ahmad⁽⁵⁾. Simple pre-loading springs to reduce backlash were also used. A photo of the power train and RBS holder assembly for RBS A is shown in Figure 5.15. The setup for RBS B was similar.

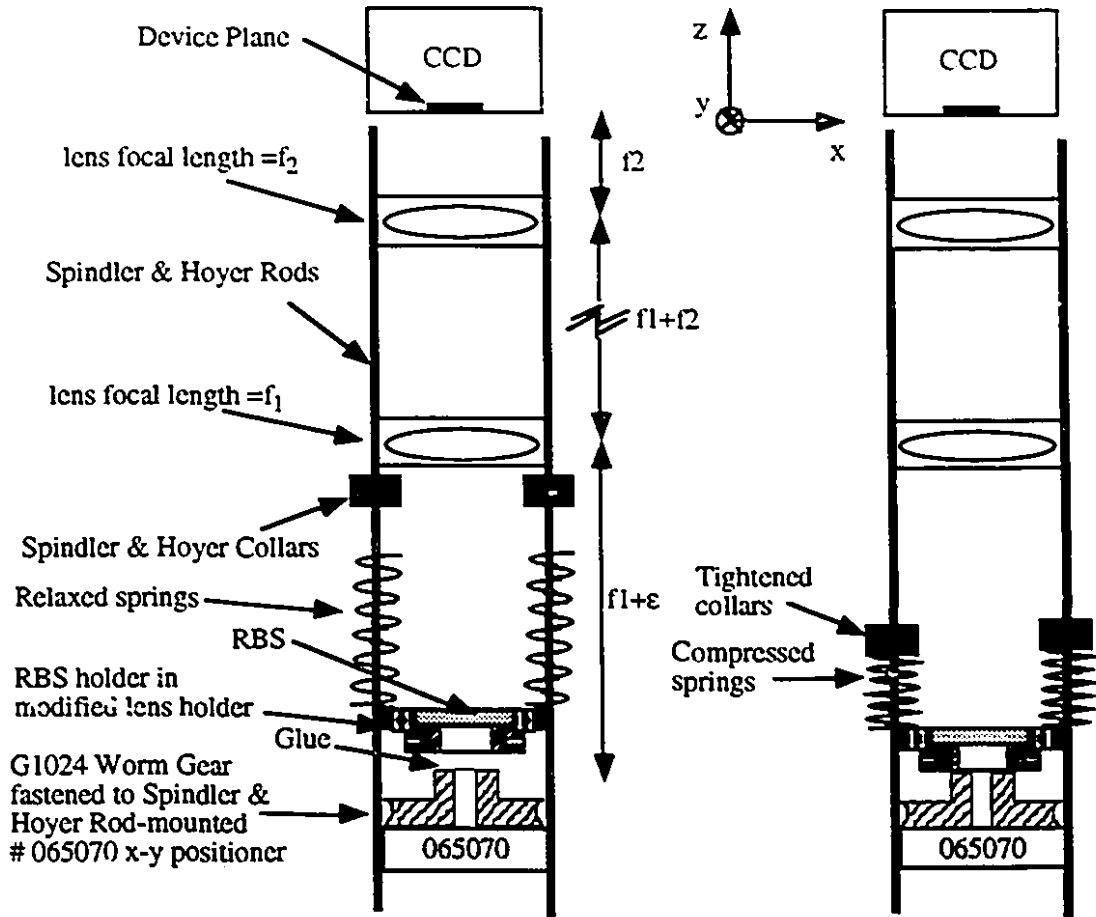
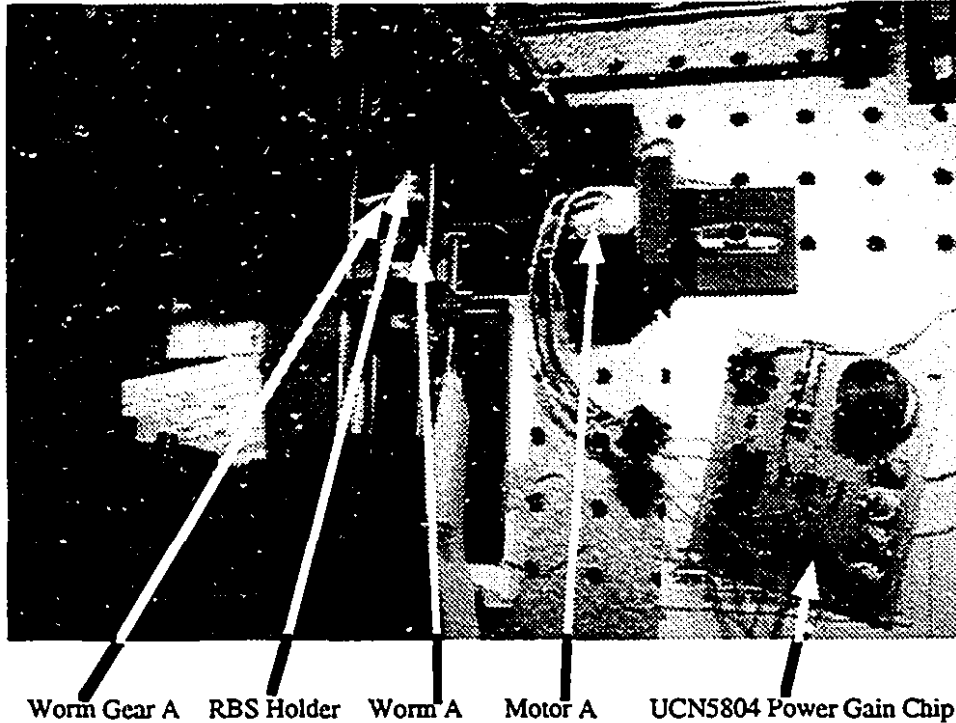


Fig 5.14: Jig used to assemble RBS holder—worm-gear assembly a) before curing, when position of RBS holder is moved and monitored on CCD until components are concentric b) during curing.



Worm Gear A RBS Holder Worm A Motor A UCN5804 Power Gain Chip
Figure 5.15: Photo of complete actuator setup indicating motors, worm, worm gear and RBS holder assembly. 25.4 mm pitch of holes on table gives scale of setup.

Determining the magnitude of backlash required knowledge of various gear parameters which are specified in data sheets or which must be measured ⁽⁶⁾. Given a pressure angle of 14.5° ⁽⁷⁾, and a conservatively estimated difference of about 0.5 mm (0.02") between the true standard centre distance and the measured centre distance, the backlash was determined to be ⁽⁸⁾:

$$B = 2 \tan(14.5) \times 0.50 = 0.26 \text{ mm} \quad (5.5)$$

which yielded an angular uncertainty of $\arcsin(0.26 / 15.875) = 0.93^\circ$.

5.5 Design, fabrication, and analysis of the optomechanical support structure for the Quadrant Detector package

This subsection describes how the QD was packaged and mounted onto the support plate with a minimum of rotation about the z-axis.

It was desired to kinematically mount the QD package on an x-y-z positioner in order to facilitate manual alignment of the QD as well as to simplify certain system and device

characterizations such as the optoelectronic sensitivity measurements described in this chapter. Since the x-y-z positioner, by definition, could move the QD package in any lateral direction, the challenge was to kinematically mount the QD on an x-y-z positioner with a minimum of rotation about the z-axis (A small tilt about the x- and y-axes is not as critical since the direction of the beams reflected from the QD is important only for the imaging system, which has its own independent positioning).

The QD package, a standard TO-5 package, is shown in Figures 5.16 a) and b). The leads coming out the back carry the 4 photocurrents as well as the common reverse bias voltage and considerably complicate the mounting operation. The undesirable rotation of θ_z about the z axis is shown in Figure 5.16c)

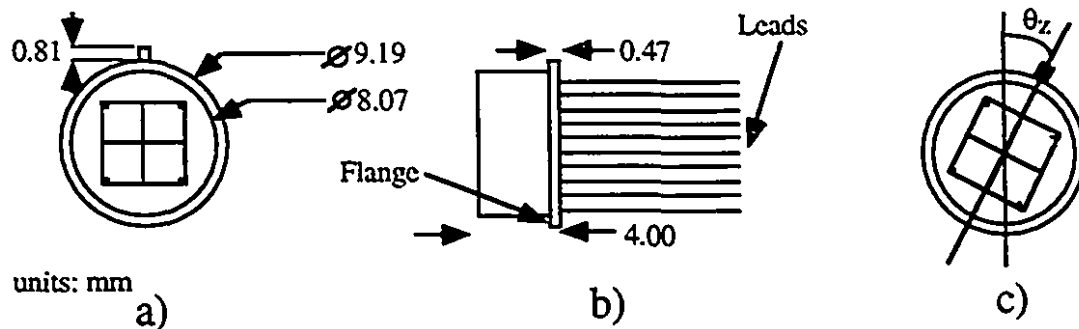


Figure 5.16. a) ,b) Front and side drawing of the TO-5 package c) undesirable rotation θ_z .

The procedure for mounting the QD was as follows. First, wires for the photocurrents and the reverse bias voltage were soldered onto the appropriate leads of the TO-5 package and labeled. Secondly, a support plate was machined which bolted onto a Newport x-y-z 461 positioner. A simplified drawing of this plate is shown in Figure 5.17a). Thirdly, RTV 732 elastomer was placed onto the seat and along the clearance hole in the plate and the TO-5 flange was glued onto the seat, as shown in Figure 5.17b).

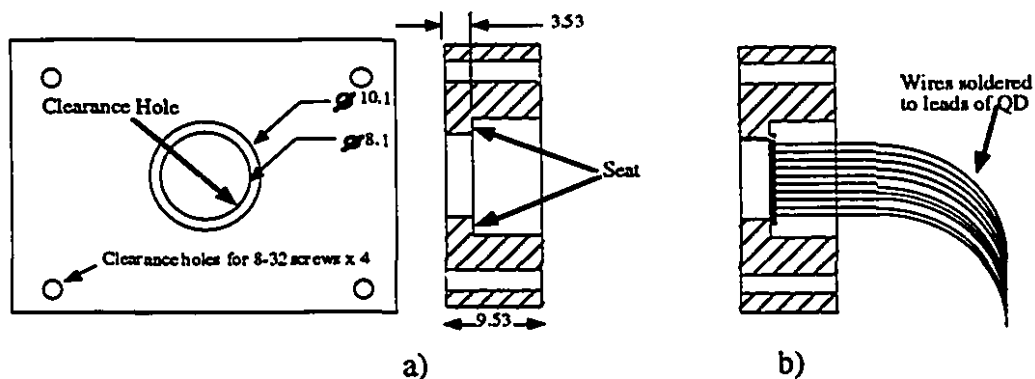


Figure 5.17: a) Support plate for the TO-5 b) Mounted TO-5.

The third step was very problematic. It was difficult to properly position the TO-5 with no rotation. Even when the TO-5 was properly positioned, the surprisingly great torsional force of the wires very rapidly (<10 seconds) tended to rotate the QD package about the z-axis toward an arbitrary 'rest position' when the glue was curing. To properly position the TO-5 with no rotation, an imaging system was built to image the QD onto a CCD camera. The CCD image was digitized and magnified, which allowed for calculation of the rotation angle θ_z . The TO-5 was then manually rotated about the z-axis until it was aligned in the seat. A magnet then clamped the steel-cased TO-5 in place until the glue finished curing.

The final result is shown in Figure 5.18. θ_z was calculated to be 2.3° . The impact of $\theta_z = 2.3^\circ$ is as follows.

For a spot theoretically centered at $P_i(x_i, y_i)$ in the first quadrant, the center $P_i(x_i, y_i)$ which is incorrectly determined by the QD due to the TO-5's rotation about the z-axis is:

$$(x_i, y_i) = (x_i \cos(\Delta\theta_z) - y_i \sin(\Delta\theta_z), y_i \cos(\Delta\theta_z) + x_i \sin(\Delta\theta_z)) \quad (5.6)$$

which for $\theta_z = 2.3^\circ$ and $x_i = y_i$ yields $(x_i, y_i) = (0.96x_i, 1.04y_i)$. The analysis is similar for all quadrants and is based on the z-axis rotational misalignment derived in Chapter 2.

This error depends also on the horizontality of the viewing CCD camera which was clamped as rigidly as possible to its x-y-z positioner. This error, while potentially problematic for other systems, did not affect the demonstrator's performance since the hunting algorithm determined the initial angular position of the RBSs relative to the QD itself, regardless of its rotation. In other words, the detected $(\Delta x_e, \Delta y_e)$ misalignment error was rotated by θ_z , but the calculated (θ_A, θ_B) are also rotated by the same amount. As a result, the spot was still properly centered. Nonetheless, this exercise indicated that mounting a device with a minimum of θ_z rotation can be complex.

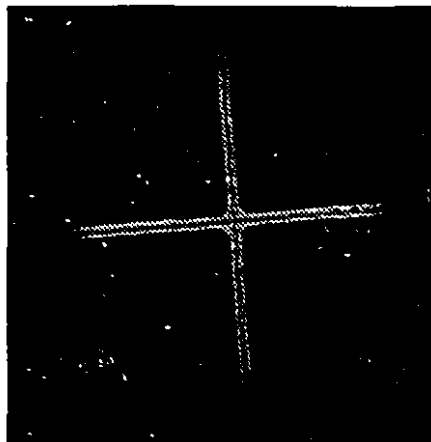


Figure 5.18: Actual mounted QD.

5.6 Computer hardware and software setup

The complete algorithm was encoded on LabView™ software running on a Macintosh Centris 650. The four voltages V_1 , V_2 , V_3 , and V_4 sampled by the LAB-NB™ board were accessed via LabView™. Since showing the entire program would require two dozen pages, only the user interface and the highest block level diagram are shown in Figures 5.19 a) and b) respectively. In the highest level block diagram, of Figure 5.19b), the 5 main steps through which the program sequences are indicated by the arrows: 1) get analog inputs 2) calculate misalignment error 3) calculate θ_A and θ_B 4) calculate the number of pulses to send to the motors 5) send the pulses to the motors.

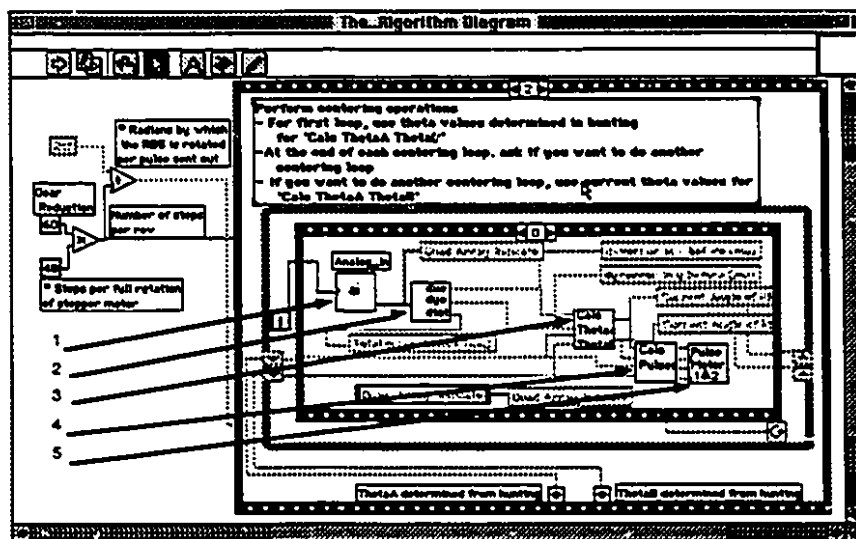
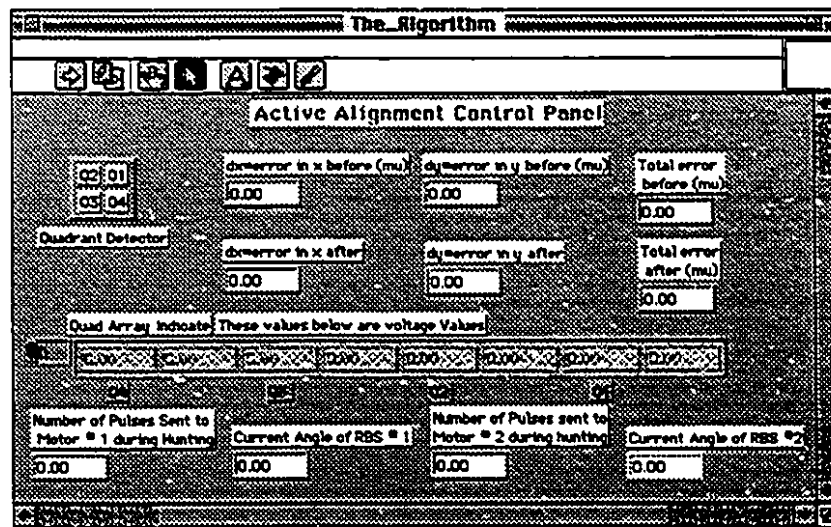


Figure 5.19): Active alignment program: a) Control panel b) highest level of program.

5.7 Effect of packaging and optomechanics on spot profile

The spot impinging on the QD did not have an ideal Gaussian irradiance distribution for many reasons. The main reason for this non-Gaussian profile was the presence of interference fringes. The TO-5 package in which the QD is mounted had a glass cover plate covering the QD and the light impinging on the QD first had to go through a quartz cover plate on the TO-5. Since the plate was not AR coated, multiple reflections created interference fringes. These fringes are clearly visible in Figure 5.20a). However, these fringes did not seem to bring about major inaccuracies in the measured data since the spot in Figure 5.20a) was the actual spot used to obtain the data plotted in Figure 5.2. The likely explanation for the accurate results despite the interference fringes is: the spot was so large that the effect of the fringes was averaged out over the large area of the spot.

Another reason for the non-Gaussian profile was the clipping that took place as the beam went through the bore of the G1024 worm gear. Optical power measurements indicated that 16.5% of the beam power was clipped as the beam went through both RBS holder assemblies. Of this 16.5%, 7.7% can be attributed to reflection losses due to two RBSs (each RBS has 2 optical surfaces, with a 2% loss at each optical surface) and the remaining 9.5% loss was due to the beam being clipped by the 4.763 mm bore diameter. A 9.5% loss in power due to clipping indicates that the bore diameter was only $2.17w$, where $2w$ is the beam diameter (e^{-2} points). As a result of this clipping, the actual spot profile was closer to that of an Airy function than to that of a Gaussian, as Figure 5.20b) shows.

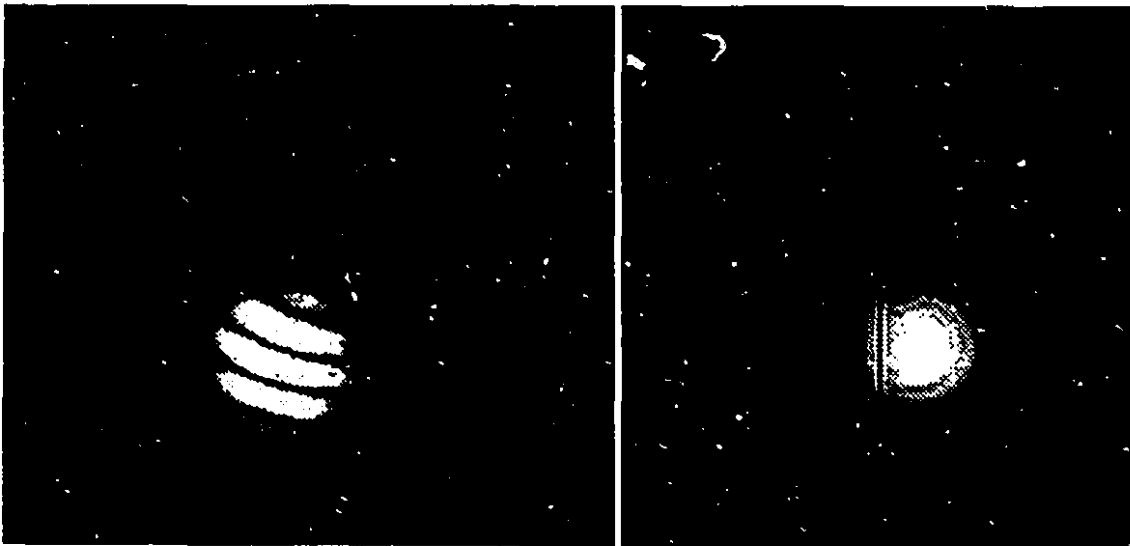


Figure 5.20: a) Interference fringes on spot brought about by quartz cover plate on TO-5 package holding the QD. b) spot on QD with TO-5 cover plate removed.

5.8 Conclusion

The work presented in this chapter indicates that substantial optical, electrical, computer and mechanical engineering was required to bring the active alignment optical design from theory to reality. It was determined that many engineering solutions are not unique and are dictated as much by theoretical considerations as by practical conditions such as the layout of the working environment or the availability of parts and equipment. Furthermore, engineering solutions to physical problems often brought about deviations from ideal models: the aperturing of the beam due to the small bore of the (easily available) worm gear was one such example.

Nonetheless, the system was built and it successfully implemented the algorithm for centering a spot on a QD using Risley Beam Steerers. The experimental results are discussed in the next chapter.

5.9 References

- [1] Hamamatsu technical specifications, Quadrant Detector # S4349 (1991).
- [2] Uniphase Inc. Model 1508 HeNe laser specifications.
- [3] Don Pavlasek, personal communication.
- [4] ACV 135 Camera specifications, Newport Inc.
- [5] A. Ahmad, "The adjustment mechanisms: types and their applications in optical systems", in *Optomechanical Design*, P. Yoder ed., **CR43**, 254 (1992).
- [6] McGill University, Course notes for course 305-260, Machine Tool Lab, given by Professor Cherna (1994).
- [7] Boston Gear Catalog, p. 74.
- [8] Berg Gear Catalog B8, p. 552.

Chapter 6

Experimental results

6.1 Introduction

This chapter gives experimental results of the fully operational demonstrator system whose theoretical underpinnings and actual construction were described in the previous chapters and in the appendix. Section 6.2 presents data produced from centerings performed by the demonstrator. Section 6.3 outlines the main limitations of the system.

6.2 Centering the spot

The objective of the demonstrator is to centre a spot on a QD: the misalignment error of the spot after being centered is ideally $(\Delta x_e, \Delta y_e) = (0, 0) \mu\text{m}$ (all displacement dimensions in this chapter are in μm).

In chapter 4, an algorithm for centering a spot using two RBSs was derived. This algorithm was encoded into LabView™. The RBSs, which nominally had identical wedge angles, actually had measured wedge angles of $\beta_A = 0.208^\circ \pm 2\%$ and $\beta_B = 0.278^\circ \pm 2\%$. Consequently, the radii of the two circles described in section 4.3.3 along which the spot moved were not identical but were in fact different. The two actual radii were: $r_A = 181 \mu\text{m}$ and $r_B = 242 \mu\text{m}$.

6.2.1 Implementation of algorithm

Before presenting the raw data, an example is given which explains how to interpret the data. An explanation of figure 6.1, which shows a complete centering operation, is as follows.

The spot initially started at position 1 on the QD surface with a misalignment error of $(\Delta x_e, \Delta y_e) = (-127, 92)$ microns. For the spot at position 1, the algorithm calculated the angular displacement (θ_A, θ_B) required for RBS A and RBS B to centre the spot, as was described in chapter 4. Once the two angles were calculated, the RBSs were rotated to their respective newly calculated angular positions. (The solid curved lines indicate the actual spot displacement on the QD). However, the laser fluctuations and other sources of error described in chapter 4 contributed to a slight inaccuracy in the detected error. This

inaccuracy caused the algorithm to calculate the new RBS angles (θ_A , θ_B) based on slightly inaccurate data. As a result, the spot was moved to position 2, which was $\sim 20 \mu\text{m}$ away from the centre of the QD. A second iteration was thus required.

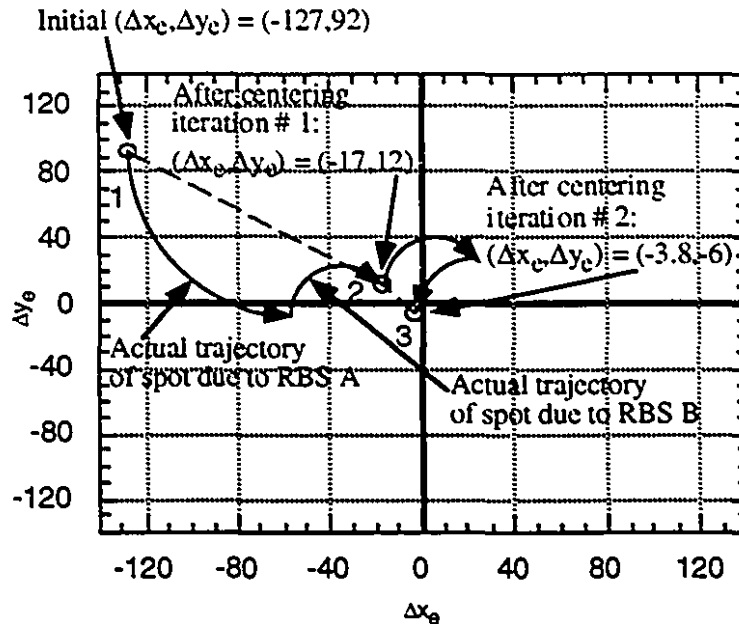


Figure 6.1 Centering operation requiring two iterations.

At position 2, the algorithm once again calculated the (θ_A , θ_B) required for RBS A and RBS B to centre the spot, and once again the RBSs were rotated to their respective newly calculated angular positions. This time, the spot was effectively centered to within the detection accuracy of the system, which was $\pm 5 \mu\text{m}$ for each coordinate (x,y).

The spot was thus centered from $(127^2+92^2)^{1/2} = 157 \mu\text{m}$ away from the centre to $(3.8^2+6^2)^{1/2} = 7.1 \mu\text{m}$ away from the centre in two iterations.

All other runs also managed to come to within $20 \mu\text{m}$ in just one iteration, regardless of the magnitude or direction of the misalignment error. Furthermore, on nearly half the occasions the spot was centered to within $10 \mu\text{m}$ in just one iteration. The results are displayed in graphical form in Figures 6.2 a)-h) and in tabular form in Table 6.1. The results in table 6.1 corresponding to Figures 6.2a)-h) were obtained in 8 consecutive runs after an initial hunting in which the initial angles (θ_A , θ_B) were determined.

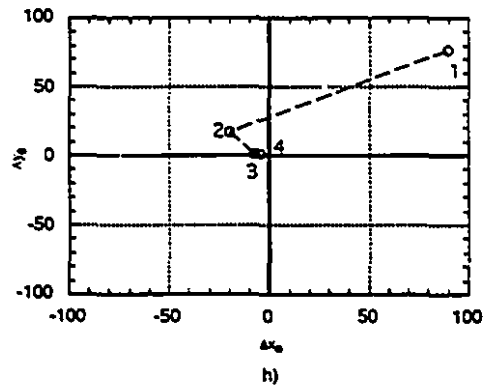
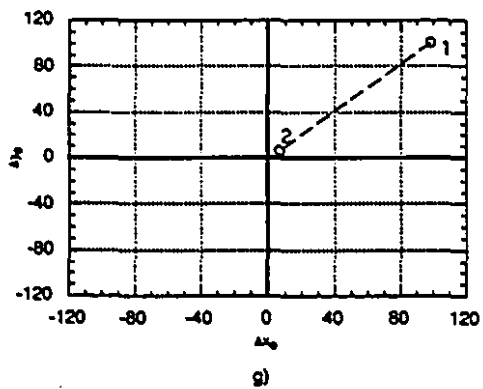
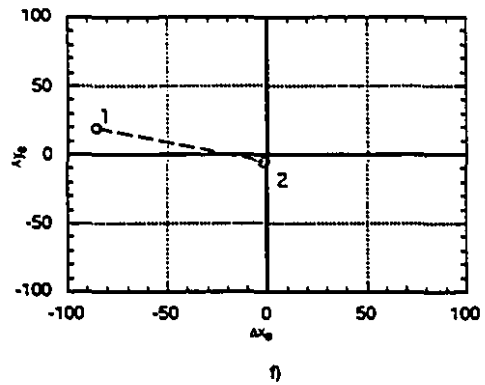
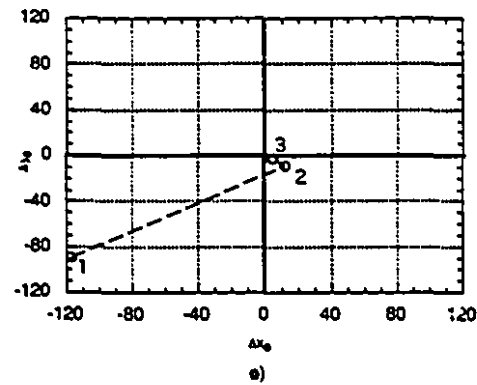
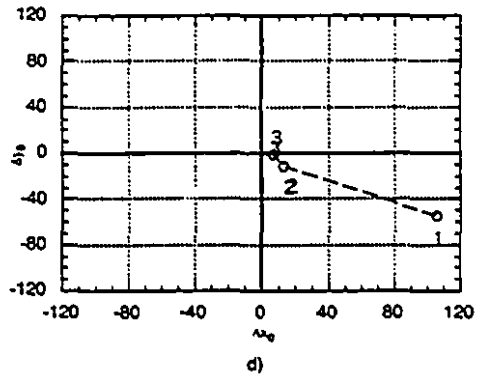
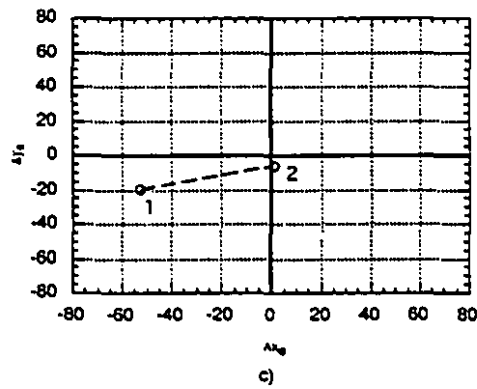
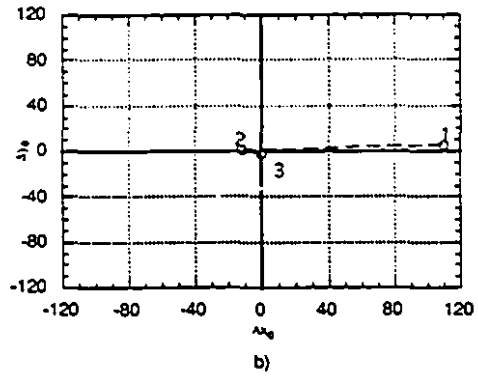
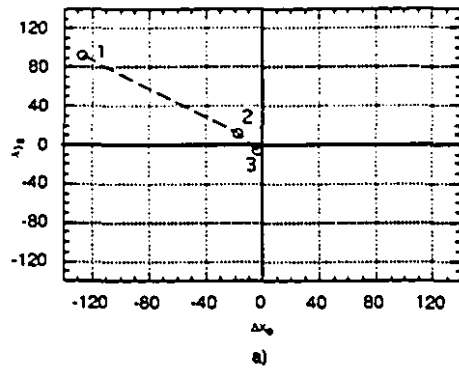


Figure 6.2 a)-h) centering of the spot for various misalignment errors.

Initial $(\Delta x_e, \Delta y_e)$ (μm)	Initial distance from centre (μm)	Final $(\Delta x_e, \Delta y_e)$ (μm)	Final distance from centre (μm)	# iterations
(-127,92)	157	(-3.8,-6)	7.1	2
(109,5)	109.1	(-0.8,-2)	2.15	2
(-53,20)	56.64	(1.1,-6.1)	6.2	1
(106,-55)	119.4	(7.2,-1.4)	7.3	2
(-117,-89)	147	(5,-2.9)	5.8	2
(-85,19)	87.1	(-2,-5)	5.4	1
(90,103)	136	(7.1,6.8)	9.8	1
(89,76)	117	(-1.3,3.9)	4.1	3

Table 6.1: Result of centerings of spots.

The experimental process which yielded the results in Table 6.1 was as follows: the hunting determined the initial angular position (θ_A, θ_B) of the RBSs; at that point, the error was determined to be $(\Delta x_e, \Delta y_e) = (-127, 92) \mu\text{m}$. The spot was then automatically centered to $(\Delta x_e, \Delta y_e) = (-3.8, -6) \mu\text{m}$ in 2 iterations by the system. A 'perturbation' was then simulated: the support plate which was bolted onto the x-y-z Newport stage and which held the QD in the TO-5 was manually moved by $\sim 110 \mu\text{m}$ to position $(\Delta x_e, \Delta y_e) = (109, 5) \mu\text{m}$ according to the QD. Once again the spot was automatically centered by the system. This maneuver was repeated 8 times for various perturbations in different directions.

The algorithm accepted RBSs with two different wedge angles and as such it 'recognized' the blind area brought about by the wedge mismatch; the algorithm thus did not attempt to centre the spot if such a task was theoretically impossible. As a result, the operator first checked every manual $(\Delta x_e, \Delta y_e)$ 'perturbation' with the algorithm running under Matlab™ on another computer to ensure that the perturbation did not require the spot to be centered to a position within the blind area: such a centering would have been impossible.

Figure 6.3 shows the initial and final position of a spot which was centered from $(\Delta x_e, \Delta y_e) = (-160, 25) \mu\text{m}$ to $(\Delta x_e, \Delta y_e) = (4, -3) \mu\text{m}$.

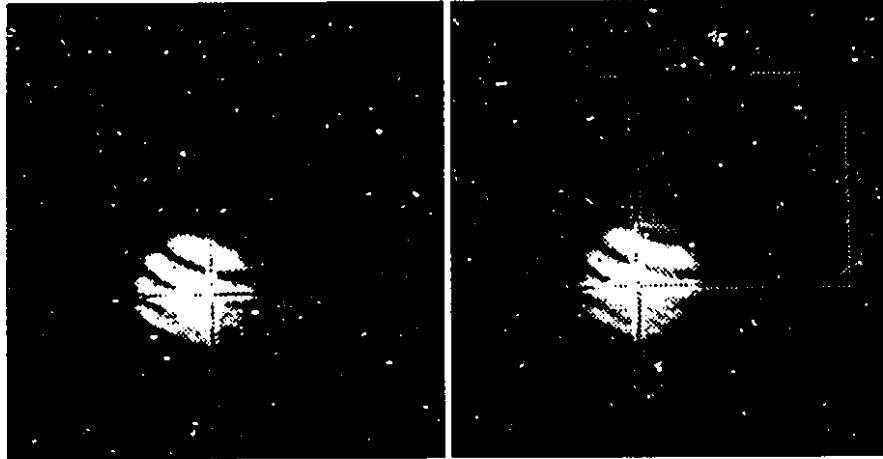


Figure 6.3: spot centering example. a) Before $(\Delta x_e, \Delta y_e) = (-160, 25)$ b) After $(\Delta x_e, \Delta y_e) = (4, -3)$ μm .

6.3 Limitations of demonstrator

6.3.1 Wedge mismatch

An experiment was performed to measure the wedge mismatch within the complete system. It was based on the fact that for the ideal case ($r_A = r_B$), the two RBSs impart no net displacement on the spot either when $\theta_A = 0$ and $\theta_B = \pi$ or when $\theta_A = \pi$ and $\theta_B = 0$. The steps were as follows. 1) The RBSs were rotated such that $\theta_A = 0$ and $\theta_B = \pi$, and the spot's x-coordinate, Δx_{e1} , was measured. 2) The RBSs were then rotated such that $\theta_A = \pi$ and $\theta_B = 0$, and the spot's x-coordinate, Δx_{e2} , was measured. Simple geometry yielded the following relation:

$$\Delta x_{e1} - \Delta x_{e2} = 2(r_A - r_B) \quad (6.3)$$

According to this calculation the difference in radii was $r_A - r_B = 60 \mu\text{m}$, which corresponds to a wedge mismatch of $\sim 0.067^\circ$. This result is consistent with the measurements performed on the RBSs before insertion into the demonstrator system. Furthermore, if the algorithm assumed the wedges were matched and equal to their nominal $15'$, the maximum error due to the wedges would be equal to $2 \times 60 \mu\text{m} = 120 \mu\text{m}$.

In order to bypass the effect of the wedge mismatch, the incoming beam was slightly misaligned during initial system alignment before the optics were inserted into the system. This ensured that the blind area was not at the centre of the QD. Such slight misalignments are often used to correct for misalignments or range limitations of RBSs⁽¹⁾. Since the total

radius of action of the two RBS is of the order of $\sim 425 \mu\text{m}$ and since the blind area has a radius of $60 \mu\text{m}$, an initial (before RBS insertion into the system) misalignment of the spot to a distance of $212 \mu\text{m}$ from the QD centre will ensure that any error $< 152 \mu\text{m}$ will be inevitably centered. Depending on initial conditions, greater errors can also be centered.

6.3.2 Limitations on initial conditions for the hunting algorithm

Besides the mismatched wedges, the other main limitation of the system could be seen during the hunting sequence, which was used to determine the initial angular displacement of the RBSs upon system startup. As was described in chapter 4, during the hunting sequence each RBS was individually rotated; in theory, the rightmost displacement of the spot (i.e. the Δx_e value of the spot $= \Delta x_{emaxA}$) when only RBS A was rotated corresponded to $\theta_A=0$ and the rightmost displacement of the spot, Δx_{emaxB} , when only RBS B was rotated corresponded to $\theta_B=0$. Thus, as far as the hunting sequence was concerned, only Δx_{emaxA} and Δx_{emaxB} were important since these determined $\theta_A=0$ and $\theta_B=0$. Once the computer knew where $\theta_A=0$ and $\theta_B=0$, the computer could then deterministically move the RBSs to any other angular position.

A full rotation of either RBS caused the spot on the QD to move along the circumference of a circle $362 \mu\text{m}$ or $484 \mu\text{m}$ in diameter for RBS A and B respectively. However, as was indicated in Figure 5.2, the differential voltages ΔV_x and ΔV_y generated by the QD photocurrents were not linearly related to the distance from the centre beyond approximately $200 \mu\text{m}$. Furthermore, beyond $300 \mu\text{m}$, the voltages did not significantly change for further displacements of any magnitude away from the centre. Consequently, the computer did not accurately detect the rightmost spot displacement, or maximum Δx_e , if $\Delta x_e > 300 \mu\text{m}$. (If $200 < \text{Maximum } \Delta x_e < 300$, the computer could still determine maximum Δx_e , since ΔV_x would still have been monotonically, although not linearly, increasing with increasing Δx_e . Only for $\Delta x_e > 300$ could ΔV_x not significantly increase for any additional Δx_e). If the computer could not accurately determine Δx_{emaxA} when RBS A was rotating, it could not accurately determine when $\theta_A=0$. Similarly, if the computer could not accurately determine Δx_{emaxB} when RBS B was rotating, it could not accurately determine when $\theta_B=0$. Figure 6.5 illustrates the problem. Depending on initial conditions, the Δx_e value of the spot might or might not go beyond $\Delta x_e > 300 \mu\text{m}$.

This uncertainty was problematic. One way to solve it was to increase the size of the spot: Figure 5.2 indicates that increasing spot size increases the linear range, but decreases the measurement sensitivity. This solution was undesirable since it permanently decreased the measurement sensitivity of the system just for the benefit of an initial startup routine.

Another solution was to initially ensure that the spot be sufficiently to the left in quadrants 2 and 3 (i.e. a large negative x-coordinate) before the hunting begins; this solution was chosen.

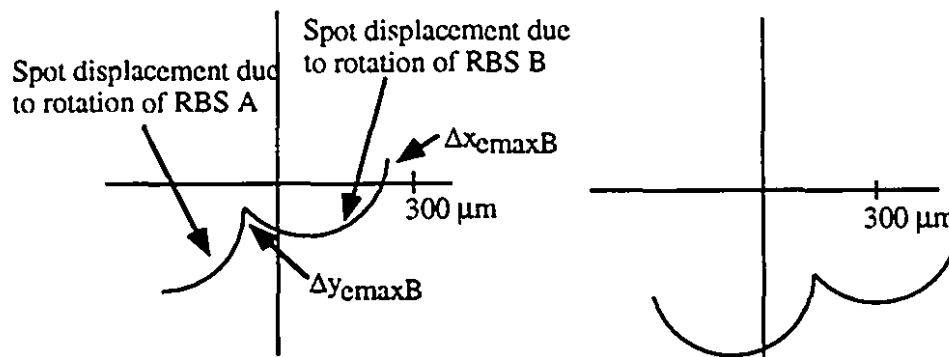


Figure 6.5: Real implementation of hunting: a) $\Delta x_c < 300 \mu\text{m}$: reliable result generated by hunting b) $\Delta x_c > 300 \mu\text{m}$: unreliable result generated by hunting.

6.4 Conclusion

The active alignment demonstrator was successfully demonstrated: spots were consistently centered for arbitrary displacements within the range of the system.

Limitations for the system were identified and characterized. These included mismatch of the wedges: the incoming beam had to be slightly misaligned during system construction in order to ensure reliable operation over a fixed range of operation. Certain misalignment errors beyond this fixed range of operation could also work provided they did not require movement into the blind area of the mismatched wedges. As well, it was shown that non-linearities in the detection of large misalignment errors could lead to serious errors during the hunting sequence which determines the initial angular displacement (θ_A, θ_B) of the RBSs. In order to minimize the impact of these limitations, restrictions were imposed on the initial position of the spot on the QD.

6.5 Reference

- [1] F. B McCormick, F. A. P. Tooley, J. L. Brubaker, J. M. Sasian, T. J. Cloonan, A. L. Lentine, R. L. Morrison, R. J. Crisci, S. L. Walker, S. J. Hinterlong, M. J. Herron, "Optomechanics of a free-space photonic switching fabric: the system", *SPIE Vol. 1533* 97 (1991).

Chapter 7

Future directions and conclusion

7.1 Future Directions

The RBS-based system described in this thesis is just a simple proof-of-concept demonstrator. In the future, if active alignment is to be implemented for practical free-space optical interconnects, then scalability, integration of alignment algorithms, and other issues will have to be explored. This section outlines some basic concepts worthy of further study.

7.1.1 Scalability

While the RBS active alignment demonstrator successfully aligned one spot onto a Quadrant Detector (QD), it is important to study how this or other active alignment systems can be scaled to systems having hundreds or even thousands of receiver windows. A typical system having an array of receiver windows on a grid of pitch D is shown in Figure 7.1.

One simple solution to the above-mentioned problem of scalability is to place QDs on a continuation of the grid at a distance D from the receiver windows, as shown in Figure 7.1. If the spots impinging on the receiver windows are produced by a grating, then higher order spots will impinge on the QD; for a misalignment just in the Δx_e or Δy_e direction, aligning a spot on a QD will necessarily align all the spots on the receiver array. Further flexibility is achievable if the imaging system is lenslet array based rather than bulk optic based. For example, the lenslets imaging onto the QDs could be of different focal lengths in order to create larger spots (which were shown in chapter 3 to give a linear relationship between photocurrents and misalignment error over a greater range of misalignment errors). Furthermore, other lenslets could be made astigmatic and thus create spots on the QD which would yield information about the Δz_e misalignment error of the array. If many QDs were present, information about all six misalignment errors could be obtained. An interesting calculation to be performed in the future will be the determination of the minimum number of QDs required to yield information about all six misalignment errors. Finally, depending on its type, the grating could be optimized to produce full intensity spots rather than higher order spots on the QD.

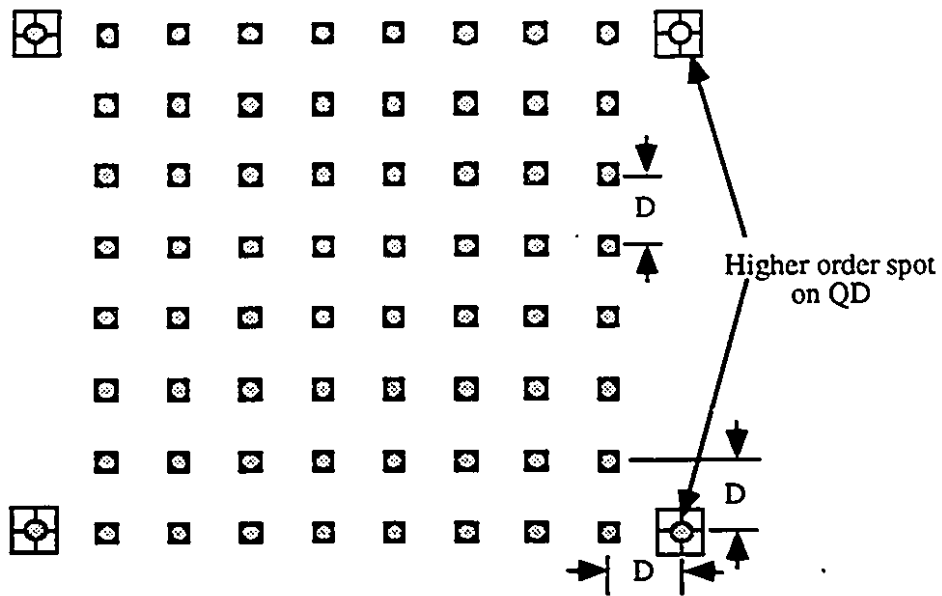


Figure 7.1: Use of higher order spots to illuminate properly positioned QDs.

However, using such a system with SEEDs and other devices requiring dual-rail logic will be difficult since only one alignment spot must be present in the QD vicinity if the solution proposed above is to yield accurate alignment information. For example, if two adjacent spots are present, as shown in Figure 7.2, then the calculations in this thesis which determined the relation between the misalignment of one spot and its associated photocurrents will be incorrect. For example if spot A is the alignment spot and spot B is the adjacent spot produced by the grating due to its optimization for dual-rail logic, spot B could contribute significant additional light power to the QD, resulting in an inaccurate calculation of the misalignment error. The inaccuracy of the misalignment error calculation will be a function of the QD size, the centre-to-centre separation of the adjacent spots, and the spot size, as well as the magnitude and direction of Δx_e and Δy_e . If the inaccuracy is unacceptable, other solutions will have to be considered, such as calculating the relation between the misalignment of two spots on a QD and their associated photocurrents (as opposed to the relation between the misalignment of one spot and its associated photocurrents which was done in this thesis), varying the location or geometry of the alignment detectors, or optimizing the grating to produce just one spot on the QD. The proper detection and calculation of misalignment errors is an issue which must be further researched.

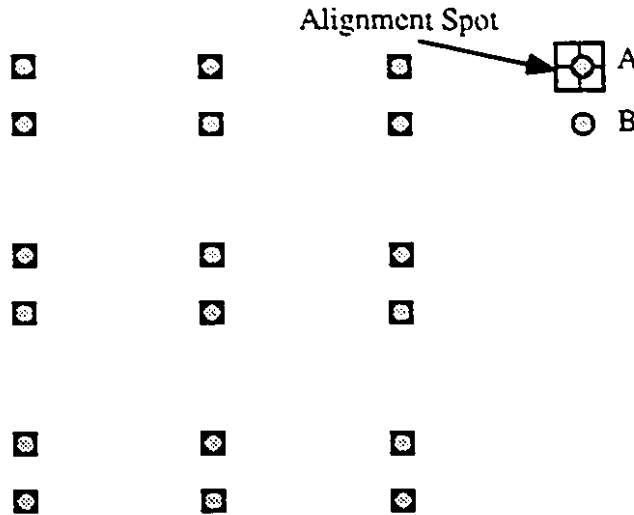


Figure 7.2: Effect on QD of spots for dual rail logic. Depending on system parameters, spot B might cause inaccuracy in calculation of misalignment error.

7.1.2 Integration of alignment intelligence

Regardless of the geometry and position of the detectors, the photocurrents produced by them will have to be processed and sent to controllers which will move actuators and optics in order to realign the spot array after a misalignment. In the demonstrator described in this thesis, all this was done on the computer. However, it would be awkward for future backplanes to have external computers perform all the alignment calculations. This added processing could be added to the smart pixel in the form of additional circuitry which has nothing to do with architectural implementations or on-chip BIST (built-in-self-test). For example, all the calculations of the misalignment errors such as $\Delta x_e = k(V_1 + V_4 - (V_2 + V_3))$ and $\Delta y_e = k(V_1 + V_2 - (V_3 + V_4))$ could be done right on chip, as shown in Figure 7.3a) (where V_1 , V_2 , V_3 and V_4 correspond to the voltages produced by a QD's four photocurrents across loads). The alignment algorithms themselves could be programmed into a Field Programmable Gate Array (FPGA) residing on the PCB. The 'calculated' misalignment error signals such as Δx_e and Δy_e would then have to be sent off the smart pixel chip to the FPGA. In order to save on pinouts, the error signals could be multiplexed into just one line. A complete system is shown in Fig 7.3b). This 'alignment intelligence' (and eventually other such diagnostics intelligence like thermal measurements) will add a new degree of functionality to the smart pixel. Eventually, as integration densities increase, complete alignment diagnostics and correction algorithms could be integrated right on the smart pixel chip itself.

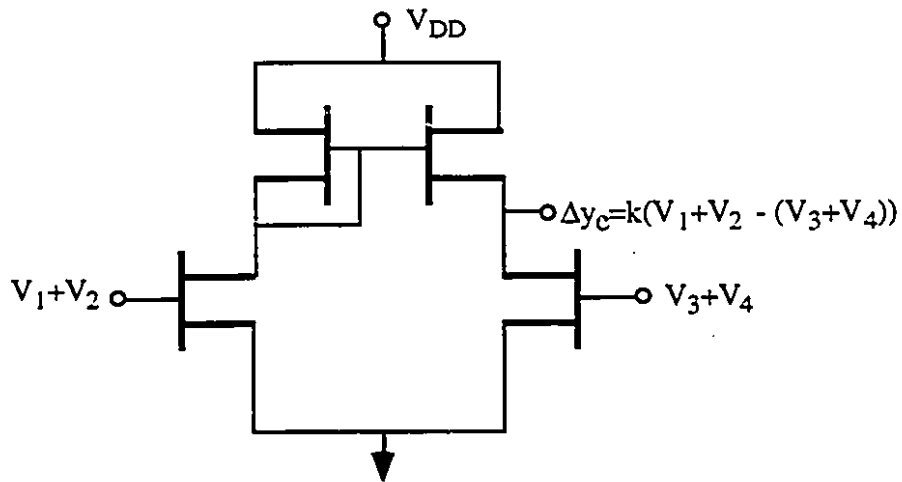


Figure 7.3a): Circuitry for calculating misalignment error Δy_e on smart pixel .

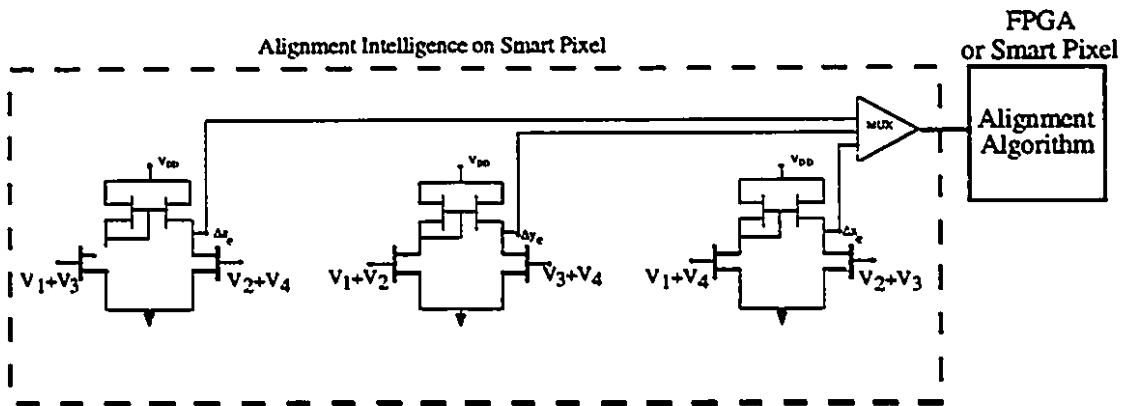


Figure 7.3b): Concept of alignment intelligence in which extensive processing of misalignment error is performed on smart pixel.

7.1.3 Further issues

Piczo- and ferro-electric actuators will have to be further studied in the future. Many of the sophisticated active alignment systems described in chapter 3 featured piezo-electric or other solid-state actuators since these are more mechanically reliable. However, since these actuators are often non-linear over their lifetime, control issues associated with these actuators will be more challenging. For example, adaptive algorithms controlling piezo-electric actuators could be a promising combination warranting further study.

7.2 Conclusion

This thesis demonstrated that traditional electronic backplanes are rapidly approaching cost/performance limits beyond which any further improvements will likely yield diminishing returns on the cost of the improvements. Free-space optical backplanes were shown not to suffer from these limits. However, maintaining the alignment of free-space optical interconnects was shown to be one of the key problems which had to be solved in order to implement practical free-space optical backplanes. Active alignment was shown to be a possible solution to this problem.

This thesis surveyed different active alignment systems and described the successful design, simulation, fabrication and testing of an active alignment demonstrator system which could correct for x-y misalignment errors in an existing free-space optical backplane demonstrator. The active alignment demonstrator used two RBSs to move a spot in the focal plane of a lens and featured an algorithm which calculated the angular position of RBSs required to centre the spot, as well as associated optics and mechanics needed to rotate the RBSs in a controlled manner to the angular positions calculated by the algorithm.

It was shown that contributions from optical, mechanical, electrical and computer engineering are all required in order to build an active alignment system. Furthermore, it was shown that some misalignment mechanisms such as rotational misalignment error about the z-axis, θ_z , are particularly difficult to correct for. Finally, this thesis demonstrated that active alignment in systems featuring free-space optical interconnects is an exciting new field with many promising avenues for further research.

Appendix A

Exact calculation of effect on beam of RBSs in series

In this appendix is derived the exact maximum angular deviation imparted on a normally incident beam by a pair of RBSs (Risley Beam Steerers) in series, as shown in Figure A1. The solution, the main steps of which are shown below, is essentially the result of repeated applications of Snell's Law, along with basic geometry.

A1 Calculation of exact expression

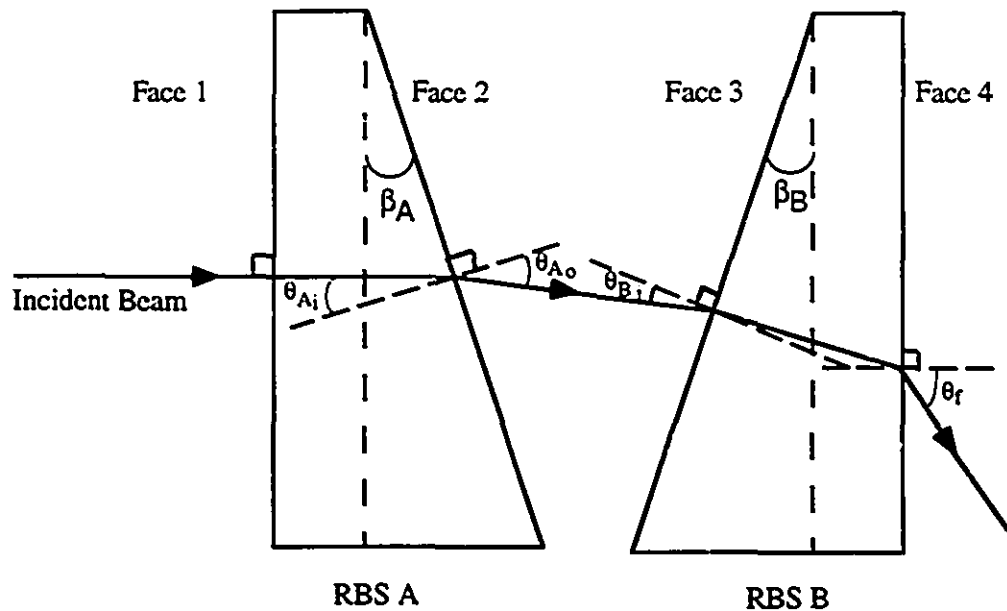


Figure A1: Geometry used in calculation of beam deviation imparted by RBSs in series.

All angles in this figure are greatly exaggerated for clarity.

The incident angle arrives normal to Face 1 and as such is not deviated. At Face 2, basic geometry indicates that

$$\theta_{A_i} = \beta_A \quad (A1)$$

and the refracted angle is:

$$\theta_{A_o} = \arcsin \left[\frac{n_r}{n_a} \sin(\beta_A) \right] \quad (A2)$$

Further geometry indicates that for face 3:

$$\theta_{B_1} = \beta_A + \beta_B - \theta_{A_1} \quad (\text{A3})$$

Further applications of Snell's law and basic geometry yield the final result, which is the exact solution for the maximum deviation imparted on a beam by two RBSs in series:

$$\theta_f = \arcsin \left\{ \frac{n_g}{n_a} \sin \left\{ \beta_B - \arcsin \left[\frac{n_a}{n_g} \sin \left[\beta_A + \beta_B - \arcsin \left(\frac{n_g}{n_a} \sin(\beta_A) \right) \right] \right] \right\} \right\} \quad (\text{A4})$$

A2 Comparison of exact expression with first order approximation

From Equation (4.18), the first order approximation for the maximum deviation imparted on a beam by two RBSs in series is:

$$\delta_{tot} = (n_g - 1)(\beta_A + \beta_B) \quad (\text{A5})$$

The actual physical values assumed in the demonstrator are:

n_a = refractive index of air = 1.

n_g = refractive of index of BK7 of RBS = 1.515.

$\beta_A = 0.208^\circ = 0.00363$ rad.

$\beta_B = 0.278^\circ = 0.00485$ rad.

$f=100$ mm.

The final angular deviation calculated by the exact expression is $\theta_f = 0.00430903$ rad.

The final angular deviation calculated by the approximation is $\delta_{tot} = 0.00430901$ rad.

Neglecting lens aberrations for these small values, the spot displacement at the focal plane, r , imparted by a lens of focal length f is:

$r_{\text{exact}} = 430.906$ μm

$r_{\text{approx}} = 430.904$ μm

The small difference between the first order approximation and the exact answer indicates that the use of first order approximations for the demonstrator was justified.